SURFACE ENGINEERED BIOSENSORS FOR THE EARLY DETECTION OF CANCER

by

MUHYMIN ISLAM

Presented to the Faculty of the Graduate School of
The University of Texas at Arlington in Partial Fulfillment
of the Requirements
for the Degree of

DOCTOR OF PHILOSOPHY

THE UNIVERSITY OF TEXAS AT ARLINGTON
December 2015

Acknowledgements

I am grateful to my parents for their continuous support, patience and understanding. I will be forever indebted to my advisor Dr. Samir M. Iqbal for the opportunity to work with him, for his guidance, support and expertise. I believe I am not an easy person to deal with and I am thankful for bearing with me for all these years. My heartiest gratitude goes to Dr. Young-tae Kim, without whose support and advice I could never complete my research work. I also thank Dr. Santaneel Ghosh, Dr. Donald Butler and Dr. Robert Magnusson for their kind consent to review my dissertation and for being in my PhD committee. I will take this opportunity to also extend my thankfulness to my co-workers Yuan Wan, Waseem Asghar, Mohammad Arif Iftakher Mahmood, Azhar Ilyas, Motasim Bellah, Waqas Ali, Raziul Hasan, Nuzhat Mansoor, Usman Raza, Madiha Hanif, Wenny, Adeel Sajid, Raheel Raja, Loan Bui, Samik Bhattari, Sandeep Shah and many others for their advice, stimulating discussion and hands on help during my research. A special thank goes to the staff of the Department of Electrical Engineering and Nanotechnology Research Center for extending their helping hands throughout my way.

October 20, 2015

Abstract

SURFACE ENGINEERED BIOSENSORS FOR THE EARLY DETECTION OF CANCER

Muhymin Islam, PhD

The University of Texas at Arlington, 2015

Supervising Professor: Samir M. Iqbal

Cancer commences in the building blocks of human body which are cells. In most of the cases, it remains silent in early stage. This is expressed at molecular and cellular levels at primary stages. Recognition of disease at these micro and nano levels might reduce the mortality rate of cancer significantly. This research aimed to introduce novel electronic biosensors for identification of cancer at cellular level. First of all, the dissertation focuses on label-free isolation of metastatic tumor cells using filter based microfluidic devices. Then, nanotextured polymer substrates were implemented for enhanced cancer cell isolation and cell growth. Next, nanotextured microfluidic channel was used for electrical profiling and detection of tumor cells from blood. Finally, a biochip was developed for the detection of tumor cells by electrical profile and surface immobilized aptamer. Standard silicon processing techniques were used to fabricate all of the biosensors. Nantoextruing and surface functionalizon were incorporated to elevate the efficiency of the devices.

The first approach aimed to detect cancer cells from blood based on their mechanophysical properties. Cancer cells are larger than blood cells but highly elastic in nature. These cells squeezed through microchannels much smaller than their sizes. The cross-sectional area of the microchannels was optimized to isolate tumor cells from blood. Nanotextured polymer substrates, a platform inspired from the natural basement membrane, were used to enhance the isolation and growth of tumor cells. Micro reactive ion etching was performed to have better control on features of nantoxtured surfaces. Next, electrical measurements of ionic current were performed across single microchannel to detect tumor cells from blood. Later, nanotexturing was shown to enhance the efficiency of the devices by selectively altering the translocation profile of cancer cells. Eventually, aptamer functionalized nanotextured polymer surfaces were integrated with ionic current measurements in a biochip to discriminate tumor cells from blood with higher efficiency and selectivity. These biochip concepts can be implemented in point-of-care devices for the early detection of cancer at cellular level.

Table of Contents

Acknowledgements iii

Abstract iv

List of Illustrations..........xiii

List of Tables..........xx

Chapter 1 INTRODUCTION 1

Research Overview 2

Label-Free Isolation of Metastatic Tumor Cells Using Filter Based Microfluidic device 3

Nanotextured Polymer Substrates for Enhanced Cancer Cell Isolation and Cell Growth..........3

Nanotextured Microfluidic Channel for Electrical Profiling and Detection of Tumor Cells from Blood 4

Single Biochip for the Detection of Tumor Cells by Electrical Profile and Surface Immobilized Aptamer 4

Chapter 2 BACKGROUND AND REVIEW..........6

Origin of Cancer 7

Cancer Metastasis..........9

Epidermal Growth Factor (EGF) and Epidermal Growth Factor Receptor (EGFR)..........11

Epidermal Growth Factor 11

Epidermal Growth Factor Receptor (EGFR)..........13

Circulating Tumor Cells (CTCs)..........14

Probe Molecules: DNA/RNA Aptamers and Antibodies................................ 15
Systematic Evolution of Ligands by Exponential Enrichment (SELEX) 17
Multiscale Structures in Nature 18
    Nanostructures in Plants and Insect... 18
    Nanostructures in Insects... 23
    Nanostructures in Human Body 23
Soft Lithoghraphy 27
PDMS.. 28
Microfluidic Systems 29
    Dielectrophoresis (DEP).. 30
    Cell-Affinity Micro-Chromatography 34
    Magnetophoresis 36
    Mechanophysical Properties 39
Isolation Based on Immunochemical Signatures through Surface Interactions.. 43
    Nanostructured Substrates for CTC Isolation 46
    Nanopillars and Nanowires 48
    Nanotextured PDMS 50
    Surface Coating with Nanomaterials 50
Chapter 3 LABEL-FREE iSOLATION OF METASTATIC TUMOR CELLS USING FILTER BASED MICROFLUIDIC DEVICE 54
Introduction.. 54

Experimental Section 55
Microdevice Design and Fabrication 55
Cell Culture 56
Experimental Setup and Procedure 57
Results and Discussion 59
Device Optimization and Calculation of Capture Efficiency 59
Detection of Cancer Cells from Blood 63
Conclusions 65
Chapter 4 NANOTEXTURED POLYMER SUBSTRATES FOR ENHANCED CANCER CELL ISOLATION AND CELL GROWTH 66
Introduction 66
Materials and Methods 67
Aptamer Preparation 67
Preparation of Nanotextured PDMS Substrates 69
Surface Characterization 69
Elemental Composition of the Samples 70
Contact Angle Measurements 70
Attachement of Anti-EGFR Aptamer on PDMS Substrates 70
Fluoresence Measurements 71
Human Glioblastoma and Astrocyte Cell Culture 72
Tumor and Astrocyte Cells Capture on Substrates 73
In vitro Cell Culture Studies on Nanotextured PDMS 73
Results and Discusion 74

Surface Topography of Nanotextured Substrates 74
Elemental Analysis and Compositional Mapping....................................... 75
Contact Angle Measurements.. 76
Fluorescence Measurements... 77
Isolation of hGBM and Astrocyte Cells.. 79
In vitro Cell Growth on Nanotextured Surfaces 82
Conclusions... 85
Chapter 5 NANOTEXTURED MICROFLUIDIC CHANNEL FOR ELECTRICAL PROFILING AND DETECTION OF TUMOR CELLS FROM BLOOD 86
Introduction.. 86
Materials and Methods 87
Device Fabrication 87
Device Characterization.. 88
Measurement Setup.. 88
Human Derived Primary Renal Cancer Cell Culture and Collection of Rat Blood 89
Results and Discussion 90
Surface Topography of Nanotextured Substrates 90
Device Assembly 90
Translocation Behavior of Tumor Cells through Plain and Nanotextured Microchannels 91

Translocation Behavior of Blood Cells in Plain and Nanotextured Microchannels........ 93
Pulse Shapes of Tumor and Blood Cells........ 96
Discrimination of Tumor and Blood Cells 97
Detection of Tumor Cells from Blood 98
Conclusions........ 100
Chapter 6 SINGLE BIOCHIP FOR THE DETECTION OF TUMOR CELLS EMPLOYING ELECTRICAL PROFILE AND SURFACE IMMOBILIZED APTAMERS........ 102
Introduction........ 102
Materials and Methods 104
Device Fabrication 104
Measurement Setup........ 105
Aptamer Preparation........ 106
Attachment of Anti-EGFR Aptamer on PDMS Surfaces 106
Culture of Human Glioblastoma (hGBM) Cells and Collection of Rat blood 107
Current Measurement and Capture of Cells in Microfluidic Device........ 108
Results and Discussion 109
Topography of Nanotextured Surfaces 109
Device Assembly 109
Determination of Cell Capture Efficiency........ 109
Electrical Measurement of Cells........ 112

Total Detection Efficiency.. 116

Isolation of hGBM and WBCs 116

Detection of Tumor Cells from Blood 119

Conclusions.. 121

Chapter 7 122

NANOTEXTUERD BARE COVERSLIP GLASS TO ENHANCE THE GROWTH OF PC12 CELLS 122

Introduction.. 122

Materials and Methods 124

Preparation of Nanotextured Glass Substrates.. 124

Surface Characterization using AFM 125

SEM and Elemental Composition of the Samples...................................... 125

Contact Angle Measurements.. 126

Culture and Treatment.. 126

Topography of Nanotextured Substrates 127

Data for Contact Angle Measurements 129

In Vitro Cell Growth on Nanotextured Surfaces 129

Nuclear Morphology of Cells... 131

Conclusion.. 133

Chapter 8 FUTURE RESEARCH DIRECTIONS.. 134

Introduction.. 134

Diagnosis from Cell Behavior... 134

Staging of Cancer... 135

  - Diagnosis of Bladder Cancer from Human Urine Samples.......................... 135
  - High Frequency Multiplexer for Microchannels to Record Cell Translocation Profiles 136

References... 138

Biographical Information 167

List of Illustrations

Figure 2-1: Mortality rates for different diseases except cancer has significantly dropped since 1950 [27]. This discloses the necessity of research and importance to find alternative detection and therapeutic approaches for cancer. 7

Figure 2-2: Two-hit theory of carcinogenesis: tumor formation in both hereditary and nonhereditary retinoblastoma [29]........ 8

Figure 2-3: Schematic demonstration of multistep tumor-host-interactions during metastasis [30] 9

Figure 2-4: Tumor cell invasion of extracellular membrane [31]. 10

Figure 2-5: Schematic to represent major steps involved in metastases [38]. 12

Figure 2-6: Amino acid sequence of EGF with disulfite bonds. The protein keeps its conformation with the help of disulfite bonds [39]. 13

Figure 2-7: Schematic diagram for processing steps of SELEX [54]. 17

Figure 2-8: SEM Images of lotus leaves (a) some lotus leaves on a pond, (b) water droplet floating on a leaf; (c) and (d) SEM micrographs of lotus leaves with different magnifications. The inset of (d) is showing the higher contact angle of water due to superhydrophobic property. Scale bar of (c) is 50 µm and (d) is 1 µm. Reprinted with permission [62] 19

Figure 2-9: Photos of ramee leaf with few water droplets (a) fron face; (b) rear face; SEM micrographs of ramee leaf (c), and (d) front face; (e), and (f) rear face; insets of (d) and (f) are showing the contact angles which are 38±2^o and 164±2^o, respectively. The scale bars for (c-f) are 100, 5, 100, and 5 µm, respectively. Reprinted with permission [62]. 21

Figure 2-10: Corneal epithelial basement membrane (a) SEM micrograph; (b) AFM image. Reprinted with permission [72].......... 25

Figure 2-11: Microfluidic device fabrication steps using soft lithography technique.......... 28

Figure 2-12: Schematic diagram of microfluidic devices to implement DEP techniques to detect cancer cells from blood sample, (a) a continuous-flow chamber for dielectrophoretic field-flow-fractionation (DEP-FFF) [105]; (b) optically induced-dielectrophoretic (ODEP) consisting six sections of moving light bars [106]. 33

Figure 2-13: Schematic diagram of microfluidic devices to implement cell-affinity micro-chromatography, (a) antibody coated micropost device [5]; (b) multi-well device to detect three types of cancer cells simultaneously using aptamer [53]; (c) long and multivalent DNA aptamer functionalized herringbone chip [26]. 36

Figure 2-14: Schematic diagram of magnetophoretic microdevice, (a) isolation of CTCs based on magnetophoretic signature [81]; (b) capture principle of a magnetic sifter [78]. 38

Figure 2-15: Microfluidic devices for the isolation of CTCs based on their mehcanophysical properties, (a) filtration using a 3D microfilter device and the applied forces (F_L) on a trapped cell [24]; (b) ratchet mechanism for cell-sorting [115]; (c) electrical and mechanical measurement of CTCs in a constriction channel [103].......... 44

Figure 2-16: Nanostructured substrates fabricated by different processes. SEM images of (a) silicon nanopillars produced by we chemical etching; (b) silicon nanowires (SiNWs) produced by vapor—liquid—solid method; (c) Magnified image of (SiNWs) bound to biotin-gold nanoparticles; (d) Au nanoclusters coated SiNWs prepared by rapid thermal chemical vapor deposition; (e) silica nanobeads deposited on glass; (f) TiO_2 nanofibers fabricated using electrospinning and calcinations; (g, h) micro needles and nanotextured surfaces were synthesized by chemical etching of chicken eggshell; (i) AFM image of nanotextured PDMS surface cured on chicken eggshell. Reprinted with permission. Reprinted with permission [121]. 52

Figure 3-1: Schematic diagram of the experimental setup and microfluidic channel device [157]. 58

Figure 3-2: Cell captured in microfluidic devices in case of (a) Device-1; (b) Device-2; (c) Device-3; and (d) Device-4. The scale bars in all micrographs are 50 µm. The right side of channels is inlet and the left is outlet as mentioned for (a) [157]. 59

Figure 3-3: Average of tumor cell capture efficiency of four devices (n=2) [157]. 60

Figure 3-4: Average diameters of the cells blocked by four devices [157]. 62

Figure 3-5: Blood introduced in (a) Device-3; and (b) Device-4. RBCs and WBCs passed through the microchannels. The scale bars are 50 µm [157]. 63

Figure 3-6: Isolation of cancer cells from rat blood using Device-4; micrographs of the devices (a) optical; (b) fluorescence. The scale bars are 50 µm [157]. 64

Figure 4-1: (a) Aptamer attachment protocol on nanotextured PDMS surfaces; (b) introduction of cell mixture on functionalized surface; (c) capturing target cells by aptamer grafted surface. 68

Figure 4-2: AFM micrographs of the plain and nanotextured PDMS surfaces. The micrographs represent (a) plain PDMS surface; nanotextured PDMS surfaces obtained by micro-RIE using O_2 and CF_4; (b) after 12 min (O_2:CF_4, 1:1); (c) after 12 min (O_2:CF_4, 1:2); and (d) after 25 min (O_2:CF_4, 1:1). Reprinted with permission [200].. 75

Figure 4-3: EDS elemental composition of (a) Plain PDMS and (b) Nanotextured PDMS (Surface-3) [200]. 76

Figure 4-4: Fluorescence intensity from AO stain [200] 77

Figure 4-5: The hGBM and astrocyte cells on the anti-EGFR aptamer modified surfaces; hGBM cells on (a) plain PDMS surface; (b) Surface-1; (c) Surface-2 and (d) Surface-3; and astrocyte cells on (e) plain PDMS surface; (f) Surface-1, (g) Surface-2 and (h) Surface-3. Scale bar = 100 µm in (a) is also applicable for (b)-(d) and (e) is also applicable for (f)-(h). Reprinted with permission [200]. 81

Figure 4-6: (a) The average cell density (cell number/mm^2) of hGBM and astrocyte cells on aptamer functionalized PDMS surfaces; (b) relationship of surface roughness and cell density of captured hGBM cells [200]. 82

Figure 4-7: The hGBM cell growth on plain and nanotextured surfaces as well as in the culture plate (a) plain PDMS surface; (b) Surface-1; (c) Surface-2; (d) Surface-3; and (e) the average cell densities (cell number/mm^2) for hGBM, astrocyte and fibroblast cells on all surfaces; Scale bar = 100 µm in (a) is also applicable for (b)-(d). Reprinted with permission [200].. 84

Figure 5-1: (a) Micrograph of the microchannel; (b) Measurement setup, syringe pump connected to the inlet of microfluidic device. One Ag/AgCl electrode is connected through the tubing at the inlet and another to the outlet. 89

Figure 5-2: Atomic force micrographs of (a) plain; and (b) nanotextured PDMS surfaces. Reprinted with permission [201]. 91

Figure 5-3: Translocation behavior of renal cancer cells through plain and nanotextured microchannels (a) characteristics plot for the cells; (b) average translocation time and (c) average peak amplitude (*n* ≈ 200). Reprinted with permission [201]. 93

Figure 5-4: Translocation behavior of blood cells in plain and nanotextured microchannels (*n ≈ 200)* 94

Figure 5-5: Representative electrical pulses of the translocated cells through the microchannels, (a) cancer cell through plain microchannel; (b) **c**ancer cell through nanotextured microchannel; (c) blood through nanotextured PDMS microchannel;, close-up of electrical pulses of some blood cells through (d, e) plain and (f) nanotextured PDMS microchannel. Reprinted with permission [201]. 95

Figure 5-6: Representative translocation data of blood and renal cancer cells through (a) plain and (b) nanotextured microchannels (*n*≈ 200). Reprinted with permission [201]. 99

Figure 5-7: Data plots for blood cells through (a) plain and (b) nanotextured microchannels; data plots for cancer cells spiked in blood through (c) plain and (d) nanotextured microchannels. The typical region of detected cancer cells are enclosed in dotted green circle. Reprinted with permission [201]. 101

Figure 6-1: Schematic diagram of the microfluidic device consisted inlet, outlet and nanotextured cell capture zone which is functionalized with anti-EGFR aptamers. Current was measured across two microchannels using Ag/AgCl electrodes. 105

Figure 6-2: AFM micrographs of (a) plain; and (b) nanotextured PDMS surfaces. 108

Figure 6-3: Cell capture efficiencies in anti-EGFR aptamer functionalized nanotextured PDMS channels at different flow velocities (a) cell capture efficiencies for hGBM and WBCs are shown using blue and green marker; captured cells; (b) hGBM cells and (c) WBCs; 100 μm scale bar is for both (b) and (c). 110

Figure 6-4: Forces working on EGFR overexpressed tumor cell in aptamer functionalized nanotextured PDMS channel. 114

Figure 6-5: Electrical data and translocation behavior of hGBM and WBCs through microchannels, (a) distribution of the pulses for two types of cells where average translocation time and peak amplitude of current both are higher for hGBM cells; electrical profile of the translocated cells through the microchannel (b) hGBM cell ; (c) WBC. 115

Figure 7-1: AFM micrographs of the (a) plain and (b) nanotextured PDMS surfaces.......... 127

Figure 7-2: (a) SEM micrograph of a nanotextured glass substrate; EDS elemental composition of (b) plain and (c) nanotextured coverslip glasses...... 128

Figure 7-3: Micrographs of PC 12 cells grown on numerous substrates under following conditions: (a) TCP; (b) plain cover glass; (c) nanotopology; surfaces were coated with 100 ng/ml NGB β (d) TCP; (e) plain cover glass; (f) nanotopology; (g) density of PC 12 cells (cell number/mm^2) on all the experimental surfaces. 131

Figure 7-4: Micrographs of DAPI stained cell nuclei of PC12 cells under the treatment of NGF β on (a) TCP; (b) plain cover glass; (c) nanotopology surfaces; (d) quantification of pyknotic nuclei on various surfaces. 132

Figure 8-1: Demonstrates the use of high speed multiplexer to increase the channels four times in the microchannel array assembly. 137

List of Tables

Table 2-1: The overexpressed protein for different cancers. EGFR is common for all types of cancers. 14

Table 2-2: The percentage of EGFR overexpression in the different cancer types. 15

Table 2-3: Comparison between antibody and aptamer. 16

Table 2-4: Functions of micro- and nanoscale structures observed in nature [69]: 22

Table 2-5: Nanostructure preparation techniques and their minimum feature size [121]. 47

Table 4-1: Contact angles measured on bare surfaces and after chemical activation with phenylene di-isothiocyanate (PDITC)) *(n=5)* 77

Chapter 1

INTRODUCTION

Cancer is a prime public health problem all over the world. This is a fatal disease provoked by the uncontrolled growth of cells that seize adjacent tissues and metastasize to remote sites within the body [1]. Though definite reasons of cancer are not revealed yet, six biological capabilities are ascertained as hallmarks of cancer which are sustaining proliferative signaling, evading growth suppressors, resisting cell death, enabling replicative immortality, inducing angiogenesis, and activating invasion and metastasis [2]. Only 5-10% of cancer is attributed to genetic defects and remaining cases originated from the lifestyle and environment. Tobacco use, diet, alcohol, radiation, infections, stress, obesity, and physical inactivity are identified as major constituent in lifestyle which causes cancer [3]. Asymptomatic nature is the predominant impediment for the diagnosis of cancer at early stage. Prevalent diagnosis techniques are challenged in yield, purity, complexity, cost, and tedious processes and also invasiveness. Hence, one of the major focuses of researchers is to develop point-of-care devices for the early detection of cancer. The circulating tumor cells (CTCs) were introduced in nineteenth century by Thomas Ashworth. Detection and enumeration of CTCs is a promising field for the diagnosis, prognosis, assessing metastatic progression and tracking therapeutic efficiency of cancer patients [4]. The CTCs are emerging as cancer biomarkers. These migrate into the vasculature from an indigenous tumor and disseminate in the bloodstream [5]. CTCs are found in the blood for majority of the cancer patients. CTCs separate from the solid tumor and wander through blood to form secondary tumors [6, 7]. This process of triggering secondary tumor is known as metastasis. It is hard to save a patient once metastasis starts. To prevent metastasis, CTCs are required to be detected at very early stages of cancer. But exceedingly low number of CTCs at early stage, ranging from 1-200 in 1 mL of blood makes it extremely challenging to recognize them [6]. Again, the number of blood cells and their mechanophysical properties in a healthy person can vary over a wide range. Consequently, detection and enumeration of CTCs demand acutely sensitive and selective scheme which is extremely strenuous to develop. The primary focus of this dissertation is to develop an inexpensive, portable and user friendly point-of-care (POC) device for the efficient detection and isolation of tumor cells.

Research Overview

The central focus of the research was to develop inexpensive and efficient point-of-care devices for the early detection of cancer. Chapter 3 concentrates on filter typed microfluidic channel device to isolate tumor cells. This device considered the mechanical and physical properties of cancer cells to distinguish them from blood. Chapter 4 investigates the isolation of epidermal growth factor receptor (EGFR) overexpressing cancer cells through aptamer-functionalized nanotextured polydimethylsiloxane (PDMS) surfaces. This approach utilized the aptamer-protein and cell-surface interactions for early cancer detection. Chapter 5 studies the electrical profile of cells obtained from ionic current measurement across microchannels. The goal of this technique was to discriminate tumor cells from blood based on their mechanophysical properties. Chapter 6 focuses on a microfluidic device which employed aptamer functionalized nanotextured surface and electrical profile determination scheme simultaneously to detect tumor cells from blood.

Label-Free Isolation of Metastatic Tumor Cells Using Filter Based Microfluidic device

CTCs have significant diagnostic value for cancer patients. We reported a label-free, simple and rapid microchannel filter type device for isolation of metastatic renal cancer cells based on their mechanophysical properties like size and deformability. The microdevice fabricated from PDMS using soft lithography contained one inlet and one outlet connected via several hundreds of microchannels. It was observed that metastatic renal cancer cells were highly elastic and squeezed through microchannels much smaller than their sizes. Using a reverse-selectivity approach, the number of microchannels and their dimensions were varied to optimize and reduce the shear stress on tumor cells such that these did not pass through filtering channels. Consequently cancer cells were isolated from blood with substantial efficiency.

Nanotextured Polymer Substrates for Enhanced Cancer Cell Isolation and Cell Growth

Detection of circulating tumor cells (CTCs) in the early stages of cancer is very promising because of their very small number. Highly sensitive approach is required to differentiate tumor cells from other cells. We composed nanotextured PDMS substrates by micro reactive ion etching (Micro-RIE) to have better control on surface morphology. Nanotextured improved the affinity of PDMS surfaces to capture cancer cells using surface immobilized aptamers. The aptamers were specific to EGFR present in cell membranes, and overexpressed in tumor cells. We also investigated the effect of nanoscale features on cell growth. The proliferation rate of tumor cells was also higher in nanotextured PDMS surfaces. The nanotextured PDMS substrates are thus useful for cancer cytology devices.

Nanotextured Microfluidic Channel for Electrical Profiling and Detection of Tumor Cells from Blood

Single microfluidic channel was used to detect and discriminate cancer cells based on translocation behavior. The ionic current was measured across microfluidic channel to characterize tumor cells based on their mechanical and physical properties. The tumor cells showed characteristic electrical signals which were easily distinguished from blood cells. The channel was fabricated in PDMS using soft lithography. First of all, plain microchannel was used to differentiate tumor cells from blood. Next, nanotexture was introduced in microchannel to enhance the disparity in translocation behavior of tumor cells from red blood cells (RBCs) and white blood cells (WBCs). Dimensions of the microchannel did not allow more than one cell to pass through simultaneously. This approach provided rapid detection of metastatic tumor cells from blood.

Single Biochip for the Detection of Tumor Cells by Electrical Profile and Surface Immobilized Aptamer

We reported a simple microfluidic device to detect tumor cells using surface grafted anti-EGFR ribonucleic acid (RNA) aptamers and translocation behavior simultaneously. Nanotextured PDMS surface of the microchannel was functionalized with aptamers to capture EGFR overexpressed human glioblastoma (hGBM) cells.

Microchannels were used to discriminate tumor cells based on their translocation behavior at single cell level. The overall detection of cancer cells relied on both overexpression of EGFR on cell membrane and mechanophysical properties of the cells. This multistage detection device can be implemented in a lab-on-a-chip setting for the early diagnosis of cancer.

Chapter 2

BACKGROUND AND REVIEW

In spite of extensive multidisciplinary research, the mortality rate from cancer still remains very high shown in Figure 2-1. In 2014, a total of 1,665,540 new cancer cases and 585,720 deaths from cancer were projected to occur in the United States alone [8]. Despite massive technological advances every year nearly two million Americans are diagnosed with cancer. Unlike other diseases, deep evolutionary root of cancer is still untangled. Only some genetic and environmental factors are suggested accountable for the cancer. Uncovering the roots of cancer, its diagnosis, prognosis and finding magic-bullet to cure it have been most promising tasks in human endeavor against cancer.

For cancer, symptoms are not perceived until the disease has reached an advanced stage. Cancer is often diagnosed at very advanced stages which delays the timely treatment and leads to poor prognosis. Insufficient progress has been made in the early diagnosis and screening of cancer and enormous costs are associated with the prevalent methods. A non-invasive diagnostic scheme through bodily fluid is a challenge as CTCs are extremely rare (~5 in billion of normal cells) in blood. The physical and chemical properties of tumor cells vary extensively and therefore, highly sensitive approaches are required to detect them.

Conventional cancer cell sorting techniques including centrifugation, chromatography, and fluorescence and magnetic-activated cell sorting (FACS and MACS) are restricted in yield and purity [9]. As a result, microfluidic systems have emerged in early twentieth century as fascinating platforms to detect CTCs. Microfluidic devices are conducive for small sample volumes, fast processing times, multiplexing capabilities and large surface-to-volume ratios [1, 10, 11]. Manifold microfluidic platforms based techniques have been developed to recognize and quantify CTCs, which are primarily classified as dielectrophoresis (DEP) [12], cell-affinity micro-chromatography [5, 13-15], magnetophoresis [16-21], and mechanophysical properties based schemes [22-26]. However, before earnest discussion about these techniques, the roots and precursors of cancers must be brought into light.

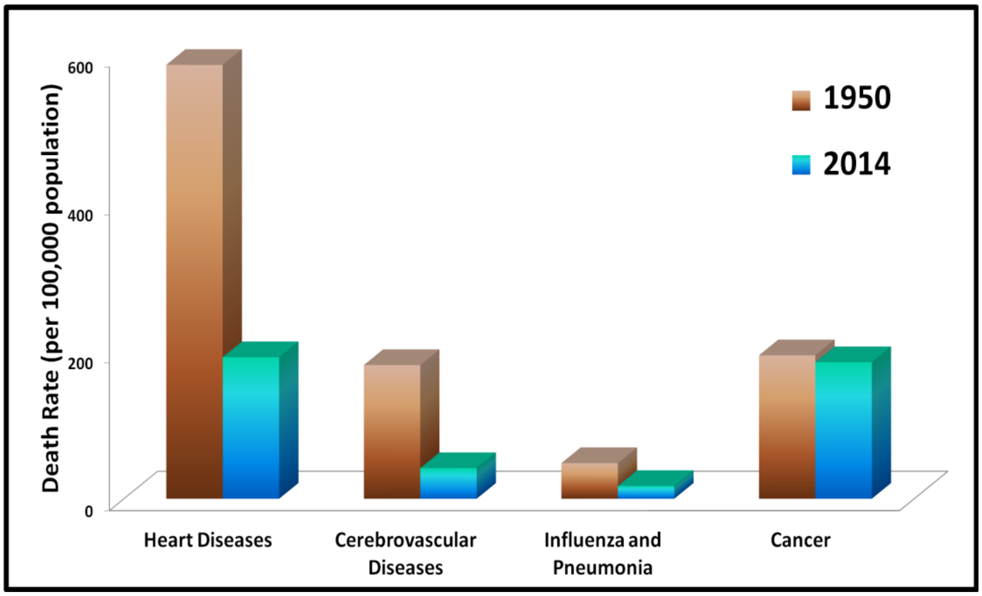

Figure 2-1: Mortality rates for many diseases except cancer have significantly dropped since 1950 [27]. This shows the necessity of research and importance to find alternative detection and therapeutic approaches for cancer.

Origin of Cancer

Cancer is a common name for a large group of diseases. At earlier age normal cells divide faster to allow the growth of the person and in adult years, cells divide only to replace dying cells or to repair injuries shown in Figure 2-2. Cancer is initiated when cells start growing in uncontrolled ways and do not die. Healthy cells mutate to cancer cells due to the damage of deoxyribonucleic acid (DNA). DNA basically drives the actions of cells. In healthy cells the damage is either fixed or cells die. On the other hand, in cancer patients, the cell engenders unwanted and identical cells. This evolution process of generating cancer cells from normal cells is called carcinogenesis. After series of mutations of genes, a cancer cell goes into unbounded growth and becomes malignant [28]. Cancer occurs after several somatic mutations. According to the two hit hypothesis by Dr. Alfred Knudson, inheriting one germ line copy of a damaged gene augments the probability of cancer [29].

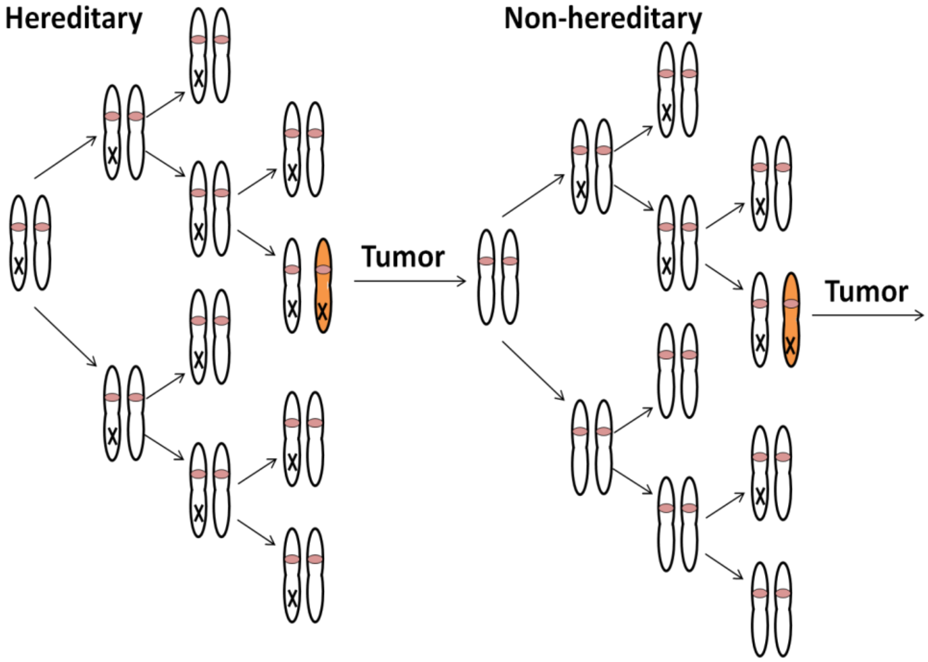

Figure 2-2: Two-hit theory of carcinogenesis: tumor formation in both hereditary and nonhereditary retinoblastoma [29].

Cancer Metastasis

The way of spreading and killing of their host organisms by tumor remains an enigma. However, most of the cancer deaths are result of metastatic disease. Cancer cells can disseminate from original site to a distant part of the body to engender secondary tumor. This entire process is known as metastasis. A complex series of tumor-host-interactions occur before metastatic colony is developed as shown in Figure 2-3. Primary tumor cells enter to host vasculature due to local invasion. Through blood stream these cells are transferred to remote organs to provoke metastatic colony followed by angiogenesis [30]. Various molecular interactions occur within microenvironment of tumor during primary tumor progression to the growth of macrometastasis. The invasive tumor has to interplay with extracellular matrix at many stages of metastasis.

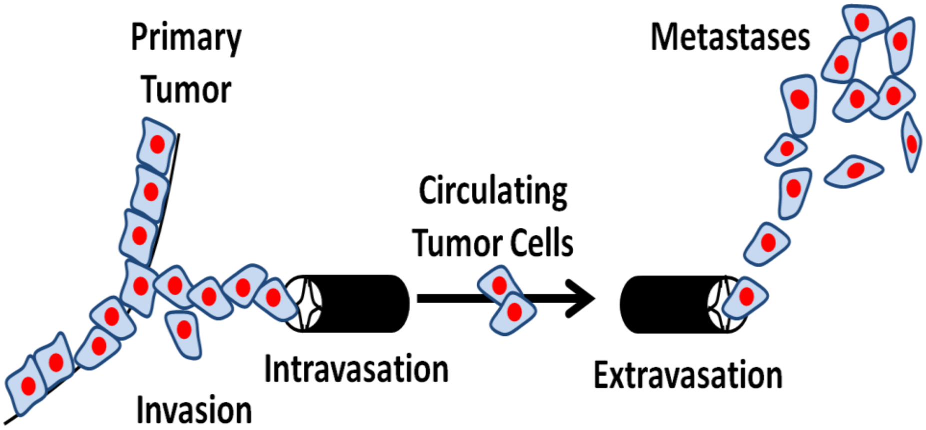

Figure 2-3: Schematic demonstration of multistep tumor-host-interactions during metastasis [30].

The invasion of tumor cell to extracelluar matrix has been illustrated in Figure 2-

4. First, specific binding to the matrix occurs followed by local degradation of matrix and the binding components due to the secreted hydrolytic enzymes. Last step is the locomotion of tumor cell into the matrix region altered by proteolysis.

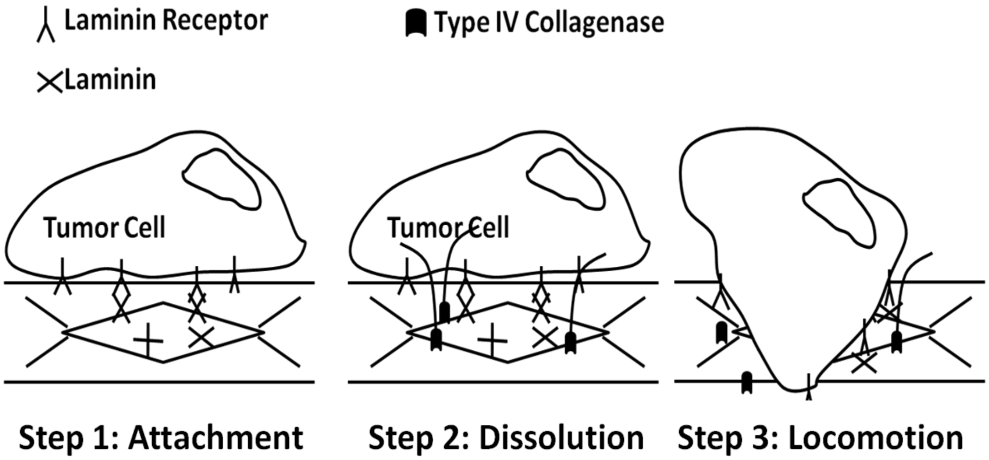

Figure 2-4: Tumor cell invasion of extracellular membrane [31].

Epithelial cells have significant structural and functional role in body organs. They are attached with each other by cadherins and to extracellular matrix (ECM) junctions by integrins. Epithelium cells are generally rigid and immobile whereas mesenchymal cells like leukocytes and fibroblasts have very flexible organization. Transition from epithelial to mesenchymal cells (EMT) is involved in tumor cell invasion. Mesenchymal-like cancer cells have high motility and can intravasate and extravasate by traversing basement membrane, interstitial gaps and endothelial barriers very easily. In blood vessels, CTCs go through apoptosis or circulate as isolated CTCs. These cells cannot proliferate in the blood vessels. When cancer cells reach the target, the reverse transition takes place from mesenchymal to epithelial transition (MET). That means cancer cells become epithelial-like cells and start cell proliferation again [32, 33]. Figure 2-5 depicts all the steps of tumor invasion and metastasis.

Epidermal Growth Factor (EGF) and Epidermal Growth Factor Receptor (EGFR)

For cancer diagnosis, a number of proteins and growth factors have been identified. These molecules are either overexpressed or downregulated in cancer cells. We have focused on epidermal growth factor receptor (EGFR) for the detection of cancer cells.

Epidermal Growth Factor

Cells are required to take molecular cues to multiply in human body. Tissues generally communicate through growth factors to control growth levels within normal limits and EGF is a biological signaling molecule for cell proliferation and differentiation (Figure 2-6). But cancer cells are often empowered by EGF and its receptor to grow without considering the consequences to their neighbor [34]. Molecular weight of human EGF is 6045 kDa consisting of 53 amino acid residues [35]. The molecule can specifically identify EGF receptor on the cell surface. The dissociation constant of the pair is ~2–4 × 10^{-10} M [36]. After reaching the cell surface, EGF are distributed arbitrarily on EGFR sites and leading to saturation of EGFRs by rapid binding. After the formation of EGF-EGFR complex, EGF is internalized via receptor mediated endocytosis and degrades in lysosomes. EGFRs are recycled in endosome and migrate again to the cell surface [37].

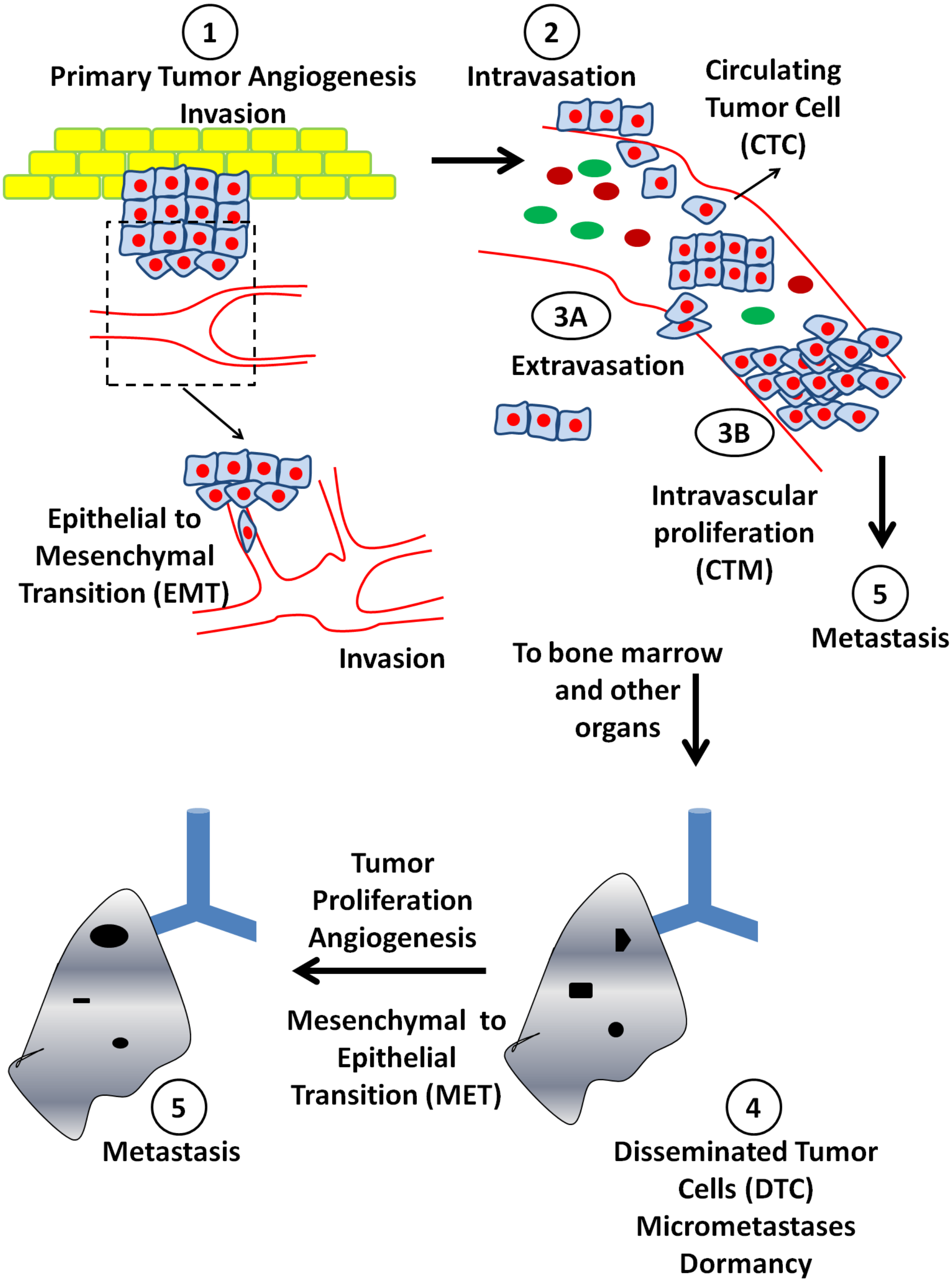

Figure 2-5: Schematic to represent major steps involved in metastases [38].

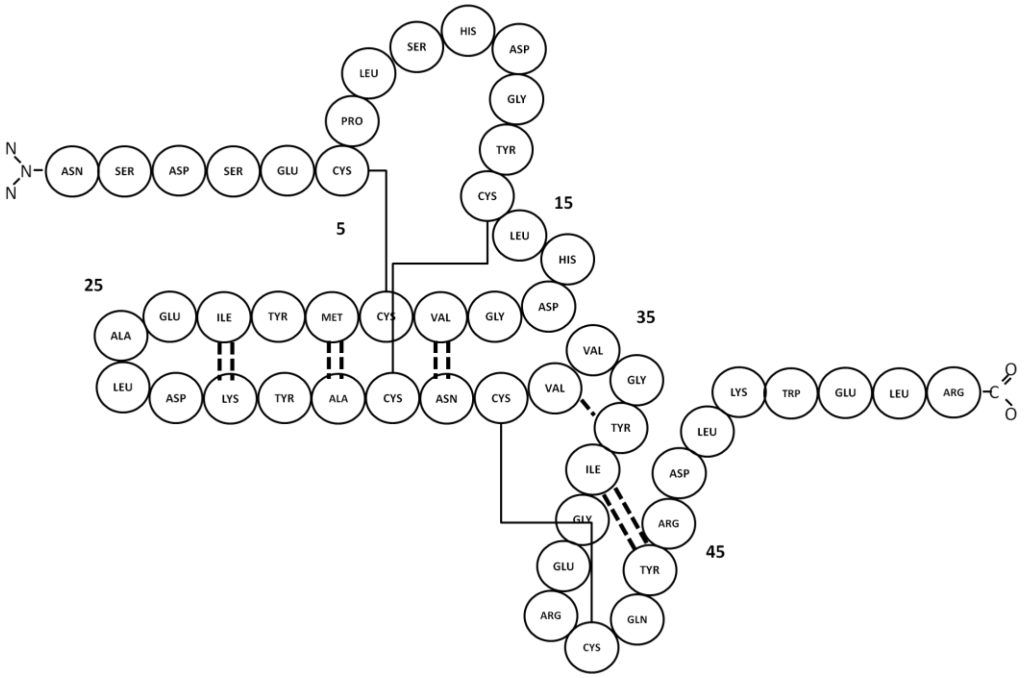

Figure 2-6: Amino acid sequence of EGF with disulfite bonds. The protein keeps its conformation with the help of disulfite bonds [39].

Epidermal Growth Factor Receptor (EGFR)

EGFR is basically a transmembrane glycoprotein that can recognize and bind to the protein members of the EGF-family (EGF, TGF-α, etc.). Molecular weight of this molecule is 170 kDa [40]. There are four functional domains of the molecule; an extracellular ligand-binding domain; a transmembrane domain; an intracellular tyrosine kinase domain, and a C-terminal regulatory domain [41]. The EGFR gene is often mutated or amplified in cancer cells and leads to metastasis [42, 43]. EGFR has significant importance in cellular functions such as DNA synthesis, cell proliferation, migration, adhesion etc. 40,000 to 100,000 EGFR count has been reported on the membrane of healthy cells [44]. In many cancer cells, EGFR is usually overexpressed 10 to 100 times and thus it is a fascinating target for cancer detection and treatment. Table 2-1 shows a list of cancers for which EGFR is known to be overexpressed and the percentage of EGFR overexpression for various cancers is shown in Table 2-2.

Table 2-1: The overexpressed protein for different cancers. EGFR is common for all types of cancers.

Disease	Biomarker
Breast Cancer	CEA, HER-2, EGFR
Cervical Cancer	Human Pappiloma Virus, EGFR
Lung Cancer	EGFR, KRAS, BRAF
Bladder Cancer	EGFR, HSP27, Annexin
Ovarian Cancer	EGFR, Haptaglobin α, CA-125
Esophageal Cancer	EGFR, Periplakin

Circulating Tumor Cells (CTCs)

Cancer cells that migrate into the vasculature from a primary tumor and circulate in the blood stream are known as CTCs. CTCs are found in peripheral blood for the majority of the cancer patients. CTCs can stimulate secondary tumor cells. CTCs are promising biomarker for the diagnosis, prognosis and post-treatment monitoring of cancer patients. The presence of CTCs can be responsible for the cancer-related deaths [45, 46]. The survival rate of cancer patients are also related to the concentration of CTCs in blood. Therefore precise enumeration and detection of

CTCs are key interests for contemporary researchers.

Table 2-2: The percentage of EGFR overexpression in the different cancer types.

Tumor Type	% of Tumors Overexpressing EGFR
Head & Neck	80-100
Kidney	50-90
Lung	40-80
Glioma	40-50
Ovarian	35-70
Bladder	31-48
Pancreatic	30-50
Colon	25-77
Breast	14-91

Possible Detection Molecules: DNA/RNA Aptamer and Antibody

Detection and sorting based on affinity interactions is expected to have higher efficiency and greater specificity compared to mechanical and electrical sorting techniques [47]. Affinity-based approaches rely on antibodies and aptamers. Antibody is Y-shaped large protein produced by plasma cells. Immune system uses it to identify and neutralize foreign objects. Aptamers are single stranded oligonucleic acid or peptide molecules that can selectively bind to specific target molecules. Majority of the affinity-based approaches rely on antibodies which are often subject to high levels of off-target cross-reactivity [48]. Some drawbacks of antibodies are: (i) their shelf life is limited and can be denatured easily; (ii) definite physiological conditions are required for antibody-antigen binding; (iii) batch to batch variation; (iv) animals are required for the production of antibody; (v) kinetic parameters of antibody-antigen interactions cannot be altered; (vi) labeling cost may cause loss in function; (vii) heterogeneity of conjugation on device surface and (viii) cost [49]. Aptamers have emerged with great opportunities in cancer diagnosis and therapeutics. Aptamers have high affinities and specificities comparable with those of antibodies and have more advantages. Due to the lack of large hydrophobic cores of proteins, aptamers do not aggregate. They are stable at wide ranges of pH, temperature, and salt and ionic conditions, and can be reversibly denatured. Aptamers can be synthesized chemically in vitro. For aptamers, selection conditions can be manipulated to obtain desirable properties for in vitro analysis [50, 51]. Moreover, as aptamers are highly hydrophilic than antibodies they

Table 2-3: Comparison between antibody and aptamer.

Antibody	Aptamer
Low specificity and sensitivity	High specificity and sensitivity
Biological system is required for production	In vitro production
Targets are limited	Virtually any target molecule
Labeling of antibody may lead to loss in affinity	Functional group can be attached without losing affinity
Antibodies have limited shelf life and are sensitive to temperature	Long shelf life and stable under temperature fluctuation.
Batch to batch variation	Very little or no batch to batch variation

can provide surface passivation against nonspecific binding. Aptamers have been used for cell labeling studies [52], activating cell signaling pathways and for the detection and isolation of cells [53]. In this work, anti-EGFR aptamer was used for the isolation of cancer cells. Table 2-3 summarizes the comparison of antibodies and aptamers.

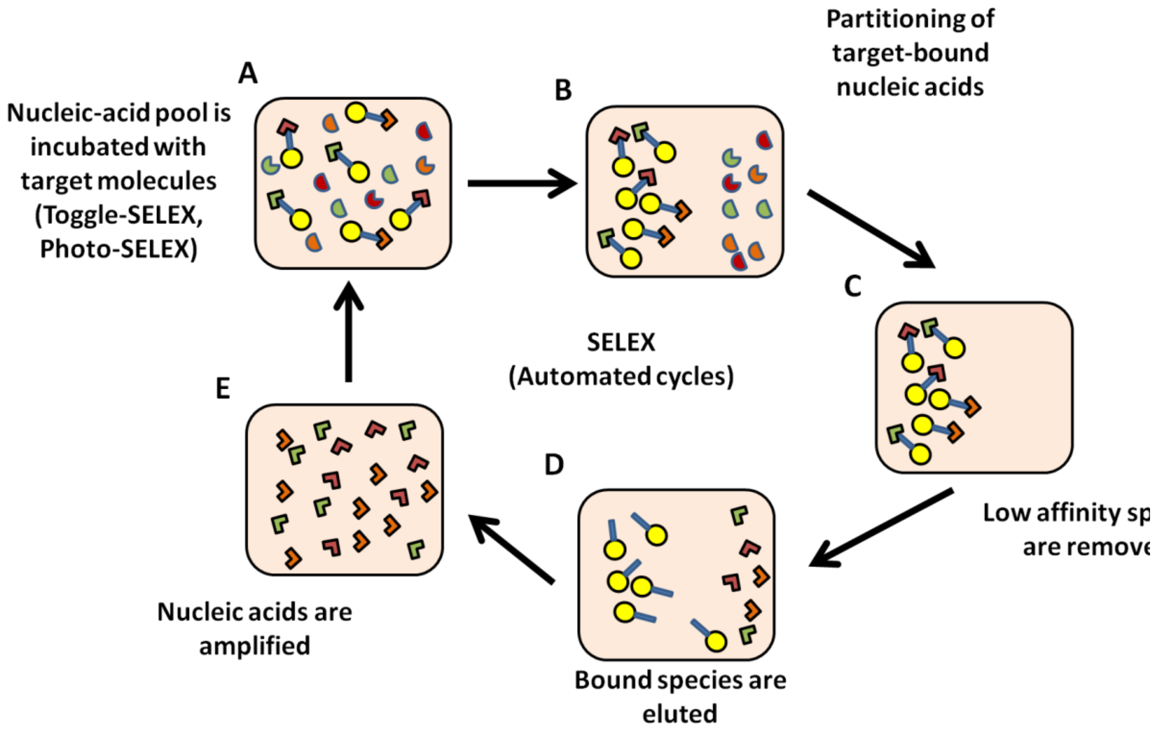

Figure 2-7: Schematic diagram for processing steps of SELEX [54].

Systematic Evolution of Ligands by EXponential enrichment (SELEX)

In vitro technique to prepare aptamers was developed in 1990 which is called Systematic Evolution of Ligands by EXponential enrichment (SELEX) shown in Figure 2-6 [55, 56]. This discovery of aptamers with specific catalytic properties or functions in gene regulation have led to re-evaluation of biological importance of these molecules

[57]. First of all, oligonucleotide library of randomly generated sequence of specific length is prepared. As there are four nucleotides (A, T, C and G), the total number of possible sequences in the library is 4^n. These sequences are introduced to the target ligand and unbound sequences are eliminated. After primary filtration, the sequences are further amplified by PCR. In the subsequent steps of selection, their binding specificity and binding affinity are examined to realize the strongest binding sequences with high specificity [58]. Target ligand can be a protein, small organic compound, or even an entire cell [59]. Aptamers have very short half life but after 2'-fluorine-substituted pyrimidine modification, aptamers are available even for weeks. Peptide aptamers and their selection process is different [60].

Multiscale Structures in Nature

Nature has been using nanotechnology long before human even thought of it. Nanotexture is observed in nature on the external and internal surfaces of animals, insects, human body, and plants. These surfaces are exceedingly sophisticated with the ability to serve multiple functions and provide new insights into the design of biomimectic artificial structures to serve numerous purposes. Here we are going to discuss the nanostructures observed in insects/animals, plants, and human body.

Nanostructures in Plants and Insect

Various leaves have nanostructures which yield self-cleaning superhydrophobic (contact angle is higher than 150^o for water droplet) surfaces. Lotus is superhydrophobic in nature which leads to its popular self-cleaning property known as "lotus effect" [61]. Initially, it was hypothesized that micrometer-scale papillae structure on the leaf is responsible for this property. But later it was observed that the micro- and nanoscale hierarchical structures are accountable for that. Randomly distributed papillae with diameters ranging from 5-9 µm had further nanostructured branches with average

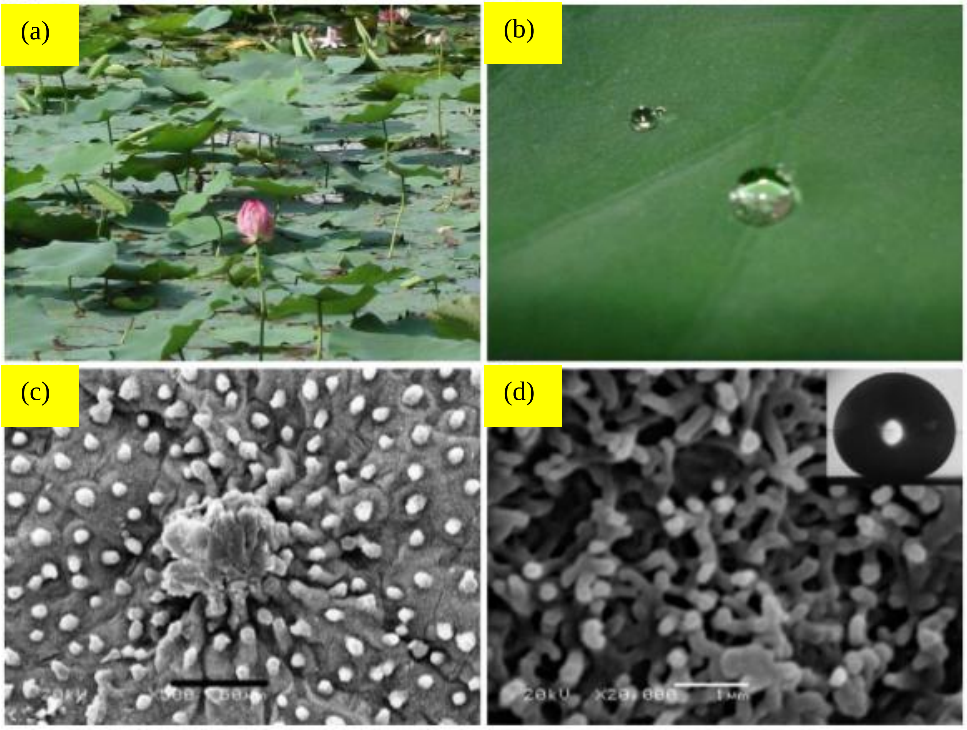

Figure 2-8: SEM Images of lotus leaves (a) some lotus leaves on a pond, (b) water droplet floating on a leaf; (c) and (d) SEM micrographs of lotus leaves with different magnifications. The inset of (d) is showing the higher contact angle of water due to superhydrophobic property. Scale bar of (c) is 50 µm and (d) is 1 µm. Reprinted with permission [62] .

diameter of 124.3 nm. Figure 2-8(a) and (b) show the photos of lotus leaves and water droplet floating on it, respectively [62]. Figure 2-8 (c) and (d) are SEM micrographs of lotus leaves and the contact angle of water droplet with a value of 161 ± 2^{o} is shown in inset of Figure 2-8(d). Higher contact angle represents the superhydrophobic nature of lotus leaves. Similar hierarchical structure was also observed in rice leaf [61]. Rice leaves have anisotropic surface architecture which also has significant influence on wettability [62]. Hierarchical micropapillae and nanofolds also exist on the petals' surfaces of red roses which provide sufficient roughness for superhydrophobicity and a high adhesive force with water. On the surface of rose petal, a water droplet appears spherical in shape, which does not roll off even when the petal is turned upside down and this phenomenon is defined as the "petal effect" [63]. Some other plants have also shown similar characteristics due to their hierarchical structures such as taro leaves, and india canna flower [62]. All these plants can trap a large amount of air on their surface, lowering their surface free energy. For these plants only frontal face showed hydrophobic properties because the rear surfaces have different structures. On the other hand, purple setcreasea has unique micro-nanoscale structures on both sides [62]. Many micro-hexagons, consisting of branch-like nanostructures (with average diameters of 250 nm) are randomly distributed on the surface. Plant leaves of perfoliate knotweed also showed similar structures on both the surfaces. An interesting phenomenon has been observed for ramee leaf. Frontal face of ramee leaf shows only micro-fiber structures which leads to hydrophilic property. But the rear face of this leaf has fibers with diameter of 1 to 2 µm formed a unitary structure to make it superhydrophobic. Figure 2-9 shows the images of ramee leaf [62]. Figure 2-9(a) and (b) are photos of front and rear face of ramee leaf with few water droplets, respecitvely.

Figure 2-9(c), and (d) are SEM micrographs of frontal face and (e), and (f) are of rear face of ramee leaves . The inset of (d), and (f) show the contact angles of water droplet (38±2^{o} and 164±2^{o}, respectively). The contact angles show hydrophilicity and hydrophobicity of front and rear face of ramee leaf, respectively. Chinese watermelon has also been shown to have similar structures and properties as ramee leaf [62].

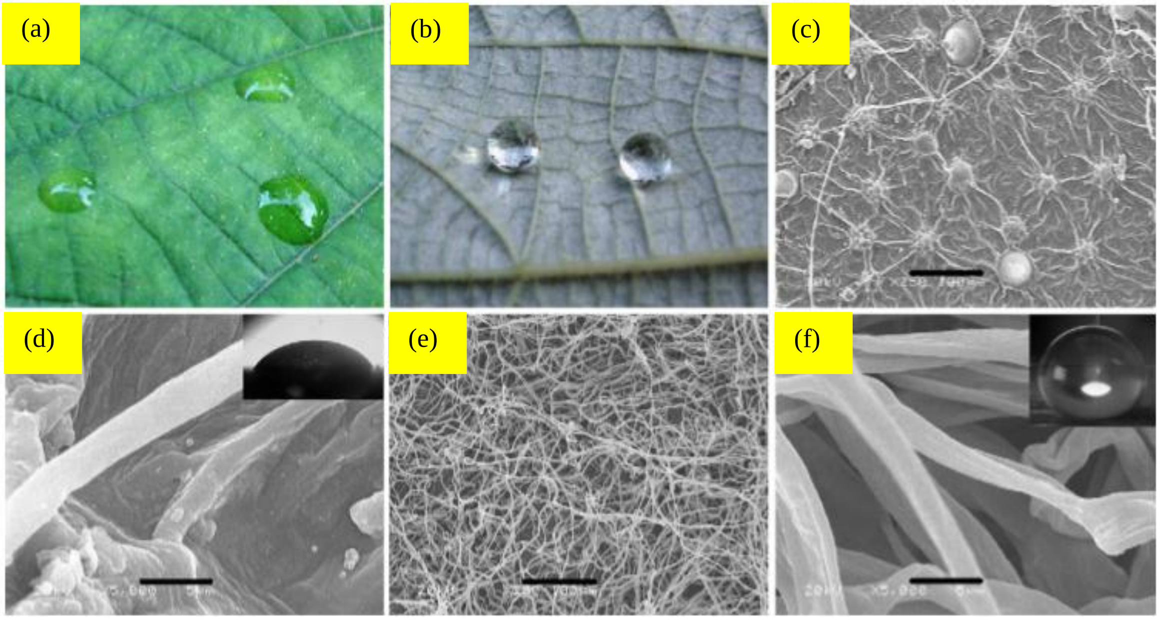

Figure 2-9: Photos of ramee leaf with few water droplets (a) fron face; (b) rear face; SEM micrographs of ramee leaf (c), and (d) front face; (e), and (f) rear face; insets of (d) and (f) are showing the contact angles which are 38±2^{o} and 164±2^{o}, respectively. The scale bars for (c-f) are 100, 5, 100, and 5 µm, respectively. Reprinted with permission [62].

Table 2-4: Functions of micro- and nanoscale structures observed in nature [64]:

Functions	Biological materials
Superhydrophobicity	Butterfly wing, cicada wing, water strider leg, Fish scale, Gecko foot, Mosquito compound eye, Peacock feather Lotus leaf, Rice leaf, Rose petal, India canna flower, Perfoliate knotweed
Anisotropic wettability	Rice leaf
Self-cleaning	Butterfly wing, Fish scale, Gecko foot Lotus leaf
Adhesion	Butterfly wing, Fish scale, Gecko foot, Spider capture silk Lotus leaf, Rose petal
Structural color	Butterfly wing, Nacre, Peacock feather, Rose petal
Chemical sensing capability	Butterfly wing
Mechanical functions	Brittlestar, Nacre, Spicule, Spider capture silk, Spider dragline silk
Optical functions	Butterfly wing, cicada wing, Mosquito compound eye, Polar bear fur, Spicule
Superoleophilicity	Fish scale
Anti-biofouling	Shark skin
Water collection ability	Spider capture silk

Nanostructures in Insects

Micro- and nanoscale structures are also observed in insects. Needle-shaped hierarchical structures are found on the legs of water striders which help them to stand, and move quickly on water surface [65]. Hydrophobic wax-coated, and hydrophilic non-waxy bumps on the modified hardened forewings (called elytra) of a desert beetle allow it to efficiently capture water [66]. In these cases, the interactions of hierarchical structures with water are very important to effect the function of biological surfaces. These interactions can be described in terms of two states which are known as Wenzel state and Cassie-Baxter state. In Wenzel state, a liquid droplet completely wets the asperities of a rough surface [67], and in the Cassie-Baxter state, a liquid droplet is suspended on the top of a rough surface and leaves air pockets inside the texture [68]. Droplets can transit from the higher energy Cassie-Baxter state to the lower energy Wenzel state by filling liquid into the asperities and forming more stable homogeneous interface [69]. The Cassie-Baxter state generally produces superhydrophobicity, which is directly related to both the chemical composition and the geometry of the surface. This is useful for various applications requiring surfaces that are self cleaning, waterproof, and/or have low drag in water. Micro- and nanoscale structures are helpful for various functions in plant and insects which are summarized in Table 2-4 [64].

Nanostructures in Human Body

Nanostructures are also observed in various human tissues and have significant impact on their proper functioning. Vascular endothelial basement membranes have three dimensional nanostructured topography which influences the cell function significantly [70]. This topographic feature has been thoroughly characterized using TEM, and SEM. Topographic features, present in the aorta, carotid, saphenous, and inferior vena cava vessels in the rhesus macaque were analyzed quantitatively. Vascular basement membranes are comprised of a complex meshwork consisting of pores and fibers in the submicron range, (100 - 1000 nm) and nanoscale (1–100 nm) range. The thickness of basement membrane, diameter of pore, and fiber substantially vary depending on the location and physical properties of the vessel. Nanoscale topography of the basement membrane underlying the anterior corneal epithelium of the macaque has also been analyzed quantitatively [71]. The characterization of the basement membrane was performed using high-resolution and low-voltage SEM, TEM, and AFM. Mean diameter of the fiber and pore was 77±44 and 72±40 nm, respectively with pores occupying approximately 15% of the total surface area. Similar features and dimensions were also observed for Matrigel, a commercially available basement membrane like complex. These nanoscale features may influence the fundamental cell behaviors such as adhesion, migration, proliferation, and differentiation. Quantitative characterization of the topographic features of the native aortic valve endothelial basement membrane has also been performed [72]. The basement membrane of aortic valve showed rich 3-D nanoscale topography consisting of pores, fibers and elevations [70]. All the measured features were in sub-100 nm range. There was no statistical difference between the fibrosal and ventricular surfaces of the cusp. Recent studies suggest that the absence of viable layer of endothelial cells on the basement membrane of bioprosthetic heart valves may be one of the causes of calcification and subsequent valve failure [72-74]. The subepithelial and subendothelial basement membrane surfaces of human cornea also have a similar appearance that consists of an interwoven meshwork of nanoscale fibers and pores [75]. The nanotopographic features are fractile in nature and provide larger surface area for cell contact. The corneal basement membrane topography (Figure 2-10) has significant impact on the function of the overlying cells. By analyzing AFM micrographs, it was observed that the distance between peak topographic features for epithelial basement membrane was 27±8 nm and the mean lateral distance between elevated topographic features was 25±11 nm. Average surface area for this membrane was 65% greater than that for an infinite surface of identical lateral dimensions. The fractal dimension of the epithelial basement membrane was ~2.2 which indicated both roughness, and regularly repeating surface.

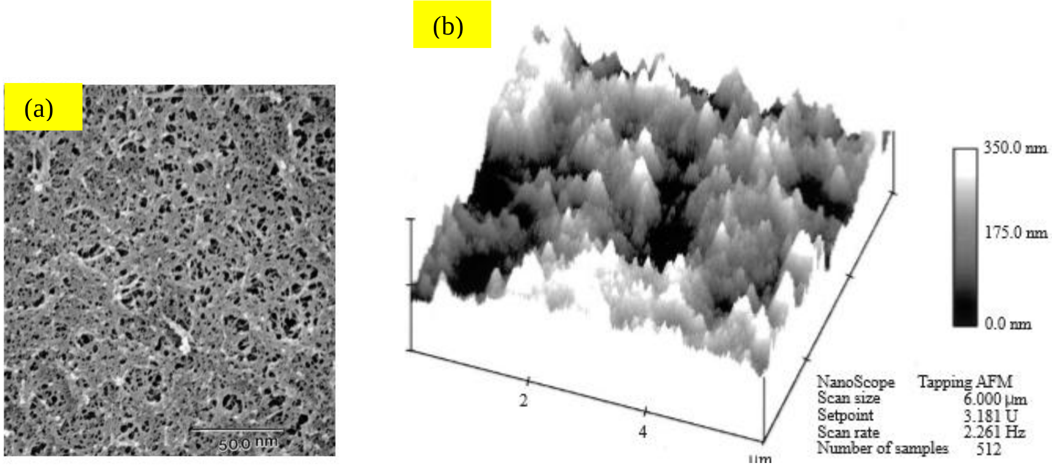

Figure 2-10: Corneal epithelial basement membrane (a) SEM micrograph; (b) AFM image. Reprinted with permission [71].

Micro- and nanoscale structures widely exist also in mineralized biomaterials, performing an essential role in setting up their outstanding properties [76]. The hierarchical assembly of enamel structure and functions, which are related to the unique characteristics of enamel has been studied. Human enamel was explored using electron microscopes. The observations revealed the complexity of the well organized enamel structures in terms of hierarchical assembly [76]. Based on the analysis, seven hierarchical levels of the microstructure were identified and described. To represent a complete spectrum of the organization covering a range from microscale to nanoscale, the scheme of seven levels was proposed: first, hydroxyapatite crystals (Level 1) form mineral nanofibrils (Level 2); the nanofibrils were aligned lengthways, aggregating into fibrils (Level 3) and further thicker fibres (Level 4); prism/interprism continua (Level 5) were then composed of them. Prisms were assembled into prism bands (Level 6) at the microscale, that provided various arrangements across the thickness of the enamel layer (Level 7). From the analysis of the enamel and bone hierarchical structure, similarities of scale distribution at each level were observed. Enamel has unique properties, including extraordinarily high hardness, excellent resistibility to wear, and stability over a lifetime of use. Thus, enamel structures and the biomineralization have been of interest to understand the basis for the enamel disease and to synthesize novel biomimic biomaterials. The TEM image of the crystals from human enamel has been used to identify the major components of the nanofibrils, and the basic structural units of human enamel which was hexagonal hydroxypatite crystals. The SEM micrographs showed the thin and long mineral nanofibrils with typical diameter of 30-40 nm. The long crystals within the microscopic domain run almost parallel to each other and the nanofibrils always aggregate lengthways with each other into thicker fibrils, 80–130 nm in diameter. SEM micrographs have also revealed the hierarchical structure of enamel which is formed by the combination of micro- and nanoscale structural units of fibrils and fibres. The AFM images showed that each prism is separated from the adjacent interpisms by the sheaths, which are relatively less eroded because of the higher content of organic materials. As a result, the keyhole pattern was found. The enlarged AFM image from the prism areas supported the presence of the fibres, consisting of some thinner fibrils, in the enamel surface. The fibres were also found in the interprism area. The average diameter of the fibres in the prisms and interprisms was 784.0±68.2 nm. The firbrils were closely connected in the fibre and further consisted of some nanofibrils [76].

Soft Lithoghraphy

To fabricate microfluidic devices traditional soft lithography, shown in Figure 2-11 is very commonly used and most of the devices are fabricated with polydimethylsiloxane (PDMS) which is a biocompatible polymer. First of all, a master is fabricated for the device, as shown in Figure 2-11(a). The Si wafer is cleaned with piranha solution (H_2O_2:H_2SO_4 = 1:3), rinsed with DI water and dried in nitrogen flow (Figure 2-11(b)). Next, this wafer is coated with photoresist, exposed in ultraviolet light using a mask and developed to define pattern in resist layer shown in Figure 2-11(c-e). Then the pattern is replicated in PDMS. PDMS is mixed at a specific ratio with curing agent. This mixture is degassed in desiccator for 1 h to get rid of air bubbles. PDMS is then poured on stamp (Figure 2-11 (f)) and heated to 150 °C for 10 min. The PDMS mold is then peeled off from the stamp and cleaned. For DEP or some other devices, electrodes are fabricated by depositing metal on the device to measure current. However, the PDMS mold is usually covered with glass slides after plasma treatment to complete the fabrication process shown in Figure 2-11(g). Microfluidic devices can also be fabricated directly in Si wafer using photolithography, etch, deposition and other fabrication techniques [77].

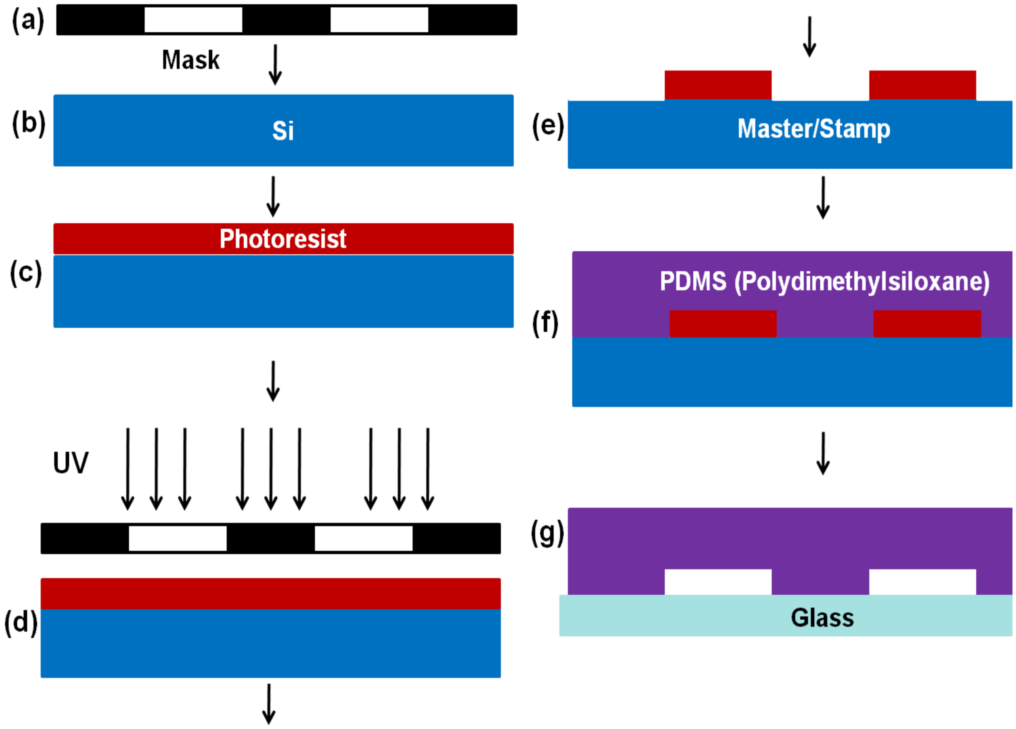

Figure 2-11: Microfluidic device fabrication steps using soft lithography technique.

PDMS

PDMS is the most widely used polymer, made of $SiOC_2H_6$ monomer, for microfluidic system. It is silicone-based organic polymer consisting of inorganic siloxane backbone and organic methyl groups attached to silicon. It has two parts, a liquid silicone elastomar and a curing agent. These chemicals are liquid at room temperature and have low glass transition temperatures. These two liquids are mixed together in certain ratio to form solid by cross linking. PDMS has several advantages such as: (i) its chemical stability is high; (ii) it has good thermal stability, and can be cured at different temperatures (from 20 °C to 180 °C); (iii) it is permeable to gas; (iv) it is optically transparent down to 280 nm wavelength of light; (v) durable and flexible; (vi) the interfacial properties can be modified by treating the surface with plasma or other chemicals; (vii) it is nontoxic and biocompatible; (viii) it can be sealed reversibly to itself and other materials via van der Waals forces, or it can be irreversibly sealed after plasma treatment by formation of covalent bonds. All these advantages make PDMS very attractive for microfluidic biosensors.

Microfluidic Systems

As mentioned earlier, conventional cancer cell sorting techniques are confined due to various limitations. Microfluidic systems have emerged as attractive platforms to detect cancer cells. Different microfluidic techniques are employed to recognize and enumerate CTCs. Magnetic beads based cell separation techniques, called magnetophoresis, have been shown to isolate and enumerate CTCs from blood samples with high efficiency, specificity and viability [16-21]. In order to take the advantage of both immunomagnetic assay and the microfluidic device, immunomagnetic CTC detection scheme has been reported [78-81]. Cancer cells have also been labeled with magnetic nanoparticles and separated from blood flow using arrays of magnets [78]. Dielectric properties of metastatic cancer cells are also known to be significantly different from normal blood cells and therefore DEP has been used to successfully detect CTCs with high efficiency and purity [82-90]. Numerous DEP techniques such as field flow fractionation DEP, multi-orifice flow fractionation DEP [87], contactless DEP [89] etc. have been reported. But complexity, time consumption, need for pre-processing and requirement of external magnetic or electric fields etc are limiting factors in these techniques [91].

Due to high specificity and selectivity, antibody and aptamers have been incorporated in several microfluidic setups to detect and enrich tumor cells [5, 15, 92, 93] and these ligand based cell detection techniques are known as cell-affinity micro-chromatography. However aptamers are not available for all types of cancers and their attachment to device is a long and tedious process. Therefore label-free microfluidic isolation of rare cells, that does not require multiple additional “tags” or “labels” is preferable [91]. Distinctive mechanophysical properties of CTCs such as density, adhesion, size, and deformability can be used for label-free separation. Usually sizes of tumor cells are not only larger than red blood cells (RBCs) and white blood cells (WBCs) but also have higher elasticity [94]. Some metastatic cancer cell types have been reported to be more than 70% softer than benign cells and mechanical analysis can distinguish these from normal cells of similar sizes and shapes [95]. Some devices like microcavity array [23], small capillaries [96, 97], 3D filters [24], pool-dam structures [98], and adhesion based nanostructured surfaces [99] use mechanical properties as discriminator of cancer cells from blood. On the other hand, some devices have employed numerous micro-channels or micropores, for example spiral channel [22], multiple channel segment devices [100], parylene membrane microdevice [25, 101] and herringbone-chip [26]. Microfluidic devices have also been reported for electrical and mechanical measurements of single cell to differentiate these [102].

Dielectrophoresis (DEP)

DEP is a phenomenon in which a force is exerted on a dielectric particle, suspended in a medium, due to a non-uniform electric field. The strength of the force depends on physical and electrical properties of the particles, medium, and frequency and amplitude of the applied electric field. The target particles which have greater electric permittivity than the suspension medium move towards the region of stronger electric field and this is called positive DEP. Negative DEP is just opposite to this where target particles move towards weaker electric field. DEP works on microparticles with diameter ranging from 1-1000 µm. DEP signatures vary among different biological cell types and also depend on the activation states of the cell. DEP is an effective approach of label-free isolation which has been studied widely in microfluidics. DEP-based cell separation techniques have been implemented to detect rare cells including oral cancer cells, colorectal cancer cells, prostate tumor-initiating cells, leukemic cells, breast cancer cells and so on [11]. At an optimized flow rate, DEP has high purity and recovery. Simple and traditional DEP technique has been reported in several studies to isolate cancer cells from blood [1, 11]. To overcome some limitations of DEP, such as bubble formation (due to electrolysis), electrode fouling and delamination, and expensive fabrication, contactless DEP (cDEP) was implemented to isolate tumor cells [103]. In cDEP, electric field is applied in the sample channel using electrodes which are inserted into two other microchannels separated from the sample channel by thin insulating barriers. However, to detect significant number of rare cells the minimum volume of sample required to be processed is high, usually 5-10 ml, which leads to low throughput. Hydrodynamic approaches have been combined with DEP to improve the throughput. Continuous flow based dielectrophoretic field-flow-fractionation (DEP-FFF) shown in Figure 2-12(a) has been reported to process large volume of blood sample in short period of time to isolate tumor cells [86, 88, 104]. One group has reported the processing of 10 ml of blood in less than an hour [104]. Here, peripheral blood mononuclear cells of a clinical specimen were slowly injected in a microfluidic chamber, deionized and CTCs were separated based on balance of DEP, sedimentation and hydrodynamic lift forces. Tumor cells were transported close to the floor of the chamber due to positive DEP force, while blood cells were accumulated to waste due to negative DEP force. The tumor cells were collected in outlet at an average recovery rate of ~75%.

Another scheme to improve the performance of DEP is multi-orifice flow fractionation (MOFF). This method can be used to move microparticle laterally due to hydrodynamic inertial forces created by a multiorifice structure [12]. In this method, microparticles can be concentrated at different lateral positions in a microchannel depending on their sizes. The reported device was composed of one inlet, a filter, a multi-orifice segment, a fraction segment and two wide outlets. The multi-orifice segment had an alternating series of contraction channels and expansion chambers repeated 80 times. This method had high throughput due to hydrodynamic separation and DEP separation provided precise post-processing to increase the efficiency. This system was able to isolate circulating tumor cells from blood at an efficiency of 76%.

Optically induced DEP (ODEP) is another method to produce tunable and dynamic electrode patterning in real time using a photoconductive layer [105]. Due to illumination of light, electron-hole pairs are generated in this layer, thus the electrical impedance is reduced significantly. Consequently, locally non-uniform electric field is created. This ODEP force can be used to manipulate microparticles. This technique has been implemented to separate CTCs from leukocytes based on their size and dielectric properties at an efficiency of 76-83%. Here, six moving light-bars, divided into two groups screening in opposite lateral directions, were used to define the separation region as shown in Figure 2-12(b).

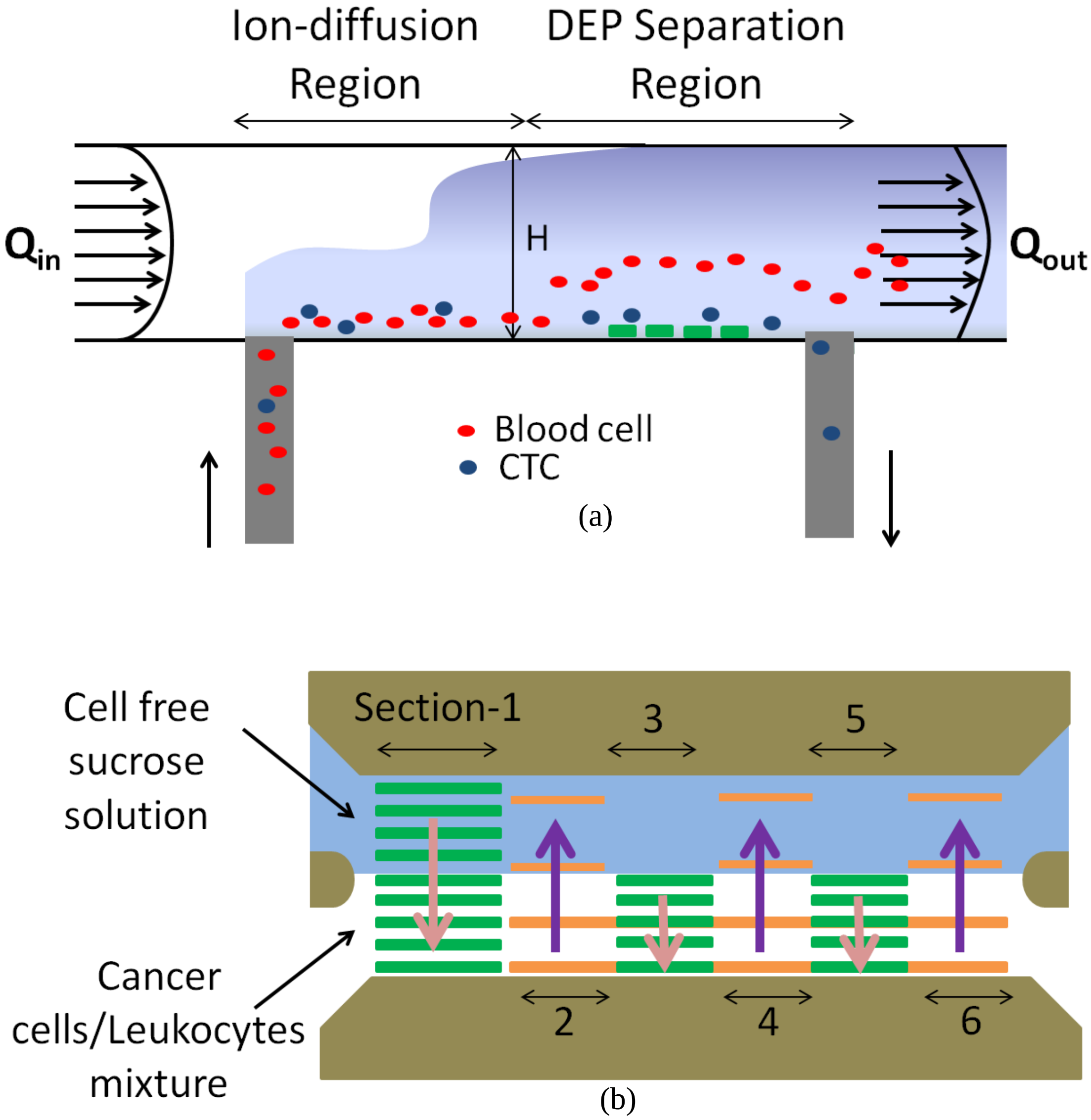

Figure 2-12: Schematic diagram of microfluidic devices to implement DEP techniques to detect cancer cells from blood sample, (a) a continuous-flow chamber for dielectrophoretic field-flow-fractionation (DEP-FFF) [104]; (b) optically induced-dielectrophoretic (ODEP) consisting of six sections of moving light bars [105].

Cell-Affinity Micro-Chromatography

Cell-affinity micro-chromatography is used to selectively capture specific target cells from heterogeneous cell population through selective binding with substrate-immobilized high-affinity ligands. This technique is widely used to separate cancer and healthy cells [1]. The large surface to volume ratio of microfluidic channels enhances the probability of cell-to-surface interactions and results in better isolation performance. Implementation of 'optimum shear stress' is necessary to balance between separation efficiency and purity. The first antibody-based cell-affinity micro-chromatography system was reported to capture cervical cancer cells by specific capture ligands (α6-integrins) in a PDMS microchannel [106]. In microchannels, cells prone to follow the streamline due to dominant laminar flow that prevents effective interactions between cell and surface. Thus, modification of the surface of microchannels to enhance cell-surface interactions has been key interests for many studies. Nagrath et al. fabricated functionalized micro-pillars, shown in Figure 2-13(a) to increase the cell-antibody interactions to separate CTCs with high purity and efficiency. They detected cancer from 115 out of 116 patient samples [5]. The ‘‘herringbone chip” is a second generation CTC chip implemented with a microchannel architecture to produce microvortices within the flow to improve the likelihood of cell–surface interactions and it achieved a high cell recovery rate (91.8%±5.2%) for prostate cancer cells [26]. This device also successfully detected CTCs from 14 out of 15 patients. An alternative strategy to improve cell-surface interactions is nanotextured surfaces. Nanostructured surface coated with anti-EpCAM resulted in a higher cancer cell recovery rate because of topographic interactions between silicon nano-pillar and nanoscale proteins found on cell surface [107]. Densely packed nano-pillar surfaces enabled the capture of cancer cells of up to ten times compared to channels with flat surface. The recovery rate was 95% for tumor cells from whole blood. This device was able to detect cancer from 17 out of 26 patients with prostate cancer [108]. More detail about nanotextured surfaces will be explained in later sections.

Due to limited available antibodies to capture target cells, aptamers have recently been employed as binding ligands to detect CTCs in microfluidic platform. Aptamers have higher selectivity and sensitivity compare to antibody. Aptamers are also more stable at various physical conditions. Phillips et al. used aptamers in microfluidic devices for the first time to enrich cancer cells by immobilizing aptamers on the surface of flat microchannels [53]. The recovery rate of the system was 80% with purity of 97.52%. A second-generation device was implemented (Figure 2-13(b)) to detect multiple types of cancer cells simultaneously from a single mcirofluidic channel device functionalized with aptamers [15]. DNA-aptamers showed 135-fold enrichment of rare cells. The height of the channel was on the order of a cell diameter to achieve that high yield. Aptamer functionalized graphene oxide nanosheets have also been implemented to isolate CTCs [109]. Flower-shaped gold patterns were first depostid on Si wafer. Then graphene oxide was adsorbed onto the gold surface and coated with anti-EpCAM to isolate cancer cells at an efficiency of 82%. Immobilized long chain DNA molecules (10–100 micrometers) was introduced in a herringbone structured microfluidic device to isolate cancer cells shown in Figure 2-13(c) [110]. The DNA molecules contained particular aptamer sequences repeatedly to recognize target cells. The long-chain DNA molecules were extended into the flow and enhanced the accessibility of aptamer to cells. The capture efficiency in this device was 80%.

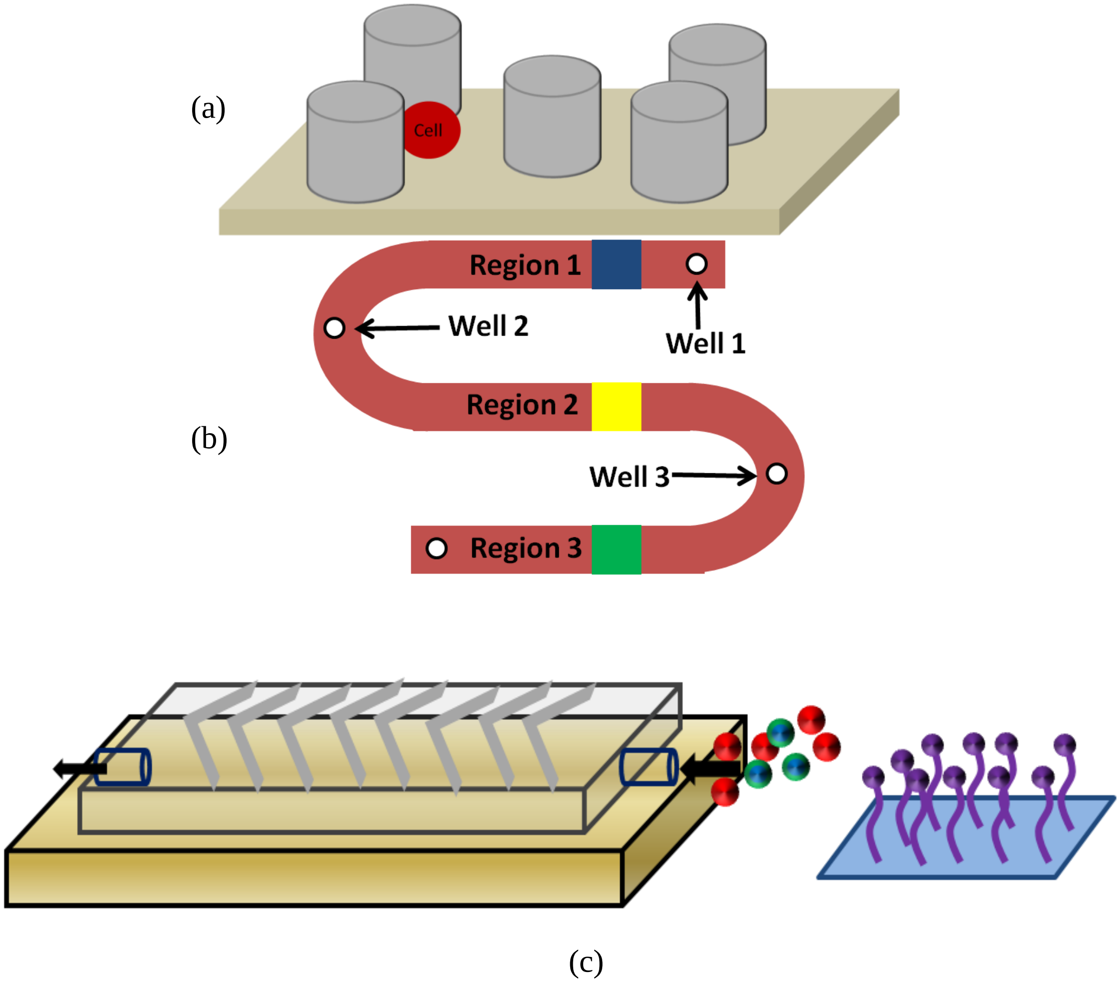

Figure 2-13: Schematic diagram of microfluidic devices to implement cell-affinity micro-chromatography, (a) antibody coated micropost device [5]; (b) multi-well device to detect three types of cancer cells simultaneously using aptamer [53]; (c) long and multivalent DNA aptamer functionalized herringbone chip [26].

Magnetophoresis

This approach implements a magnetic field gradient to selectively isolate target cells labeled with magnetic particles. Compared to the passive hydrodynamic approaches, this technique actively applies strong magnetic force to extract magnetic particle-labeled cells. Thus, this system is less dependent on the condition of flow and particle-particle interactions. Consequently, this method has higher specificity and allows to process whole blood in a high-throughput manner [11]. This approach is also biocompatible with low damage to the cells. Though the high-gradient magnetic field is used, the forces are not directly applied to the cells and thus 100% viability can be obtained in this method. First, Liu and Pang et al. implemented the microfluidic device for isolating rare cancer cells from red blood cells (RBCs) suspension using magnetic cell separation [111]. Hexagonal array of nickel micro-pillars was integrated onto the bottom of a microfluidic channel to generate magnetic field gradient to trap super paramagnetic beads. These beads were functionalized with specific antibodies. The cell capture efficiency was 62-74% in this system. Lateral magnetophoresis is a common method for cell separation among immunomagnetic approaches. A horizontal magnetic field was used to drag labeled target cells from sample flow into the buffer flow, as shown in Figure 2-14(a) [80]. This technique was robust and provided high throughput and recovery rate. This technique was reported to isolate CTCs from human peripheral blood with 90% recovery and 97% purity. This method required buffer flow and therefore vertical magnetic field gradient was introduced to isolate rare cells which could be used for high capture efficiency [79, 81]. A magnetic porous structure has been reported which had passage for cellular samples but generated high magnetic forces to capture the labeled cells [77]. This magnetic separation device was called magnetic sifter, shown in Figure 2-14(b), which is basically a miniature microfluidic chip with high density of pores. This device offered high capture efficiency (~95%) of tumor cells from blood at high throughput. The release of captured cells was around 92% in this technique.

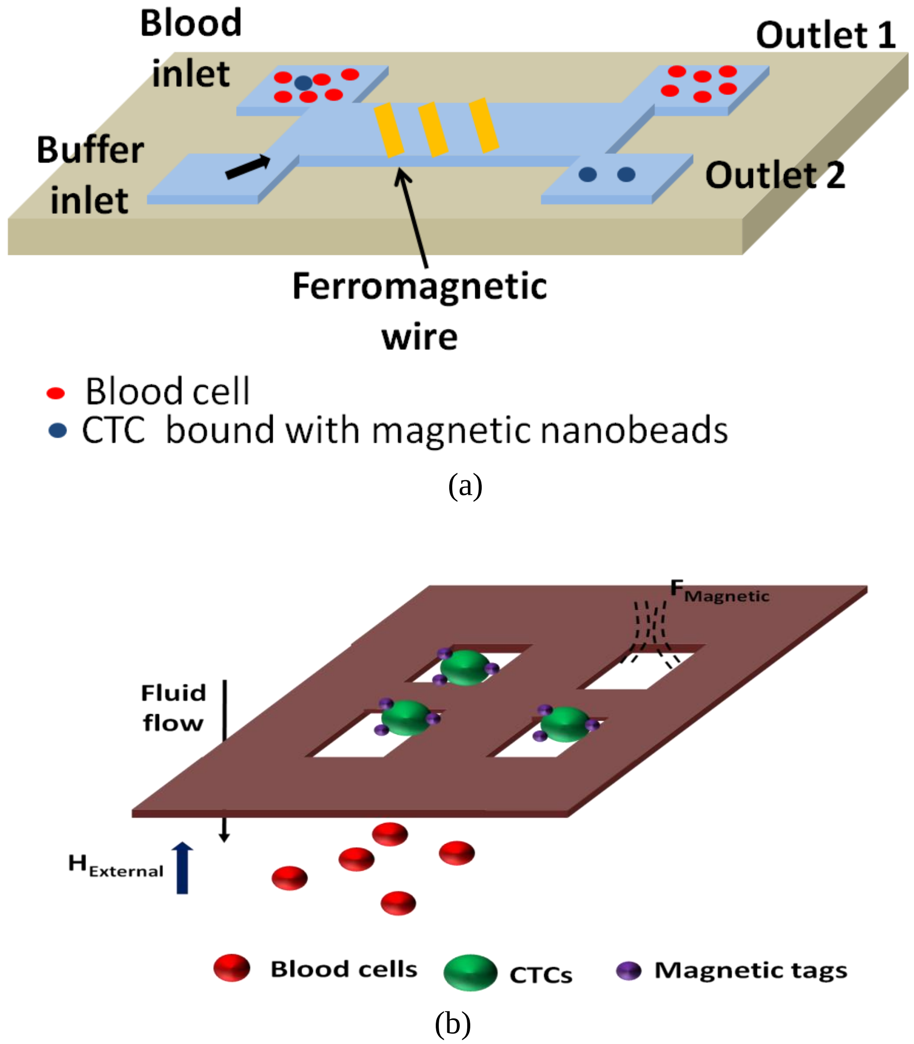

Figure 2-14: Schematic diagram of magnetophoretic microdevice, (a) isolation of CTCs based on magnetophoretic signature [80]; (b) capture principle of a magnetic sifter [77].

The most obvious limitation of magnetic bead based techniques is the requirement of additional sample preparation steps to label the target cells. To address this issue a novel method was introduced called 'Ephesia' [17]. In this study, antibody-conjugated magnetic beads were assembled dynamically into an array inside microfluidic channel. Micromagnetic pattern was generated onto glass using magnetic ink dots. Using external uniform magnetic field they concentrated field lines and created local gradient that worked as potential wells for the magnetic beads in the device. When the sample was flown through the channel, target cells with specific biomarkers were captured by the magnetic beads. The superiority of this method was dynamic assembly of the magnetic microbeads. The cell capture efficiency of this device was 94% for cancer cell lines.

Mechanophysical Properties

Differences in mechanophysical properties of cells can be exploited in microfluidics for the detection of cancer cells without having the knowledge of biochemical characteristics of target cells. Size, deformability and density of cancer cells are significantly different from blood cells. The flow rate, sample concentration, and device geometry are key factors for this method. After optimizing the conditions for a specific cellular sample, the protocol could be validated for numerous clinical applications. Mechanophysical property based cell sorting has several advantages [11]. First of all, this approach is label free, does not require any immunostaining, antibody labeling or expensive chemical reagents. Thus it reduces the sample preparation time and risk of cell damage. Proper design of separation scheme can handle large amount of samples in a short time. These separation methods are also highly reproducible. First size-based microfluidic cancer cell separation device consisted of four regions with decreasing channel widths and depth [100]. It was observed that cultured neuroblastoma cells were retained in 10 µm wide and 20 µm deep channels. On the other hand, adult white blood cells were retained in 2.5 µm wide and 5 µm deep channels, while red blood cells were able to pass even through these small channels. Size dependent parylene membrane filters has been reported for cancer cell detection and separation [112]. This micro-filter device had circular pores of diameter 10 µm. The size difference between CTCs and blood cells was exploited to test sample of metastatic prostate, breast, colon, and bladder cancer patients. Out of 57 patients, this device was able to detect CTCs from 51 samples. The cell viability was low here due to high stresses developed in the cell membrane during the cell capture process. A double membrane device was developed to decrease the stress on cell membrane shown in Figure 2-15(a) [24]. A second porous membrane was introduced below the first membrane. Pore position between two membranes was intentionally misaligned. The bottom membrane supported the trapped cells to reduce flow-induced stress on cell membrane. The viability was reported to be 85% for this device. Multiple arrays of crescent-shaped wells were fabricated in a device to isolate breast and colon cancer cells at an efficiency of 80% from whole blood [96]. 5 µm gaps were used within each of the crescent-shaped traps to capture CTCs while blood cells were passed through. Hydrodynamic micro-filter based on cell size variations has been reported to separate cancer cells from blood [113]. Laminar vortices combined with inertial focusing selectively isolated and trapped larger cancer cells through an array of expansion-contraction reservoirs placed in series and parallel. A shear gradient lift force tried to push the cells towards the channel walls whereas the lift force repelled the particles away from the wall. For larger cells, shear gradient lift force was higher and pushed toward the vortex core where they remained isolated and orbited in the vortex. The reported cell recovery rate was lower, 23% for breast cancer cells. Clogging and saturation are main drawbacks of the filtration methods. Ratchet mechanism shown in Figure 2-15(b) has been employed to solve this problem [114]. No clogging and degradation of the device was observed in this device for more than 4 hours.

Deterministic lateral displacement (DLD) technique allows the label free cell isolation where fluid passes through an array of microposts. Smaller particles followed the periodic streamline patterns and pass the posts but larger particles bump against posts and displace laterally in opposite direction to the small particles. Therefore, particles can be differentiated based on their size, shape and deformability [25, 100, 101, 115]. Loutherback et al. optimized DLD array to isolate spiked cancer cells from blood with efficiency greater than 85% at a flow rate of around 10 ml/min [115]. They isolated different types of cells and the result indicated that the larger cells had higher isolation efficiency, since their flow profiles fit more into the displacement zone of the DLD arrays.

Rare cells can be separated based on inertial lift force which depends on the velocity of the particles in a microfluidic channel. As the magnitude of the lift force is determined by the particle size, special designs can allow separating cells based on their size and deformability. A spiral microchannel with inherent centrifugal forces has been implemented for continuous, size-based separation of CTCs from blood [116]. Device performance was optimized for 85% efficiency at a throughput of 3 ml/h. Recovery of cancer cells using cancer cell lines and clinical validation was performed with positive CTC enumeration in all samples from patients with metastatic lung cancer. A spiral microfluidic channel with trapezoidal cross-section has been reported for ultra-fast, label-free enrichment of CTCs from clinically relevant blood volumes [117]. This novel design allowed very high throughput and appreciable CTC capture efficiency. This device was able to detect CTCs from 100% of the patient sample. To take the study of spiral channel one step further, a group has reported double spiral microfluidic platform for high throughput and capture efficiency [118]. In a curved microfluidic channel, a Dean drag force is induced on particles to compete with the inertial lift force, resulting in different equilibrium positions for particles of different sizes. Based on this hydrodynamic principle, this device was able to isolate tumor cells spiked in blood. Results indicated that 92.28% blood cells and 96.77% tumor cells were collected at the inner and middle outlets, respectively. Microfluidic devices are capable of measuring cellular biophysical properties to detect cancer cells. A microfluidic device has been reported for electrical and mechanical measurement of single cells, shown in Figure 2-15(c), which detected CTCs [102]. Here cells were aspired continuously through a constriction channel. Elongation of the cell and impedance profile of the channel was measured simultaneously. The cell transit time through the channel and the impedance amplitude ratio was calculated to distinguish different types of cells at an efficiency of 93.7%. Microfluidic devices provide a number of advantages for isolating and analyzing cancer cells, but the throughput is still an issue. Most of the existing microfluidic devices need several hours to process a standard 7.5 ml blood sample. In general, microfiltration may provide high throughput but high flow rate and large gradients in shear stress may damage the isolated cells. Thus, for enumeration of cancer cells microfiltration is very suitable where subsequent analysis steps are not required. For gentle capturing, methods such as micro-affinity cell-chromatography, dielectrophoresis and magnetophoresis are better alternatives.

But more work needs to be done using clinical samples based on these concepts. Inertial microfluidics can also be exploited for both label-free and high throughput cell isolation process. A gentle and high throughput isolation system may emerge with the possibility for continuous sorting and isolation. Thus, blood sample may be removed from the body to isolate cancer cells and then re-injected to the body. As captured cells may have variety of subtypes or the same cell type at different stages of growth, subsequent analysis to characterize genotype and phenotype can allow profiling of the isolated cells. To serve this purpose, cells must be captured in viable condition with high cell integrity.

Isolation Based on Immunochemical Signature through Surface Interactions

Interactions between surface and cells have been explored as a successful modality for isolation of rare tumor cells [11]. Large surface to volume ratio of microfluidic devices remarkably enhances the probability of cell-to-surface interactions for better cell isolation efficiency. Immobilization of immunoaffinity-binding molecules or application of specific surface pattern can be used to differentiate adhesion among cells. Optimization of shear stress is very important to obtain high purity and efficiency. Generally, higher shear stress provides less efficiency but better purity and vice versa. For rare cells, isolation efficiency gets higher priority than purity. Throughput is another key concern which needs to be high as much as possible while obtaining appreciable efficiency. In such case, laminar flow reduces the probability of cell-surface interactions and therefore nanostructures have been introduced.

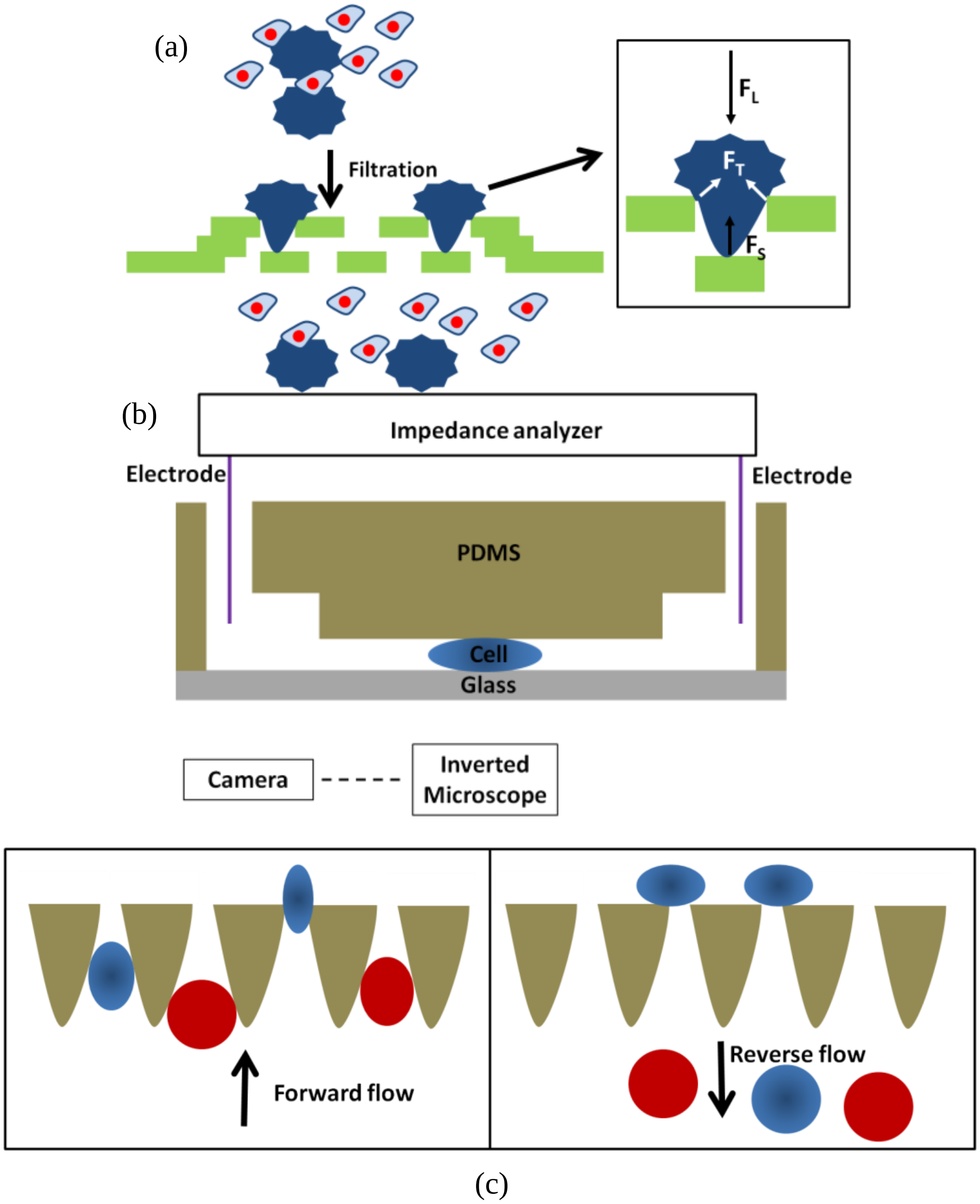

Figure 2-15: Microfluidic devices for the isolation of CTCs based on their mehcanophysical properties, (a) filtration using a 3D microfilter device and the applied forces (F_L) on a trapped cell [24]; (b) ratchet mechanism for cell-sorting [114]; (c) electrical and mechanical measurement of CTCs in a constriction channel [102].

Several studies have demonstrated that cell capture, cell growth, adhesion and orientation are influenced by nanoscale topography of the surface [13, 119, 120]. The key feature of nanotextured surface is, it offers increased effective surface area to capture high quantity of probe molecules [13]. Consequently, nanostructured substrates have emerged as promising biosensing platforms since they provide better isolation sensitivity for CTC isolation.

Nanostructured substrates can be fabricated using various methods which can be primarily divided in two categories, top-down and bottom-up method [120]. In top-down fabrication methods, a bulk material is patterned by a series of steps. First of all, lithography is used to transfer pattern from a mask onto a substrate. Light, X-ray or electron beam is mostly used in lithography process to make pattern of controllable geometries. There is another form of lithography named colloidal lithography in which geometries depend on random dispersal of coated nanoparticles [121, 122]. Secondly, nano-embossing is a fascinating method for inexpensive and high throughput nanofabrication [123]. Thirdly, etching is a subtractive method to selectively remove material from the substrate. Nanostructured surfaces can be prepared by etching silicon wafer [124] and polymers like PDMS, PLGA, poly-L-lactic acid (PLLA), polyethylene terephthalate (PET), and polyether urethane (PU) [125].

In the bottom-up methods, desired structures are fabricated by bringing the building blocks in close proximity. This approach has already been implemented in numerous biotechnology applications such as in tissue engineering using self assembly [126], magnetic [127] and acoustic assembly [128], and bioprinting [129]. One of the bottom-up methods is electrospinning which utilizes electrical forces to synthesize nanofibers using polymers. These nanofibers are arranged in order or randomly on a substrate to form nanostructure surfaces [130]. Next, chemical vapor deposition (CVD) is also used for nanoscale fabrication especially silicon nanowires (SiNWs) can be fabricated using CVD. In this process, materials react and/or decompose on the substrate to produce desired deposition on surface [131, 132]. Vapor-phase coating is another fabrication method to deposit nanoporous film on substrate [133]. The average diameter of nanopores can range from 100 to 500 nm. Gas foaming technique uses gas as porogen and produces sponge like structure of 0.1-100 nm [134]. Thermally induced phase separation technique is similar to gas foaming but it utilizes a solvent with a low melting point that can be used to remove certain chemicals and leave random nanotextured pattern of few nanometers on the substrates [135]. These fabrication processes with their advantage and limitations are summarized in Table 2-5.

Nanostructured Substrates for CTC Isolation

Recently, nanostructured surfaces have been studied extensively for cell proliferation, migration, differentiation and alignment on nanostructured surfaces [136-138]. Nanotexturing facilitates protein adherence to surface due to its larger surface area. Also protein epitopes are recognized by integrin heterodimers on the cell membrane; integrins assemble as focal points which initiate cell adhesion [120]. Consequently, the nanostructure itself facilitates cell attachment. Adhesion forces between cells and substrate are significantly improved by antigen-ligand binding. A number of nanostructured substrates have been explored for rare cell isolation including nanopilars, nanowires and nanotextured PDMS. Figure 2-16 shows nanostructured surfaces fabricated using various methods [17].

Table 2-5: Nanostructure preparation techniques and their minimum feature size [120].

Fabrication method	Minimum feature size	Advantages/limitations
Optical lithography	~50 nm	Patterns can be created precisely
X-ray lithography	~20 nm	Expensive lenses needed
E-beam lithography	5-10 nm	Good contol on geometries. But serial and time consuming process.
Colloidal lithography	~300 nm	Geometries are random.
Nano-embossing	~100 nm	Geometries and patterns are controllable.
Etching polymer	>1 nm	Inexpensive method but nanostructures are random.
Etching silicon wafer	2-3 nm	Aluminium template is required to have control on dimensions and pore sizes.
Reactive ion etching	20-100 nm	High aspect ratio patterns.
Electrospinning	40-2000 nm	More than 20 polymers can be used; limited to only fiber formation.

Table 2-5- *Continued*

Chemical vapor deposition	~2 nm	Layer thickness can be controlled. But require high vacuum furnaces and it is slow process especially in the case of epitaxy.
Vapor-phase coating	100-500 nm	Fabrication method is easy but the coatings are not very stable.
Gas foaming	0.1-100 nm	Low-cost method but have limited applications.
Phase separation	>1 nm	Nanofeatures and pore sizes cannot be controlled precisely.

Nanopillars and Nanowires

Array of micro/nano scaled silicon pillars have been used for studying cell adhesion, migration, and morphology [139]. The surface area depends on number of nanopillars or nanowires per unit area and their average diameters. The adhesive force can be increased by increasing the number of nanostructures in per unit area or by decreasing their diameters [139-141]. However silicon nanopillars (SiNP) with diameters in the range of 100-200 nm on silicon wafer have been used for cancer cell isolation. The capture yield of MCF7 cells in culture medium was 45-65% on SiNP which was 10 times more than that was found on flat silicon. Viability of the captured cells was 84-91% [142, 143]. SiNPs were also integrated into a microfluidic device with chaotic micromixers to enhance cell-SiNP contact by making a vortex with a serpentine chaotic mixing channel [144]. Again silicon nanowires (SiNWs) of 100-200 nm in size were reported for T lymphocyte separation with capture efficiency of 88% [145]. SiNWs covered with uniform gold nanoclusters (Au NCs) were also synthesized (diameter: 50-160 nm) to capture MCF7 cancer cells with an efficiency of 88% and viability of 95% [118]. In another report, quartz nanowires (QNWs) were fabricated to capture A549 cells with average efficiency of 89% compared to 23% achieved on flat glass surfaces [146]. The size of nanowires was in the range of 80-100 nm. Recently, bare nonorough glass surfaces with root-mean-square (*Rq*) value of 150 nm were utilized to capture 93.3% MCF7 and 95.4% MDA-MB231 cells spiked into 500 µl lysed blood, regardless of their EpCAM expression [147]. On the other hand, only 22% MCF7 and 13.9% MDA-MB231 cells were captured on smooth glass surfaces. In this experiment, surfaces were not functionalized with any ligands and it was demonstrated that only nanoroughness of glass could significantly enhance adhesion of cancer cells to the surfaces. High nonspecific binding was also observed when mixing ratio of MDA-MB231 and PBMCs was changed from 1:1 to 1:200, effectively capture purity of MDA-MB231 cells got significantly reduced from 84% to 14% [147].

Nanotextured PDMS

Nanotextured substrates are getting much attention for cancer cell enrichment [120]. The basement membrane can anchor cancer cells through cell adhesion molecules to improve cell adhesion and growth [148]. Aptamer funcionalized nanotextured PDMS substrates have been fabricated to isolate cancer cell. NaOH etched poly(lactic-co-glycolic acid) (PLGA) polymer scaffold was used as a master for nanotextured PDMS substrate. The available large surface area allowed immobilizing large number of aptamer which favored cell isolation. Consequently, total number of captured hGBM cells on nanotextured PDMS were twice that of on a glass surface [13].

Surface Coating with Nanomaterials

Nanostructured surfaces can be fabricated by coating nanomaterials on flat surfaces [120]. Nanoscale surface coating enhanced capture efficiency of KG1a cells [149, 150]. Rolling velocity of cells on a silica coated microtube surface was decreased by 50% and as a result number of cells captured on the nanoscale surface was twice than planar surface [150]. Similar results were reported for Titanium (IV) Butoxide and halloysite nanotubes [149, 150]. Another report has shown that glass surface with a layer of indium tin oxide was homogeneously coated with anti-EpCAM grafted poly(3,4-ethylenedioxy)thiophenes polymer (PEDOT). The diameters of coated dots ranging from 98 nm to 333 nm to isolate cancer cells [151]. Capture efficiency of MCF7 (EpCAM+) cells were related to polymer dot size and for feature size of 232 nm it was 4-5 times higher than that on a flat surface. It was also reported that capture efficiency of EpCAM+ cells was 10 times higher than the capture efficiency of EpCAM− (negative) cells (HeLa). Again, surface nanotopography of glass slides was controlled over a large range (100-1150 nm) by coating with silica beads to study Jurkat cell capture [152]. Antibody modified silica beads coated surface showed 1.2-1.6 times higher cell capture efficiency compared to flat surface. Silicon wafer was coated with TiO_2 nanofibers (100-300 nm in size) by electrospinning and antibody immobilization was employed to achieve over 80% cell capture efficiency for HCT116 cells. This higher efficiency was achieved in culture medium and it decreased to 45% when cells were spiked into human blood samples [153].

Nanostructured surfaces increase cell isolation efficiency because of several features [120]. First of all, it allows higher surface area for biomolecule immobilization. Next, it facilitates lower rolling velocity and enhances cell attachment. Nanostructure might assist in cell attachment by improving cell-substrate adhesion. Moreover, pseudopodia formation might also help to increase cell capture yield. The morphology of captured cells was found to be flatter on nanostructed substrates compare to flat substrates [13].

Despite all these promising results from nanostructured substrates, none of these have shown clinical validity or utility and mostly remain in laboratory settings. There are two major challenges in CTC isolation technology [120]. First of all, heterogeneity of CTC is primary issue. CTCs can even differ between two cancer patients. In brief, they might have variable expression of biomarkers on cell membranes. The other important issue is releasing captured CTCs from the nanostructured substrates. The strong adhesion forces between the captured cells and functionalized substrates are needed to be overcome to detach cells. Some methods are implemented to satisfy this purposes such as physical elution with fluidic flow, thermodynamic release, electrochemical desorption, proteolytic enzyme degradation,

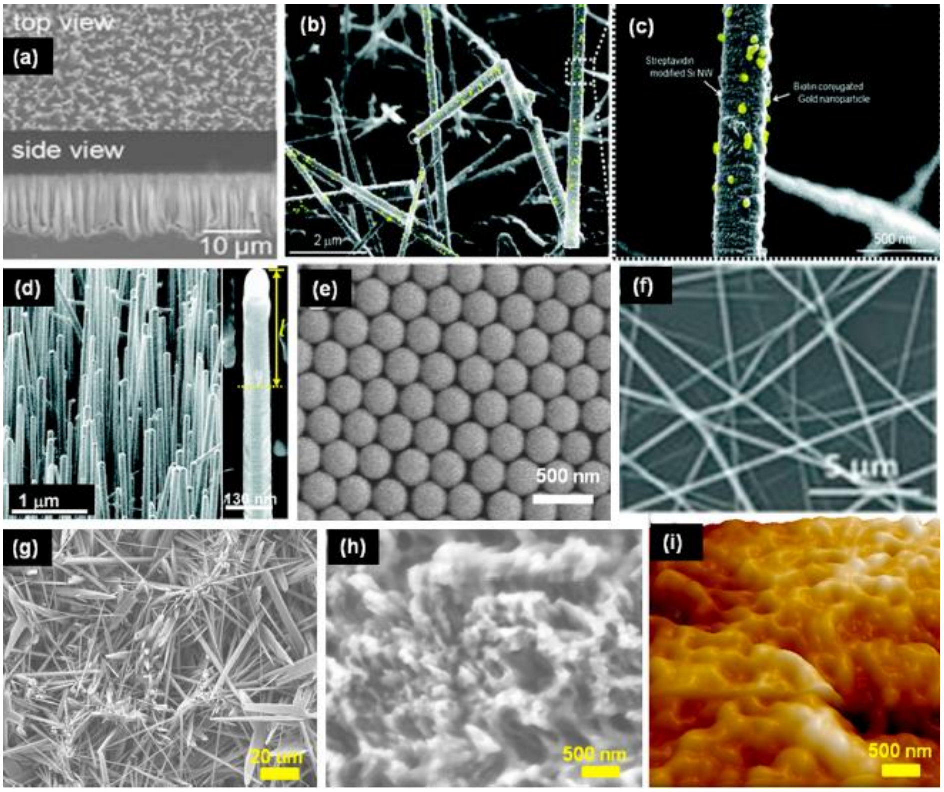

Figure 2-16: Nanostructured substrates fabricated by different processes. SEM images of (a) silicon nanopillars produced by we chemical etching; (b) silicon nanowires (SiNWs) produced by vapor—liquid—solid method; (c) Magnified image of (SiNWs) bound to biotin-gold nanoparticles; (d) Au nanoclusters coated SiNWs prepared by rapid thermal chemical vapor deposition; (e) silica nanobeads deposited on glass[152]; (f) TiO_2 nanofibers fabricated using electrospinning and calcinations[153]; (g, h) micro needles and nanotextured surfaces were synthesized by chemical etching of chicken eggshell[119]; (i) AFM image of nanotextured PDMS surface cured on chicken eggshell. Reprinted with permission. Reprinted with permission [121].

endonuclease clearance, oligonucleotide hybridization, removable glass beads array, and negative selection strategy [14, 154, 155]. However all these methods have certain limitations and thorough studies are needed to overcome these issues and bring nanostructured surfaces to clinical applications.

Chapter 3

LABEL-FREE ISOLATION OF METASTATIC TUMOR CELLS USING FILTER BASED MICROFLUIDIC DEVICE

Introduction

Microfluidic devices have been employed for the detection of tumor cells [1, 9, 11]. Here we introduced a microfluidic filter type device that captured cancer cells in spite of their highly elastic nature [94]. The device had one inlet and outlet connected by 400 microchannels shown in Figure 3-1. The dimensions of the microchannels were optimized to isolate more than 78% of renal cancer cells in the inlet. This label-free, cost-effective, and high-throughput technique could be implemented for rapid cell sorting based on their distinctive physical properties such as size and deformability without any pre-processing. This device was fabricated in PDMS using soft lithography with different cross-sectional areas of the channels by varying the width and height. The four types of devices with channel dimensions of 20 µm x 10 µm (Device-1), 10 µm x 10 µm (Device-2), 10 µm x 5 µm (Device-3), and 5 µm x 5 µm (Device-4) were fabricated. For every device, dimension is represented as height x width. Cell blocking efficiency of these four devices for metastatic renal cancer cells were 31.04%, 45.18%, 70.96% and 78.36% respectively [156]. The smaller cross-sectional area increased the overall cell isolation efficiency showing specific behavior of RBCs and WBCs in these devices. From our experiments it was observed that RBCs and WBCs were small enough to pass easily through the microchannels in Device-3 and Device-4. Eventually cancer cells were mixed with rat blood at low concentration and Device-4 was able to detect tumor cells successfully with substantial efficiency.

Experimental Section

All the chemicals were purchased from Sigma-Aldrich (St. Louis, MO) unless mentioned otherwise.

Microdevice Design and Fabrication

Dimensions of the microchannels were chosen based on cell size. As diameter of cancer cells mostly varied from 10-20 µm, therefore experiments were started with dimension of 10 x 20 μm^2. Several articles have also suggested similar dimensions of channels to capture cancer cells [27-37]. It was reported that WBCs and RBCs could traverse through 2-5 µm capillaries while cancer cells were captured [28]. Again, simple mechanophysical analysis was performed using Young's law. It was calculated that for a specific flow rate of 1 mL/h, the final size of CTCs in a channel of dimension 10 x 20 μm^2 could be reduced to 9.99 µm and 19.99 µm for their initial diameter of 10 µm and 20 µm respectively. The Young's law described a relationship among Young's modulus (*Y*), applied pressure (*P*), initial length (*L*) and change of length (*l*) of a substance by the following equation,

$$Y = P/(l/L) \dots \dots \dots \text{(3-1)}$$

Here the value of Young's modulus for cancer cells was assumed as 0.5 kPa [26]. From the above analysis it was expected to capture a good number of tumor cells using this device. But obtained capture efficiency for the device was low. Thus the dimensions of the channels were decreased to enhance efficiency.

The microdevice had one inlet and outlet connected via microchannels for blocking tumor cells. Dimensions of the inlet and outlet were 28 mm by 7 mm. The width of the microchannels was varied from 5 to 10 µm. This device was fabricated in

PDMS by soft lithography. First of all, the photo-masks were drawn in AutoCAD and patterns produced on glass. The inlet and outlet were fabricated by spin coating (1000 rpm, 30 s) SU-8 2010 on a silicon wafer. The height of the inlet and outlet was 22 µm. Next, the microchannels were fabricated using 10 µm height SU-8 2010 (spin coated at 1000 rpm for 30 s) and 5 µm height using SU-8 5 (spin coated at 3000 rpm for 30 s). The patterns were generated in masters using photolithography.

Next, the patterns were translated to PDMS. First of all, PDMS was mixed (10:1, wt/wt) with Sylgard 184 silicone elastomer curing agent (Dow Corning). This mixture was degassed in a desiccator for 1 h to get rid of the bubbles. Then PDMS was poured on the masters and heated at 75 °C for 5 min and then 150 °C for 10 min. Next the PDMS molds were peeled off from the masters and fluidic ports were punched in every PDMS mold. These molds were cleaned in isopropyl alcohol (IPA), rinsed in deionized water (DI water) and dried in nitrogen. To cover PDMS, glass slides were used. The glass slides (50 mm x 75 mm) were cleaned with piranha solution (H_2O_2:H_2SO_4 in a 1:3 ratio) for 10 min, rinsed with DI water and dried in nitrogen flow. The PDMS and glass slides were treated with UV Ozone plasma for 25 min and hermetically bonded together. Eventually the devices were filled with 1X PBS with 5 mM magnesium chloride (pH 7.5) to make it hydrophilic.

Cell Culture

Metastatic renal tumor cells were isolated from the brain tissues of consenting patient at the University of Texas Southwestern Medical Center at Dallas, Texas, USA as per the approved Institutional Review Board protocol [38]. The known metastasized renal derived cancer cells were collected in ice-cold Hank’s medium. Then cells were chemically dissociated with papain and dispase (both 2%) as reported earlier [39]. Next cells were cultured in Dulbecco's modified Eagle's medium (DMEM) with 10% fetal bovine serum [156]. The renal cancer cells were stably transduced with a lentivirus expressing *mcherry* fluorescent protein. The blood samples were collected from tail of a rat by restraining the animal. The blood was collected in tubes with K2-EDTA as anticoagulant.

Experimental Setup and Procedure

The renal cancer cells were suspended in 1X PBS solution to get desired concentration. The cells were flown through the microfluidic channel device at flow rate of 1 mL/hr using a syringe pump shown in Figure 3-1. Although, higher flow rates would have reduced the processing time, the larger shear forces on the cells would have modified the cell behavior and selective filtration capability would have been lost. At the same time cell viability will be reduced at higher shear stress. Cells were passed for 30 min. To avoid cell sedimentation the syringe was shaken after every 10 min. After passing the cells, whole devices were scanned thoroughly and images were taken using optical microscope to count the cells in inlet and outlet. In addition the cell solution that was coming out from the outlet chamber was collected using syringe and also images were taken of that solution to count the number of cells in the outlet. All of these images were analyzed to determine cell capture efficiency and also cell sizes were measured using *ImageJ*. In order to calculate cell capture efficiency, average number of cells passed to the outlet chamber and average number of cells captured in inlet chamber in per unit area was considered.

The cell viability was measured using the solution that was collected from outlet chamber. This solution was mixed with equal volume of trypan blue solution (0.4%) and let sit for 5 min at room temperature. This solution was put on a glass slide and observed in optical microscope to count live and dead cells.

The blood samples were passed through devices after diluting with sterile 1X PBS at 1:10 ratio in order to reduce the sample viscosity [6]. Next, the blood was diluted similarly and cancer cells were mixed in it at a concentration of 1000 cells/mL and this solution was used to run experiment in Device-4. After running experiments with this cell mixture the devices were observed in fluorescence microscope and images of the devices were taken in order to calculate cell capture efficiency of the device to isolate cancer cells from blood using the same procedure mentioned above. In order to increase throughput several devices can be used in parallel. Besides number of channels can be increased in each device, which could have allowed higher flow rate.

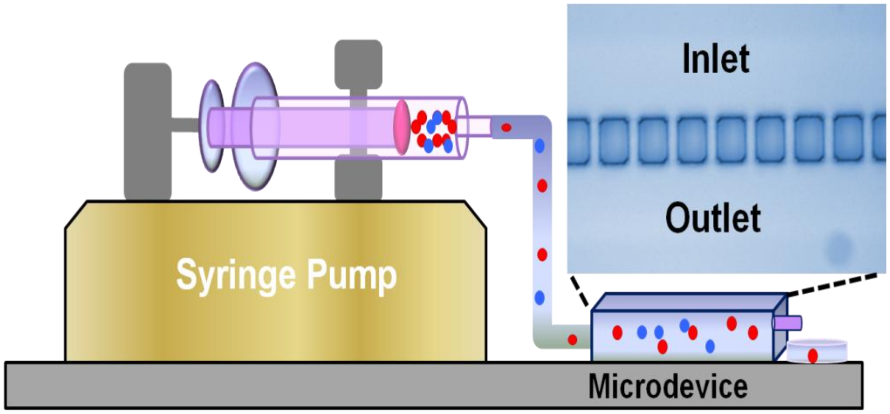

Figure 3-1: Schematic diagram of the experimental setup and microfluidic channel device [156].

Results and Discussion

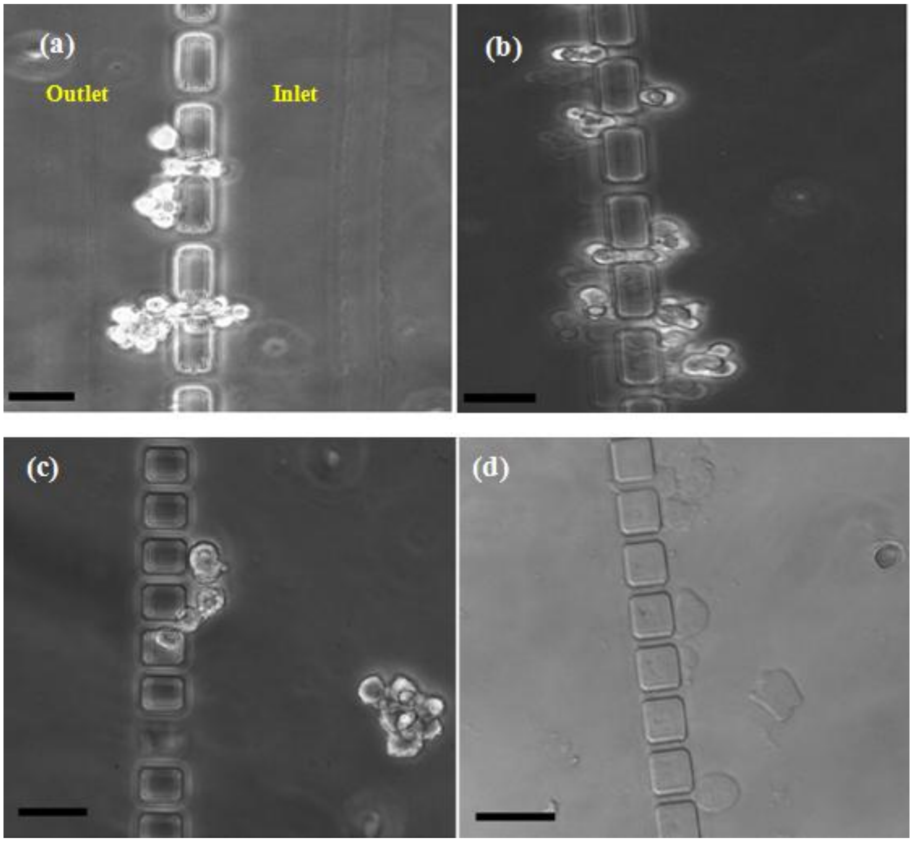

Figure 3-2: Cell captured in microfluidic devices in case of (a) Device-1; (b) Device-2; (c) Device-3; and (d) Device-4. The scale bars in all micrographs are 50 µm. The right side of channels is inlet and the left is outlet as mentioned for (a) [156].

Device Optimization and Calculation of Capture Efficiency

The microfluidic device design is portrayed schematically in Figure 3-1. To determine the baseline efficiency of the device to isolate cancer cells, high concentration of cell were in 1X PBS and flown through the microdevices at a flow rate of 1 mL/hr. The cross-sectional areas of the channels were altered by changing the thickness of SU8 in master used as template for PDMS. Average diameter of cancer cells was approximately 15 µm, but most of the cells squeezed through the channels in Device-1 because of their highly elastic nature. Some cells were captured in the channels and cluster of cells were observed around the channels as shown in Figure 3-2(a). The average capture efficiency (*η*) for this device was 31.04±2.5%. The following equation was used to enumerate capture efficiency of the devices.

$$\eta = \frac{X}{X+Y} \times 100\% \qquad \dots\dots\dots (3\text{-}2)$$

In this equation variable *X* and *Y* are representing the number of cells remaining in the inlet and the number of cells that made it to the outlet, respectively.

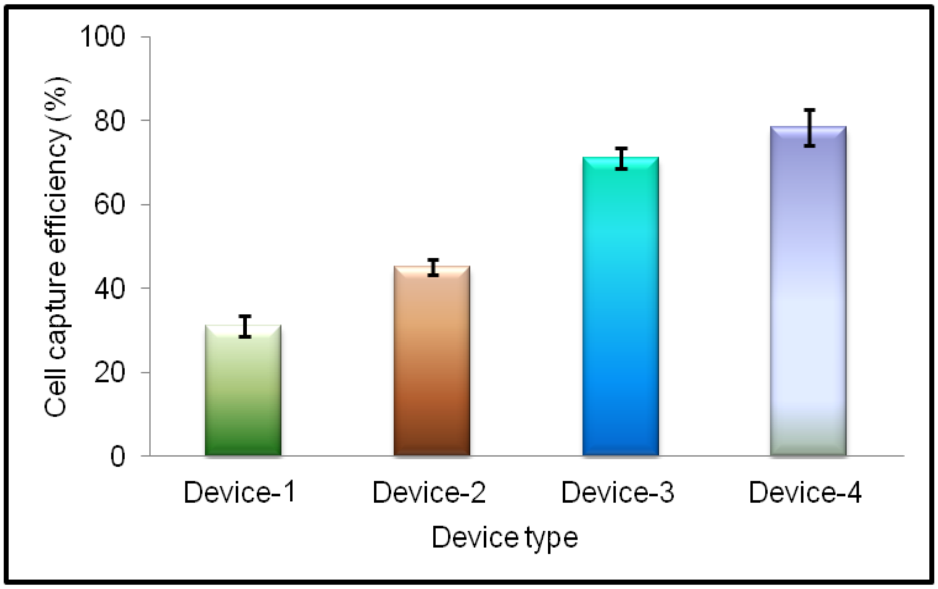

Figure 3-3: Average of tumor cell capture efficiency of four devices (n=2) [156].

In addition to mechanophysical properties, there might be some other factors that cells passed through the channels. First prime factor could be the heterogeneity in the sizes of cancer cells. Shape and orientation of the cells could be another reason; cells are globular in shape but channels were rectangular. Also the exact range of Young's moduli for cancer cells is unknown. All these factors were remained same from device to device, thus their contributions can be discounted. To enhance capture efficiency, the height was lowered to 10 µm (Device-2) for reducing the total cross-sectional area available for the cells to pass through. Consequently cell capture efficiency of the device increased to 45.18±1.85%. Still more than half of the cells were able to pass through the channels as shown in Figure 3-2(b). Next two devices were fabricated with channel dimensions of 10 µm x 5 µm (Device-3), and 5 µm x 5 µm (Device-4) and capture efficiencies jumped to 70.96±2.39% and 78.36±4.29% respectively (Figure 3-3). For every device, experiment was repeated at least two times and the results clearly exhibited a statistically different behavior that followed an almost monotonic trend. It can be observed from Figure 3-2 that cells are passing through the channels in Device-1 and Device-2. Therefore the cell clusters are found on both sides of the channels (Figure 3-2(a) and (b)). On the other hand, no clusters of cells are observed on the outlet side of the Device-3 and Device-4 (Figure 3-2(c) and (d)). Furthermore, as cells had more space to traverse through in Device-1 and Device-2 compared to Device-3 and Device-4, higher number of cells were hanging around the channels in first two devices.

It was also deduced that all the size of the cells varied within a large range and it had significant impact on cell capture efficiency. By calculating the size of the cells from images using *ImageJ,* it was found that the cells blocked in Device-1 had average diameters of 18.44±3.597 µm, while the cells captured in Device-4were of average diameter 15.215±3.536 µm (Figure 3-4). For Device-2 and Device-3 these diameters were 17.25±2.129 µm and 15.26±4.967 µm, respectively. That indicates that all cancer cells were not of same size and while flowing through a microchannel, they squeezed up to a certain limit depending on their sizes. This brings out the significant aspect of the cell elasticity dependence on its size. Previous studies have just looked at elasticity of tumor cells as a whole but maybe the elasticity is further dependent on the grade of tumorigenesis, stage of cell division, amount of overexpression/downregulation of various markers, etc.

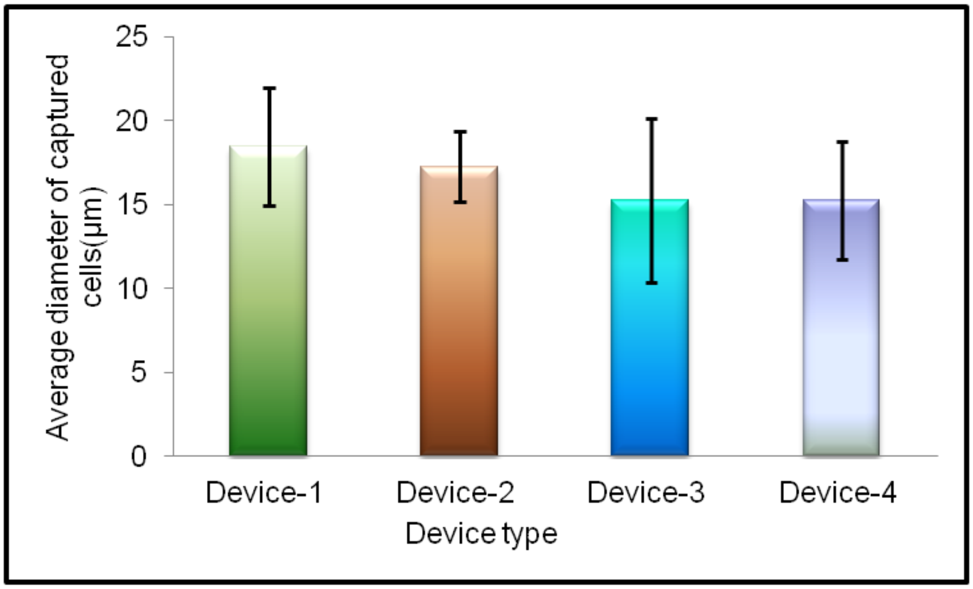

Figure 3-4: Average diameters of the cells blocked by four devices [156].

As the flow rate was same for all cells, the pressure applied to each cell, and consequently the shear force, was also same. So if it is considered that all cells have same Young’s modulus then strain on each cell would also be the same. From the simple definition of Young’s modulus the final size of the cells should be linear function of their initial size. Consequently, larger cells are blocked and smaller cells passed through. From viability analysis of renal cancer cells in Device-4 it was found that cell viability was above 74% for the cells that were able to pass through microchannels and came out from the outlet chambers.

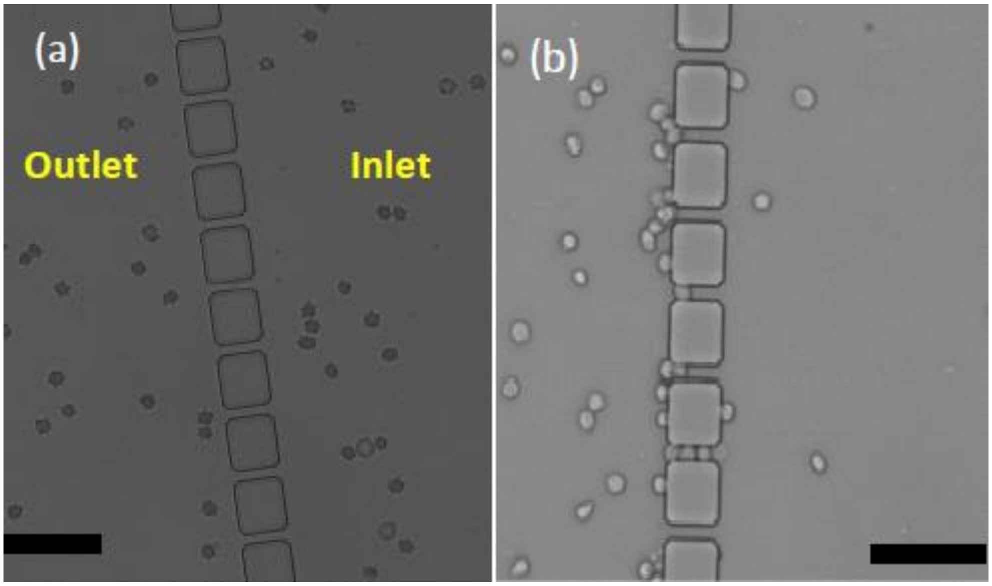

Figure 3-5: Blood introduced in (a) Device-3; and (b) Device-4. RBCs and WBCs passed through the microchannels. The scale bars are 50 µm [156].

Detection of Cancer Cells from Blood

Optimized devices (Device-3 and Device-4) were employed to run experiments with diluted blood samples obtained from rat. Blood cells (WBCs and RBCs) were smaller in size and able to pass through the microchannels quite easily (Figure 3-5). In Device-4, microchannels created obstacles for some WBCs but eventually passed through without creating any cluster or blockage. Though some WBCs may be larger in size but it has been reported before that RBCs and WBCs can traverse through capillaries of 2-5 µm [28]. However, next tumor cells were spiked in diluted blood at a concentration of 1000 cells/mL and experiment was run with Device-4. From optical micrograph it was observed that some cells were captured by the channels as shown in Figure 3-6 (a). As WBCs and RBCs were able to traverse through the channels and channel dimensions of Device-4 were optimized to capture renal cancer cells with high efficiency, it can be safely concluded that the blocked cells from blood sample are indeed cancer cells.

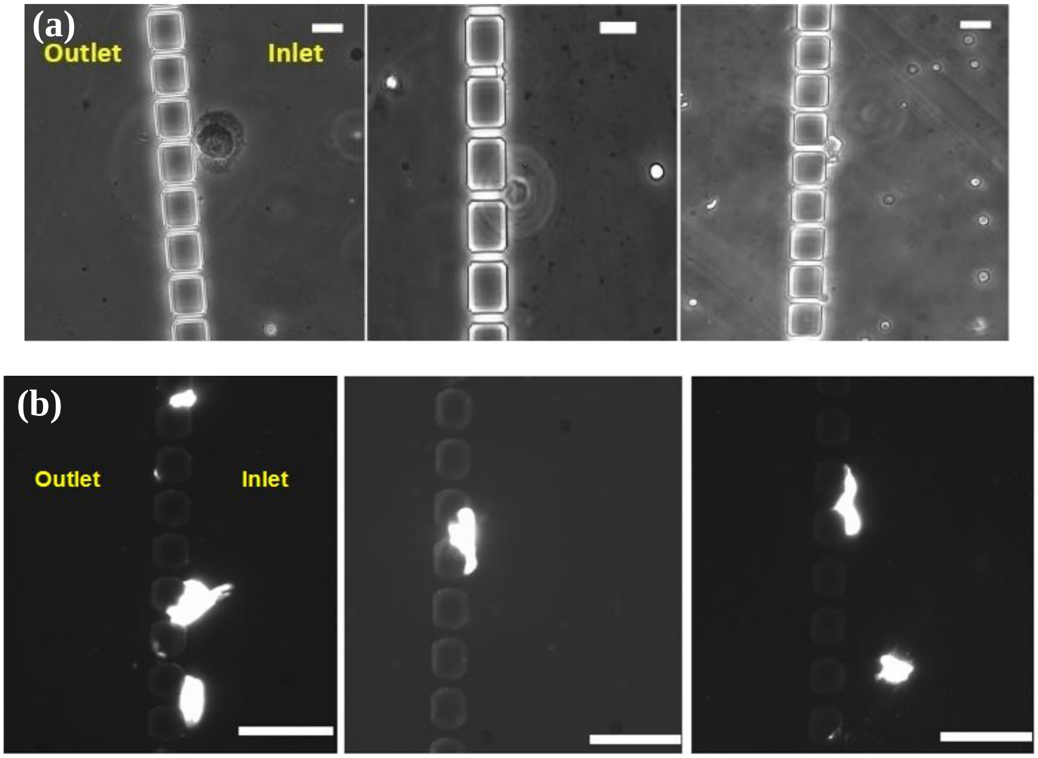

Figure 3-6: Isolation of cancer cells from rat blood using Device-4; micrographs of the devices (a) optical; (b) fluorescence. The scale bars are 50 µm [156].

But for ensuring the discrimination of tumor cells from blood and to determine capture efficiency fluorescent images of the devices were taken (Figure 3-6(b)). By analyzing all the images it was determined that this device was able to isolate the tumor cells from blood mixture with an average efficiency of 78.20±2.57%. Thus, in this case efficiency is very similar to that one which was achieved from the optically-observed devices to isolate tumor cells from PBS solution.

In addition, tumor cells were very flexible and could change their shapes while trying to squeeze through the smaller microchannels, but clearly the shear force of the flow was not high enough. Smaller shear force did not result in the cell squeezing through, counter-intuitive to the more flexible nature of the cells. Some of the captured cells by microchannels were distorted in shapes.

Conclusions

A microdevice is applied to detect metastatic renal cancer cells. Physical and mechanical properties of the cells were considered to discriminate them from RBCs and WBCs. The highly deformable nature of cancer cells was observed. These cells can squeeze through very small pores. The device consisted large number of channels to reduce shear stress on each cell to minimize deformability of cancer cells and detect them successfully with an efficiency of more than 78%. It was observed that the optimized channels were large enough for WBCs and RBCs to pass through. This simple and inexpensive device can be implemented in point-of-care module for the detection of CTCs from blood samples.

Chapter 4

NANOTEXTURED POLYMER SUBSTRATES FOR ENHANCED CANCER CELL ISOLATION AND CELL GROWTH

Introduction

Early detection of cancer can decrease the mortality rate significantly [6]. Affinity interactions based cancer detection and sorting scheme, especially with aptamers, can provide high specificity and selectivity [15, 47]. EGFR specific RNA aptamer functionalized substrates have been employed to recognize, capture and isolate hGBM cells with high specificity and selectivity [13, 157]. Cell capture and growth are affected by nanotextured topography of aptamer grafted molecules [13, 119, 158, 159]. In tissue engineering, nanostructured scaffolds have remarkably increased the densities of certain cells [160, 161]. The main advantage of nanotextured surface is the availability of increased surface area to anchor high quantity of protein or nucleic acid [13, 119, 162, 163]. Different processes have been reported to create nanotextured surfaces which are micro-contact printing, stencil assisted patterning or long polymer chemical etching [13, 158, 164]. These processes are time consuming and expensive. Plasma etching can be used as a simple and rapid method to make nanotextured surfaces [162, 163, 165].

Due to stable chemical and physical properties PDMS has been used widely in biomedical research specially to fabricate microfluidic device [166]. An easy way to prepare 3-dimensional, nanotextured PDMS substrates are described here. Micro reactive ion etching (Micro-RIE) was performed to prepare nanotextured PDMS surfaces. These surfaces were functionalized with anti-EGFR aptamers for the isolation of tumor cells overexpressed with EGFR. It was observed that the nanoscale features of PDMS increased the affinity of cancer cell attachment by providing larger surface area for aptamer immobilization. The increased surface area permits higher number of available aptamers on the surface to capture target cells. The nanotextured surfaces also provided higher cell growth. Especially for cancer cells the proliferation rate was as high as in the standard well plate used for cell culture. Comparison among three nanontextured surfaces showed almost linear relationships for both cell capture and cell growth with respect to surface roughness. The nanotexture enhanced cell capture probability and growth rate which is very important for microdevices used for detecting and enriching tumor cells. The key findings exhibited that nanotexture of the substrate could be quantitatively controlled to tweak the density of available ligands for possible match with the overexpression of oncogenes. Thus nanotextured PDMS devices can stage the cancer cells based on the overexpression. Primary steps of aptamer functionalization on nanotextured PDMS surfaces are shown in Figure 4-1(a) and Figure 4-1(b) and (c) are illustrating the principle of capturing target cells using aptamer grafted surfaces from a cell mixture with non-specific cells. The structure of aptamer molecules is changed while attaching to target cells.

Materials and Methods

All chemicals were obtained from Sigma-Aldrich (St. Louis, MO) unless noted otherwise.

Aptamer Preparation

Aptamer was prepared using a standard procedure reported earlier [13]. For anti-EGFR RNA aptamer selection with systematic evolution of ligands by exponential enrichment (SELEX) process, purified human EGFR (R&D Systems, Minneapolis, MN) was used. The anti-EGFR aptamers (K_d = 2.4 nM) were extended with a capture sequence. The amine-modified capture probe was used to immobilize aptamers on the substrate through duplex formation. The sequences of the extended anti-EGFR aptamers and substrate-anchored capture molecules were: anti-EGFR aptamer, 5'-GGC GCU CCG ACC UUA GUC UCU GUG CCG CUA UAA UGC ACG GAU UUA AUC GCC GUA GAA AAG CAU GUC AAA GCC GGA ACC GUG UAG CAC AGC AGA GAA UUA AAU GCC CGC CAU GAC CAG-3' and substrate anchored capture DNA, 5'-amine-CTG GTC ATG GCG GGC ATT TAA TTC-3' [13].

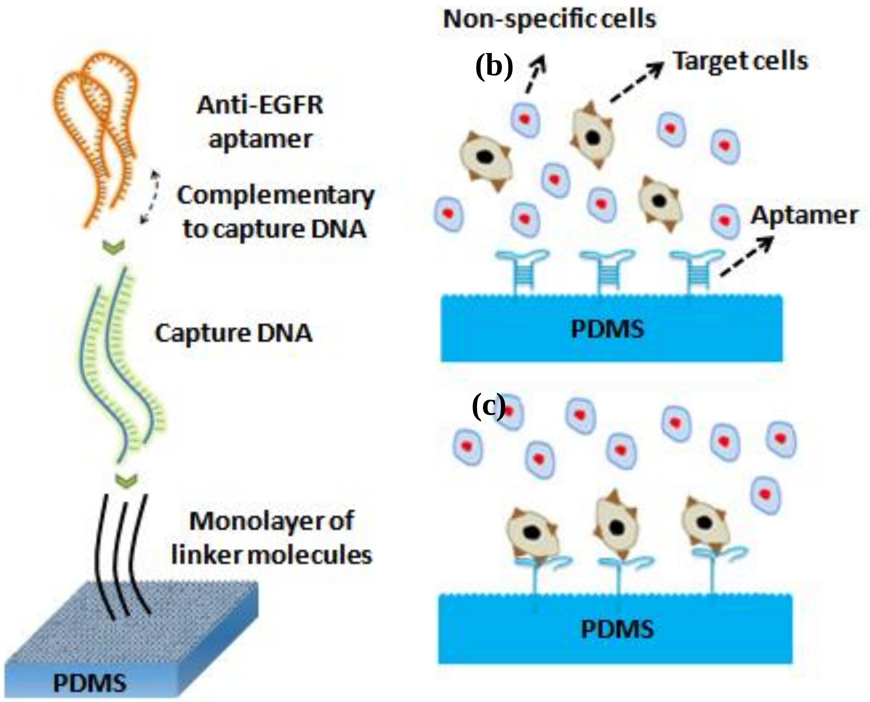

Figure 4-1: (a) Aptamer attachment protocol on nanotextured PDMS surfaces; (b) introduction of cell mixture on functionalized surface; (c) capturing target cells by aptamer grafted surface.

Preparation of Nanotextured PDMS Substrates

PDMS was mixed (10:1, wt/wt) with Sylgard 184 silicone elastomer curing agent (Dow Corning) and degassed in a desiccator for 1 h to remove all air bubbles. PDMS was then poured on 4 inch silicon wafer and heated to 75 °C for 5 min and then 150 °C for 10 min. Next, the PDMS was peeled off from the silicon substrate and cut into small pieces (~2 inch x ~2 inch). These substrates were cleaned in isopropyl alcohol (IPA), rinsed in deionized (DI) water and dried in nitrogen. A reactive ion etch (RIE) series 800 plasma system was used to prepare nanotextured PDMS. Three recipes were used in this system to etch the PDMS using mixture of oxygen (O_2) and carbon tetrafluoride (CF_4). First of all, the etching was performed with two ratios of etchant gases for 12 min. In recipe 1, the flow rate of O_2 and CF_4 was 10 sccm, respectively (ratio of O_2:CF_4 was 1:1) and in recipe 2, flow rate of O_2 and CF_4 was 7 sccm and 14 sccm, respectively (ratio of O_2:CF_4 was 1:2). In recipe 3, the flow rate of gases was same as recipe 1 but the etching time was increased to 25 min. After etching, each substrate was cleaned in sonicated IPA followed by cleaning in piranha solution (H_2O_2:H_2SO_4, 1:3). In later part of this article, three PDMS surfaces prepared by recipe 1, 2 and 3 will be named as Surface-1, Surface-2 and Surface-3, respectively.

Surface Characterization

Surface topography of PDMS surfaces was evaluated quantitatively by a Dimension 5000 atomic force microscopy (AFM). The root mean square surface roughness was measured. Micrographs of PDMS samples were captured in the ambient air with 15% to 20% humidity at a tapping frequency of approximately 300 kHz

[13]. The analyzed field measured 10 µm x 10 µm at a scan rate of 1 Hz with 256 scanning lines.

Elemental Composition of the Samples

Energy dispersive x-ray spectroscopy (EDS) was used for elemental analysis of plain and nanotextured PDMS. All samples were coated with thin layer of silver (Ag) before this analysis. Here an EDS detector (EDAX, Genesis) was attached to the scanning electron microscope (SEM). The SEM was focused at a 15 mm working distance with 20 kV accelerating voltage and data were recorded followed by mapping analysis.

Contact Angle Measurements

Contact angles for plain and nanotextured PDMS substrates were measured using a contact angle goniometer (NRL-100; Rame-Hart, Washington, DC). On average, 5 measurements were taken for each run. Angles were measured twice for each substrate. First, the angles were measured on substrates without any modification and next on substrates functionalized by isothiocyanate.

Attachement of Anti-EGFR Aptamer on PDMS Substrates

The aptamer attachment was adapted from our previous work [13]. PDMS substrates were further cut into 10 x 10 mm^2 pieces. These small pieces were cleaned with UVozone plasma for 30 min followed by piranha solution dip. These substrates were then rinsed with DI water and dried in nitrogen flow and immersed in 3% (v/v) of

(3-aminopropyl)triethoxysilane (APTES) in methanol for 30 min at room temperature. Next, the substrates were washed in DI water and methanol; and cured for 30 min at 120 °C. Substrates were then put in dimethylformamide (DMF) for 5 hours at 45 °C. DMF had 10% pyridine and 1 mmol/L*p*-Phenylenediisothiocyanate (PDITC) in it. After 5 hours, substrates were rinsed with DMF and 1,2-dichloroethane and dried in nitrogen gas. A 30 µmol/L concentration of capture DNA (which had a 5' amine group) was prepared using DI water with 1% *N,N*-Diisopropylethylamine (DIPEA) and substrates were incubated in DNA solution overnight in a humid chamber at 37 °C. After incubation, the substrates were washed with methanol and diethylpyrocarbonate (DEPC) treated DI water. Next, substrates were immersed for 5 hours in 150 mmol/L DIPEA in DMF and 50 mmol/L 6-amino-1-hexanol and again washed in ethanol, DMF, and DEPC-treated DI water. Then a glass chamber was properly washed with RNase free and DEPC treated DI water and PDMS substrates were placed in it. Then anti-EGFR RNA aptamer (1 µmol/L) dissolved in 1X annealing buffer [10 mmol/L Tris (pH 8.0), 1 mmol/L EDTA (pH 8.0), 1 mmol/L NaCl] was placed on each substrate. After 2 hours of incubation at 37 °C, substrates were washed with 1X annealing buffer and DEPC-treated DI water for 5 minutes. 1X PBS (pH 7.5) with 5 mmol/L magnesium chloride solution was prepared and the substrates were then placed in it before using for experiments. The experiments were run within several hours after functionalization.

Fluoresence Measurements

Surface modification was confirmed further by fluorescence measurements of acridin orange (AO) stain. DNA attached PDMS surfaces were used to measure intensity of AO. The AO solution of concentration 2 mg/mL was prepared in sterilized DI water. DNA functionalized plain and nanotextured PDMS surfaces were completely immersed into it and kept on the shaker for 30 minutes. Then all samples were washed thoroughly in DI water and fluorescence measurements were taken at 480 nm wavelength using Zeiss confocal microscope. The fluorescence intensities were analyzed with *ImageJ* (National Institutes of Health, Bethesda, MD).

Human Glioblastoma and Astrocyte Cell Culture

The culture of hGBM cells have been reported before [13]. These cells were cultured in chemically defined, serum-free Dulbecco's Modified Eagle's Medium (DMEM)/F-12 medium supplemented with 20 ng/mL mouse EGF (from Peprotech, Rocky Hill, NJ), 1X B27 supplement (Invitrogen, Carlsbad, CA), 1 insulintransferrin-selenium (Invitrogen), and penicillin: streptomycin 100 U/mL:100 µg/mL (HyClone, Wilmington, DE) and plated at a density of 3 x 10^6 live cells per 60 mm plate. The hGBM cells were transduced with a lentivirus expressing *mcherry* fluorescent protein. Human astrocyte cells were obtained from consenting patients at the University of Texas Southwestern Medical Center (Dallas, TX, USA) with the approval of the Institutional Review Board. The collected human astrocyte cells were cultured in DMEM/F-12 (Cellgro, Mediatech Inc.) with 10% fetal bovine serum. Gentamycin and L-glutamine (Invitrogen) were added to the cell culture medium. Standard cell culture conditions i.e. a sterile, humidified, 95% air, 5% CO_2 and 37 ^oC were maintained to incubate cells.

Tumor and Astrocyte Cells Capture on Substrates

First of all, cell suspensions were centrifuged and the supernatants were removed. Next, 1X PBS solution (with 5 mM $MgCl_2$) was added to dilute the cells to a concentration of 100,000 cells/mL. Approximately 500 µL drop of cell suspension was put on each substrate and incubated for 30 min at 37 °C. After incubation, substrates were washed with sterilized 1X PBS on a shaker at 90 revolutions per minute for 15 minutes [13]. Then substrates were observed and micrographs were captured using Leica optical microscope. *ImageJ* was used to calculate cell density from captured micrographs. For each type of surface, eight and six samples were prepared for hGBM and astrocyte cells, respectively. The cell capture efficiency on surfaces was also calculated by taking the ratio of total number of cells captured and number of cells suspended on each sample surface. Total number of cells captured on each sample was calculated from the cell density and total surface area of the samples. Statistical analysis was performed using one-way analysis of variance (ANOVA) for all types of surfaces.

In vitro Cell Culture Studies on Nanotextured PDMS

Fibroblasts, hGBM and human astrocyte cells were seeded on standard well plate, plain and nanotextured PDMS to observe the effect of nanotexturing on cell growth. All PDMS scaffolds were cut into 6 mm diameter circular disks, washed three times in DI water, dried in nitrogen flow and treated with O_2 plasma for 30 min. Next, scaffolds were washed in 70% ethanol for 30 min to sterilize. Again, all scaffolds were washed in DI water three times and dried. The samples were then coated with poly-Dlysine (PDL) by immersing the scaffolds in PDL solution for 24 h and then washed again in sterilized DI water thoroughly. Then samples were coated with laminin solution containing 10 µg/mL laminin in 1X PBS (PBS was Mg^{2+}/Ca^{2+} free) and incubated at 37 ^{o}C overnight to adhere laminin to the PDMS surfaces [119]. Next, samples were washed in sterilized 1X PBS and freshly harvested human fibroblasts, hGBM and human astrocyte cells were seeded (1000 cells/mL) onto the samples. The sample surfaces were observed under optical microscope after 3 days. For each type of surface, five samples ($n = 5$) were prepared. Statistical analysis was also performed using one-way ANOVA for all types of surfaces.

Results and Discusion

Surface Topography of Nanotextured Substrates

The average roughnesses found from AFM were 242.92±87.71 nm, 515±102.28 nm and 629.17±109.67 nm for Surface-1, Surface-2 and Surface-3, respectively (Figure 4-2). Thus higher surface roughness was achieved when the ratio of CF_4 was higher than O_2. But similar feature was obtained by using same amount of O_2 and CF_4 for longer period of time. Therefore, it can be said that the features of nanotextured surfaces can be controlled by both the etch time and ratio of oxygen and carbon tetra fluoride. Moreover, this approach can be used to create nanotexture in microfluidic devices fabricated in PDMS. The devices will need to be fabricated first in PDMS and exposed to micro-RIE to create nanotexture. Template based techniques to create nanotexturedsurfaces have been reported [16, 17], but the presented method does not require any template.

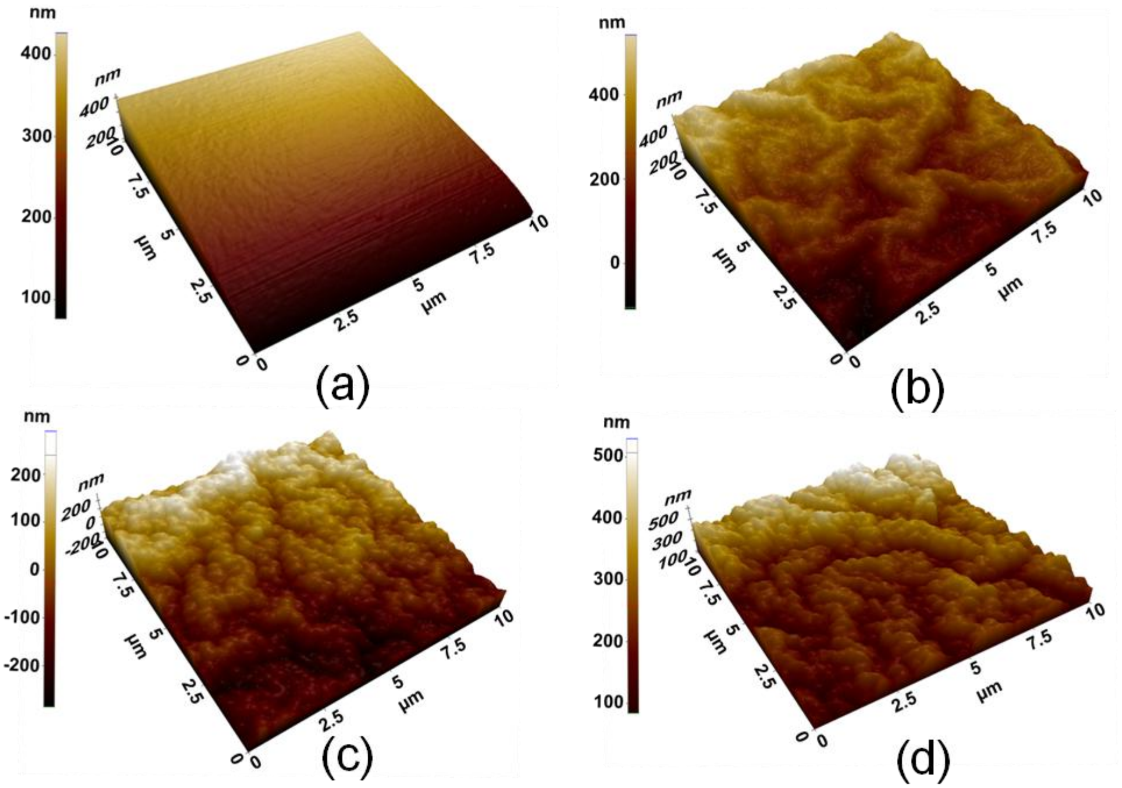

Figure 4-2: AFM micrographs of the plain and nanotextured PDMS surfaces. The micrographs represent (a) plain PDMS surface; nanotextured PDMS surfaces obtained by micro-RIE using O_2 and CF_4; (b) after 12 min (O_2:CF_4, 1:1); (c) after 12 min (O_2:CF_4, 1:2); and (d) after 25 min (O_2:CF_4, 1:1). Reprinted with permission [200].

Elemental Analysis and Compositional Mapping

PDMS is a polymer which is made of $SiOC_2H_6$ monomer. Energy dispersive X-ray spectroscopy (EDS) elemental analysis of plain PDMS showed that it comprises of silicon, oxygen and carbon (Figure 4-3(a)). Silver came from the coating. Hydrogen could not be detected in EDS analysis. Because hydrogen atom is very small with lower atomic number. Micro-RIE was conducted on plain PDMS surfaces to get nanotextured PDMS using O_2 and CF_4. The EDS elemental analysis of nanotextured PDMS (Surface-3) had almost identical results (Figure 4-3(b)). That means the etching did not make any change in chemical nature of PDMS.

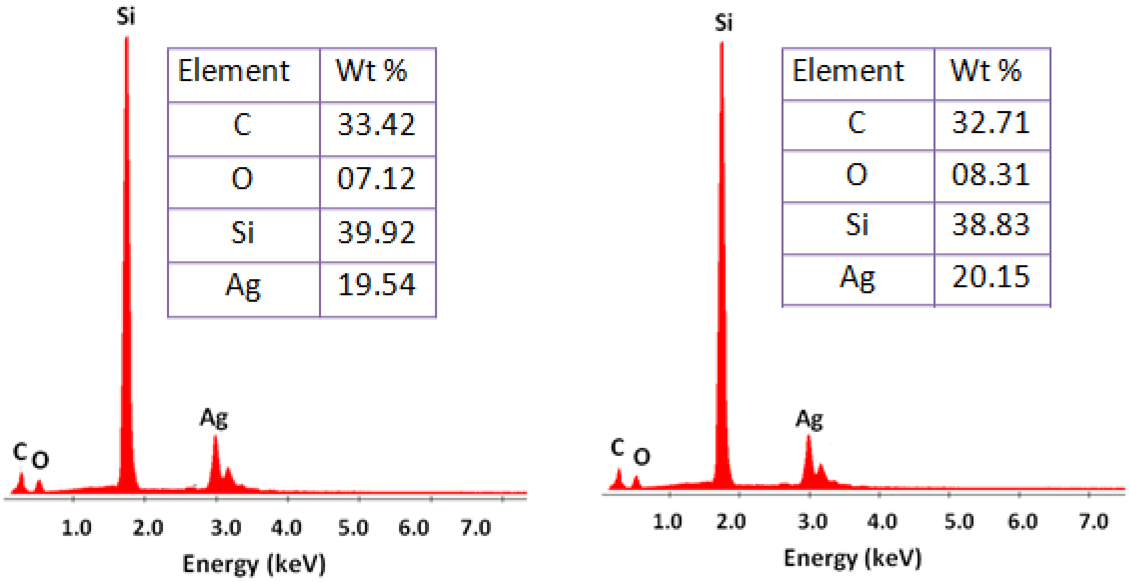

Element	Wt %
C	33.42
O	07.12
Si	39.92
Ag	19.54

Element	Wt %
C	32.71
O	08.31
Si	38.83
Ag	20.15

(a) **(b)**

Figure 4-3: EDS elemental composition of (a) Plain PDMS and (b) Nanotextured PDMS (Surface-3) [200].

Contact Angle Measurements

Contact angle of a water droplet indicates the hydrophobicity or hydrophilicity of a surface [13]. Contact angle is more than 90^{o} for hydrophobic surfaces, otherwise it is hydrophilic. Nanotexturing increased both the hydrophobicity and hydrophilicity of a hydrophobic and hydrophilic surface respectively [13, 163]. The contact angles of all experimental surfaces are given in Table 4-1. All bare surfaces were hydrophobic and after APTES and isothiocyanate functionalization, all substrates became hydrophilic.

Table 4-1: Contact angles measured on bare surfaces and after chemical activation with phenylene di-isothiocyanate (PDITC)) *(n=5)*

Substrate Type	Base Substrate	After PDITC Treatment
Flat PDMS	112.2 ± 2.77	66.2 ± 2.17
Surface-1	126.8 ± 3.11	56.2 ± 2.28
Surface-2	139.8 ± 2.39	52 ± 2.45
Surface-3	145.4 ± 2.19	48.4 ± 1.95

Fluorescence Measurements

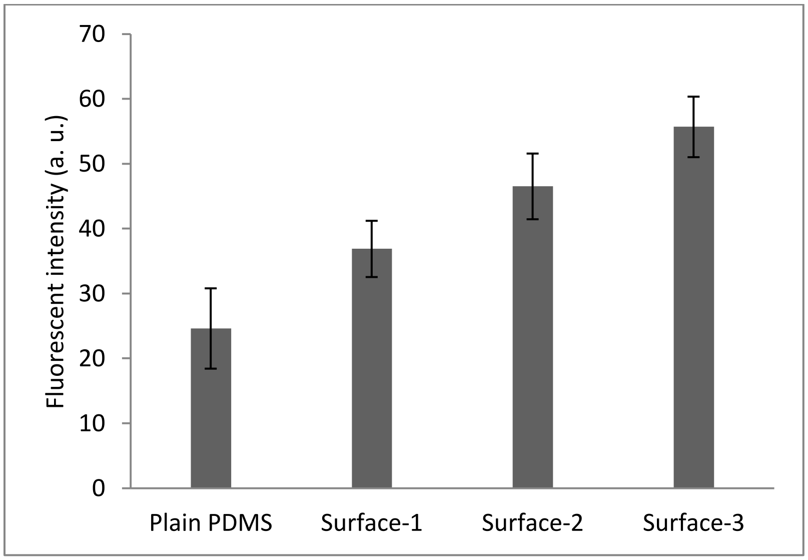

Figure 4-4: Fluorescence intensity from AO stain [200].

Plasma treatment and exposure to piranha solution increased the number of available hydroxyl groups on PDMS surfaces. It helped to enhance the number of amino groups from adsorbed APTES. This indeed enriched the number of attached DNA molecules on the surface which finally increased the total number of immobilized aptamers [13]. Fluorescence intensities of AO were determined to compare the relative number of DNA molecules on all substrates. Figure 4-4 is showing the average intensities of all the substrates. Nanotextured PDMS substrates provided higher signals compared to plain PDMS. The highest intensity was observed in Surface-3 and lowest for Surface-1. Nanotexture amplified available surface area and generated higher number of hydroxyl groups, thus more amino groups and consequently higher number of DNA got immobilized. Higher number of DNA is favorable to attach increased number of aptamer molecules on the surface and as a result tumor cell isolation was much enhanced. It is reported that the packing density of anchored DNA depended on radius of gyration of the molecules and the radius of gyration determined the footprint of a molecule and density of packing [167]. Nanotextured surfaces shorten the distance between the immobilized ends of the probes as free ends had more room on a curvaceous surfaces and need smaller footprint compared to flat surface for same radius of gyration [13]. Hence, nanotextured surfaces had higher probe density. For same areal size nanotextured surfaces also offered higher effective area than plain surface. That’s why total number of captured molecule was elevated and nonspecific aptamer adsorption was decreased on nanotextured surfaces. Non-specific adsorption of aptamers occurred due to van der Waals forces only if aptamers could find their way to the surface. But negative charge of tightly packed DNA repelled aptamers and minimize non-specific adsorption [13].

Among three nanotexturedPDMS surfaces fluorescence intensity was lowest for Surface-1. But Surface-2 and Surface-3 showed higher intensity as they had higher surface roughness. Again, roughness of Surface-3 was higher and consequently density of DNA molecules was higher compared to Surface-2. Therefore, fluorescence intensity was highest for Surface-3.

Isolation of hGBM and Astrocyte Cells

Figure 4-5(A-D) represents micrographs of hGBM cells captured on anti-EGFR aptamer grafted plain and nanotextured PDMS substrates. Average densities of hGBM and astrocyte cells were calculated after washing the substrates with 1X PBS at 90 revolutions per minute for 15 min. By analyzing the optical micrographs, average number of captured hGBM cells was found lower on plain PDMS compared to nanotextured PDMS surfaces. The average cell density for plain PDMS surface was 49.25±7.21 per mm^2 and for surface 1, 2 and 3 cell densities were 103.75±5.28 per mm^2, 146.75±5.50 per mm^2, and 166.38±7.19 per mm^2, respectively. From cell density on surfaces, the cell capture efficiency calculated for plain PDMS surface was only 9.85% where as for Surface-3 it increased to 33.28%. Average cell densities of astrocyte cells did not vary significantly for all of these surfaces (Figure 4-5(E-H)). For plain PDMS, it was 28±9.80 per mm^2 and for surface 1, 2 and 3 it was 36±15.18 per mm^2, 38±14.03 per mm^2, and 44±14.53 per mm^2, respectively. Figure 4-6(a) is showing the quantitative results for both types of cells on all surfaces and Figure 4-6(b) is representing the linear relationship between surface roughness and cell capture density. All these substrates were modified with anti-EGFR aptamer. Density of hGBM cells depended on the available number of anti-EGFR aptamer molecules on the substrate, the density of EGFR on cell membrane, the affinity between EGFR and aptamer, and the surface roughness of the substrate [13].

Availability of aptamer molecules depended on surface nanotexture and the nanotexture also increased affinity between surface and aptamers by providing biomimectic environment for the cells. Nanotexture allowed more surface area for aptamers to be attached on the surface. Thus, cell capture density was higher. Cell capture density was proportional to surface nanotexturing. The relationship between surface roughness and density of captured hGBM cells was almost linear. Surface roughness and cell capture density of tumor cells both were highest for Surface-3 and lowest for Surface-1. Statistical analysis, one-way ANOVA, showed statistically significant differences (p-value < 0.01) in cell density for three surfaces.

For astrocyte cells, density of captured cells were little higher on nanotextured PDMS surfaces but the differences were not as high as for tumor cells. From Figure 4-6(a), it is obvious that number of captured cells was very lower for astrocyte on nanotextured PDMS with respect to hGBM cells. The functionalized nanotextured surfaces had very high number of available aptamers, thus reduced the non-specific binding of astrocyte cells on the surfaces. It represents the essential trade-off between sensitivity and selectivity. On the whole, the nanotextured surfaces offered higher sensitivity but also suffered from lower specificity. The end-goal would define optimal levels of nanotexturing for particular applications against various cancers but here we can see that the nanotextured surfaces are advantageous to increase isolation of rare cancer cells. The data also supports to the fact that for one type tumor cells, with one level of receptor overexpression, the isolation efficiency can be increased by simply increasing the number of available ligands. Nanotexture of the PDMS substrates gives an easy and straight-forward way to do that in microfluidic channels.

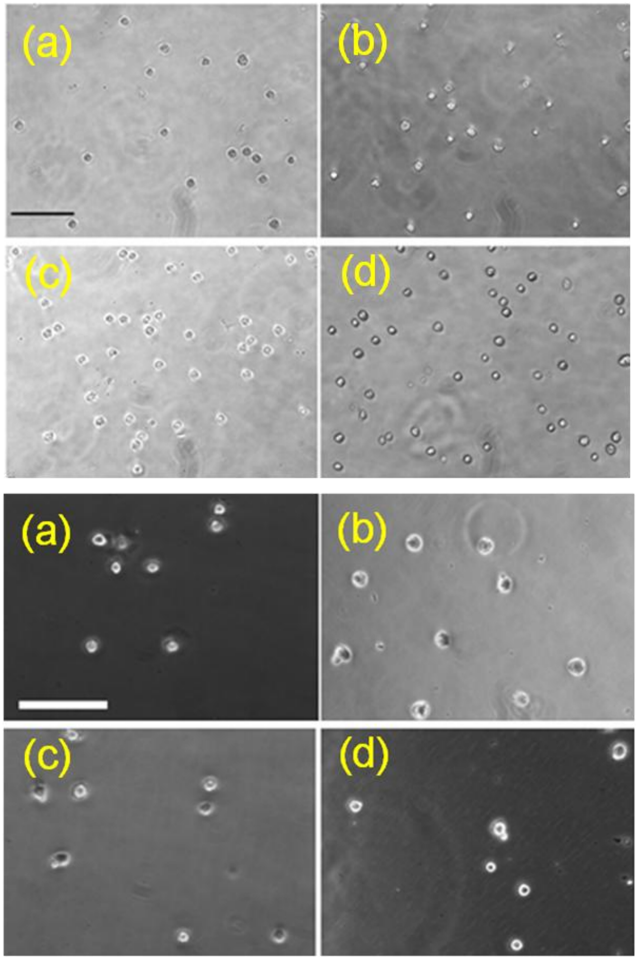

Figure 4-5: The hGBM and astrocyte cells on the anti-EGFR aptamer modified surfaces; hGBM cells on (a) plain PDMS surface; (b) Surface-1; (c) Surface-2 and (d) Surface-3; and astrocyte cells on (e) plain PDMS surface; (f) Surface-1, (g) Surface-2 and (h) Surface-3. Scale bar = 100 µm in (a) is also applicable for (b)-(d) and (e) is also applicable for (f)-(h). Reprinted with permission [200].

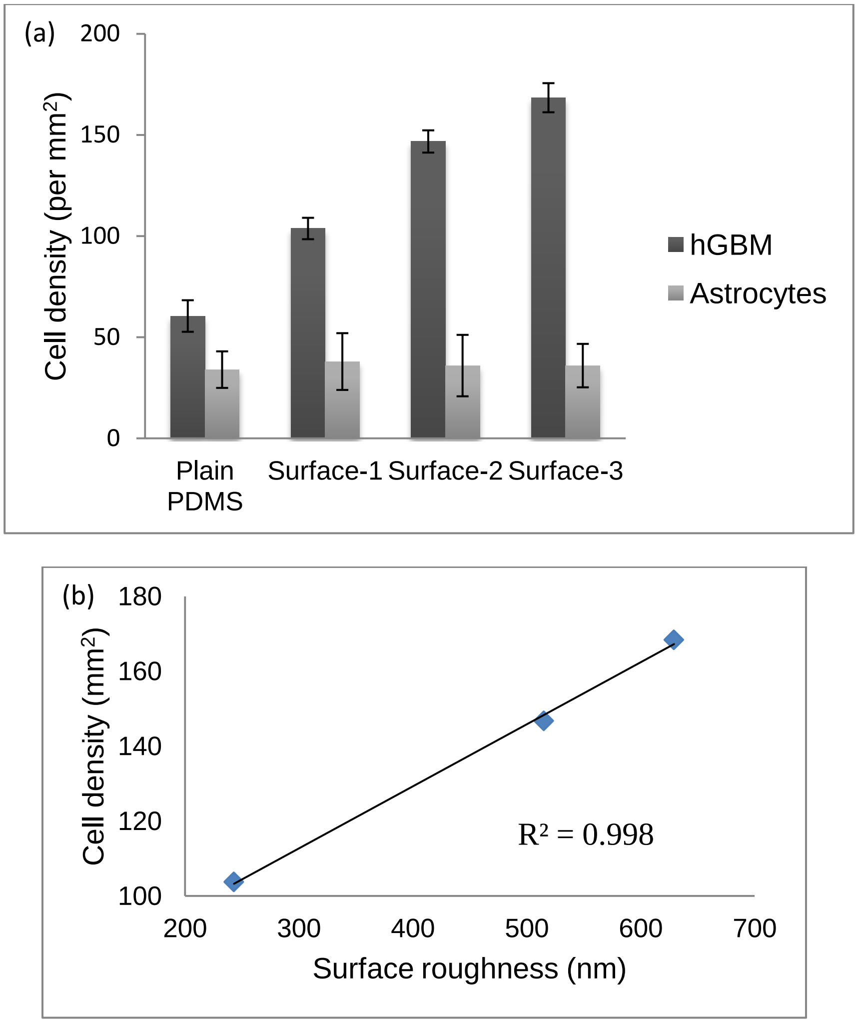

Figure 4-6: (a) The average cell density (cell number/mm^2) of hGBM and astrocyte cells on aptamer functionalized PDMS surfaces; (b) relationship of surface roughness and cell density of captured hGBM cells [200].

In vitro Cell Growth on Nanotextured Surfaces

Three types of cells were seeded on four PDMS surfaces and standard polystyrene well plates. All the surfaces were coated with Laminin before seeding the cells. Nanotextured surfaces allowed higher growth rate compared to plain PDMS surfaces for all types of cells (Figure 4-7). For all cases, Surface-3 showed highest cell density among three nanotextured surfaces. Density of astrocyte cells increased to 114±16.15 cells per mm^2 on Surface-3 as plain PDMS had 28±3.58 cells per mm^2. But the standard well plate had higher cell density compared to Surface-3. Similarly, density of fibroblasts cells was also higher in well plate (349.6±20.12 cells per mm^2) compared to Surface-3 (272.80±13.68 cells per mm^2). One-way ANOVA analysis showed statistically significant differences in all substrates for astrocyte and fibroblast cells except for astrocyte cells in Surface-2 and Surface-3. In this case, the cell density did not vary significantly (p-value > 0.29). For hGBM cells, statistical difference among well plate, Surface-2 and Surface-3 was not remarkable (p-value > 0.39). Therefore, only for hGBM cells, nanotextured surfaces showed high cell growth similar to well plate.

A limitation of plain PDMS surface is even after chemical modification, it is hard to maintain cells on surface, especially for long-term cell culture due to the absence of stable cell-adhesive layer [13, 168]. The hydroxyl groups go through dehydration reaction and high chain mobility pulls the hydrophobic methyl groups to the surface and prevents the generation of a cell-adhesive layer. Similar occurrence happened to nanotextured PDMS surfaces. But nanotexturing upgraded cell attachment and isolation by increasing surface area which allows more protein attachment and allows cell adhesion and growth. Consequently, the nanotextured surfaces allowed higher cell growth. For tumor cells, the proliferation was comparable to standard well plate. But for healthy cells, well plate had much higher cell growth compared to nanotextured surfaces. That suggests that tumor cells have higher affinity towards nanotextured surfaces compared to healthy cells. Therefore, nanotextured PDMS surfaces can be efficient tool in microfluidic platforms for isolation and growth of tumor cells as standard well plate materials are not compatible with microfluidic devices.

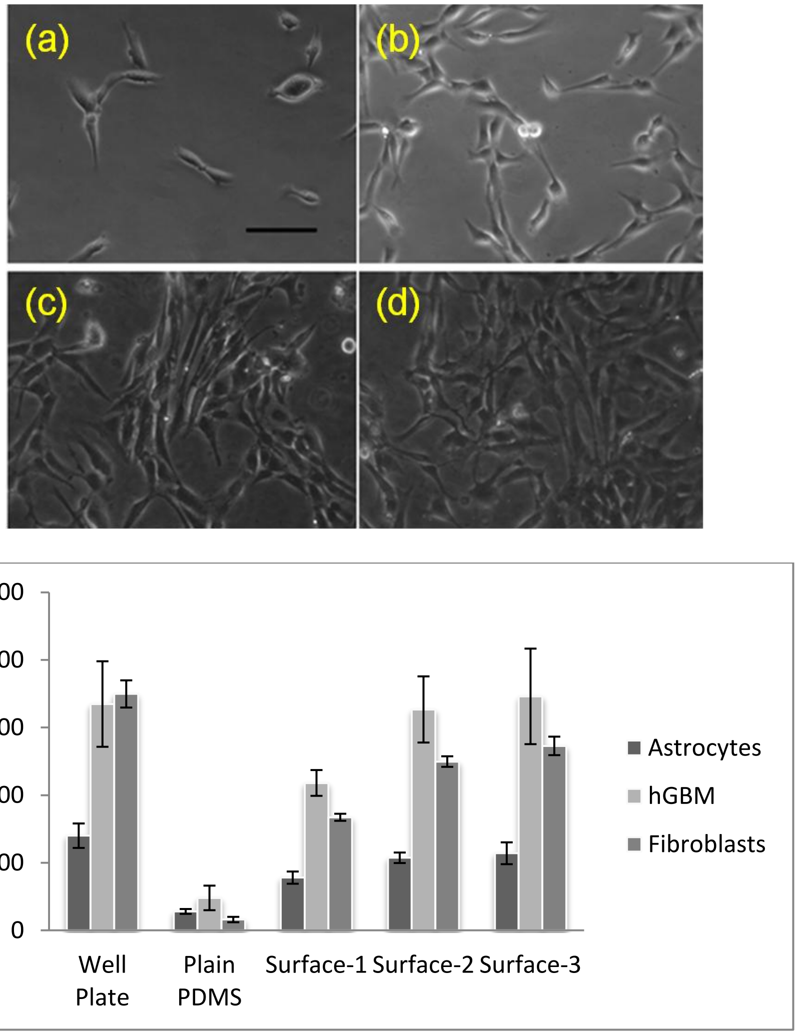

Figure 4-7: The hGBM cell growth on plain and nanotextured surfaces as well as in the culture plate (a) plain PDMS surface; (b) Surface-1; (c) Surface-2; (d) Surface-3; and (e) the average cell densities (cell number/mm^2) for hGBM, astrocyte and fibroblast cells on all surfaces; Scale bar = 100 µm in (a) is also applicable for (b)-(d). Reprinted with permission [200].

Conclusions

Nanotextured PDMS surfaces give rapid and inexpensive ways of fabricating better substrates cell isolation and cell-culture. Micro-RIE can provide better control to create nanotextured surfaces of desired roughness. For the detection of CTCs, a device must have high cell capture efficiency and faster cell growth facility. By simply introducing nanotexture in microfluidic devices it is possible to achieve these both potentials. The surface roughness effect cell capture and cell growth almost linearly. That’s why nanotextured PDMS could be implemented in microfluidic biosensors. Therefore, nanotextured surfaces can be incorporated in point-of-care device for the detection of tumor cells.

Chapter 5

NANOTEXTURED MICROFLUIDIC CHANNEL FOR ELECTRICAL PROFILING AND DETECTION OF TUMOR CELLS FROM BLOOD

Introduction

Micropore has been reported to detect tumor cells from blood from their translocation behavior [6, 7]. The CTCs exhibited characteristic electrical signals based on their mechanical and physical properties while measuring ionic current. It has been reported already that cancer cells have larger diameters than red and white blood cells (RBCs and WBCs). Cancer cells are also known to have different elasticity than healthy cells [94, 169, 170]. Again, cell behavior is influenced by nanoscale structure of the surfaces [13, 158]. Nanotexture surfaces have already been employed in biosensors [171-174]. Nanotextured surfaces can be prepared using various techniques as we mentioned in earlier. Here we implemented micro-RIE to create nanotextured PDMS microchannel to observe translocation profile of tumor cells and discriminate from blood. The reported microfluidic device, with nanotextured walls was employed to detect metastatic renal cancer cells from whole blood by measuring ionic current. Fluid pressure was applied using a syringe pump to push cells through microchannel. A pair of Ag/AgCl electrode was used to measure ionic current through the microchannel. The cells were suspended in phosphate buffered saline (PBS). Physical blockage of the channel by cells provided distinctive current pulses across microfluidic channel. Pulse magnitude depended on the cell size, and orientation and pulse duration corresponded to the time required for the cell to pass through the microchannel. The translocation time also depended on cell elasticity and cell-surface interactions inside the channel. Pulse shape related to the physical and mechanical properties of the cells. First of all, plain PDMS microchannel was implemented to discriminate tumor cells from blood. Next the nanotextured microchannel was for the same purpose. This time translocation of more than 50% of tumor cells became slower. Consequently nanotextured microchannel provided 14% higher detection efficiency of tumor cells compared to plain microchannel. The reported microdevice is simple, reusable and efficient. The soft lithography was used to fabricate the device. This method did not require fluorescent tags, surface functionalization or pre-processing of the blood sample for tumor cell detection.

Materials and Methods

Device Fabrication

The microfluidic device composed of one inlet and one outlet and a single microchannel connected them. The dimension of the channel was 20 µm x 20 µm x 5 µm (width x height x length) (Figure 5-1(a)). This device was fabricated by soft lithography using PDMS. The device was designed in AutoCAD and translated to a glass photomask. Then device was fabricated on a silicon wafer by spin coating SU-8 2010 (1000 rpm, 35 seconds) followed by photolithography. Next, the pattern was translated to PDMS as described in chapter 2.

To create nanotexture, the channel surface was etched in reactive ion etch series 800 plasma system. The etching was performed using oxygen (O_2) and carbon tetrafluoride (CF_4) for 20 min. After etch, device was washed in sonicated IPA followed by dip in piranha (H_2O_2:H_2SO_4 in a 1:3 ratio) solution. The PDMS and glass slides were treated with UV Ozone plasma for 15 min and hermetically bonded together. The fabricated devices were filled with 1X PBS with 5 mM magnesium chloride (pH 7.5).

Device Characterization

Zeiss LSM 5 Pascal Confocal Microscope and KLA-Tencor Alpha-Step IQ profilometer was used to image and measure heights of the features for the master fabricated in silicon wafer. A Dimension 5000 AFM evaluated the surface topography of PDMS and nanotextured PDMS surfaces quantitatively. The root mean square surface roughness was measured over scan area of 10 µm x 10 µm. Micrographs of PDMS samples were captured in the ambient air with 15% to 20% humidity at a tapping frequency of ~300 kHz. The analyzed field was measured at a scan rate of 1 Hz with 256 scanning lines.

Measurement Setup

The measurement setup was similar as reported before by our group [6]. Ag/AgCl electrodes were immersed in PBS that filled the microchannel and were used for ionic current measurements. The electrodes were connected to data acquisition cards (National Instruments) to bias voltage and measure current. The inlet of the device was connected to a syringe pump (Harvard Apparatus) through a tubing adapter. The entire measurement setup is shown in Figure 5-2(b). Cells were suspended in 1X PBS and injected into the inlet compartment using the syringe pump and passed to the outlet. While cells translocated through the microchannel, conductivity of the channel reduced. The conductivity of the channel *G* is given by,

$$G = sA/L \dots \dots \dots \text{(5-1)}$$

Here *s* is the conductivity of PBS solution, *A* and *L* are cross section area and length of the channel, respectively. The conductivity of the channel was reduced due to the reduction of the effective area caused by physical blockage created while cells were passing.

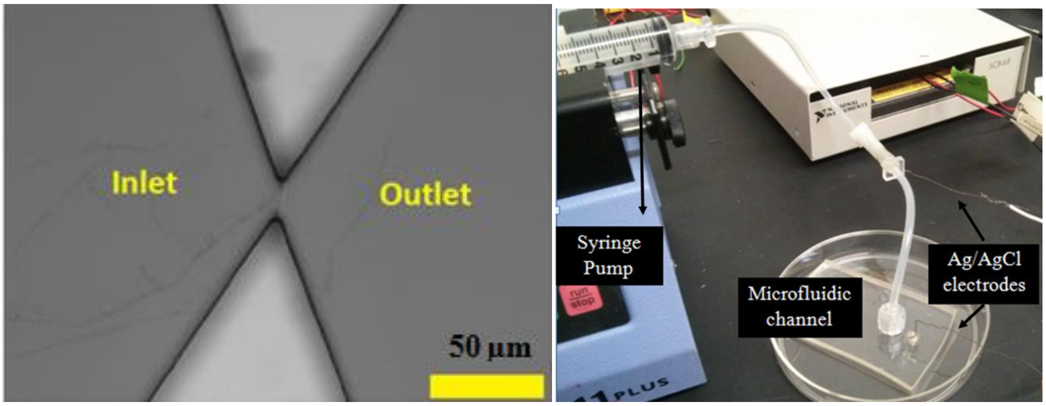

(a) (b)

Figure 5-1: (a) Micrograph of the microchannel; (b) Measurement setup, syringe pump connected to the inlet of microfluidic device. One Ag/AgCl electrode is connected through the tubing at the inlet and another to the outlet.

Human Derived Primary Renal Cancer Cell Culture and Collection of Rat Blood

The procedure for culturing human derived renal cancer cells and collecting of rat blood is same as mentioned in chapter 3. Metastatic renal tumor cells were isolated from the brain tissues of consenting patient at the University of Texas Southwestern

Medical Center at Dallas, Texas, USA as per the approved Institutional Review Board protocol [38]. The known metastasized renal derived cancer cells were collected in ice-cold Hank's medium. Then cells were chemically dissociated with papain and dispase (both 2%) as reported earlier [39]. Next cells were cultured in Dulbecco's modified Eagle's medium (DMEM) with 10% fetal bovine serum [6]. The renal cancer cells were stably transduced with a lentivirus expressing *mcherry* fluorescent protein. The blood samples were collected from tail of a rat by restraining the animal. The blood was collected in tubes with K2-EDTA as anticoagulant.

Results and Discussion

Surface Topography of Nanotextured Substrates

The measured average roughness of nanotextured surface was 519.17±103.71 nm. The AFM image of plain and nanotextured surfaces are shown in Figure 5-2.

Device Assembly

The microfluidic device had one microchannel that was assembled as described in the Materials and Methods section. The dimension of the channel was small enough so that multiple cells could not travel through simultaneously. The flow rate was optimized for the experiment. At higher flow rates, translocation events of some cells can be missed. Lower flow rates reduced the throughput of the device. To balance between these two conditions the experiments were run at a flow rate of 16.67 µL/min. Sampling frequency of the electrical signal was also optimized to have stable baseline and less noise. Lower frequency is favorable for stable baseline current and less noise. But the system might miss rapid translocation events. On the other hand, higher frequency generates inherent noise which suppressed some signals during cell translocation. The current sampling interval was optimized at 5 µs (0.20 MHz) and the applied bias voltage was 5 volts.

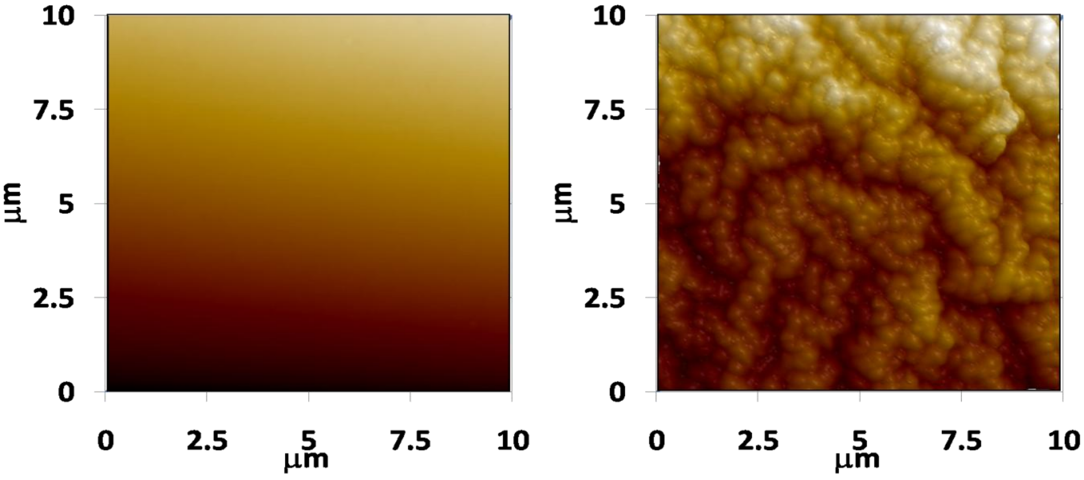

(a) (b)

Figure 5-2: Atomic force micrographs of (a) plain; and (b) nanotextured PDMS surfaces. Reprinted with permission [201].

Translocation Behavior of Tumor Cells through Plain and Nanotextured Microchannels

The metastatic renal cancer cells were suspended in 1X PBS at a concentration of 1000 cells/mL and passed through both plain and nanotextured microchannels for 10 min while current was measuring across microchannel. This experiment was repeated at least 5 times. From ionic current measurement data distinctive current pulses were found for tumor cells. The peak amplitude for tumor cells were similar in both types of channels but the average translocation time was higher in nanotextured microchannels compared to plain microchannels. Above 50% tumor cells had higher translocation time through nanotextured microchannels compared to plain microchannels (Figure 5-3(a)). The average translocation time in nanotextured microchannel was 60.40% higher compared to plain channel (Figure 5-3(b)). The magnitude of current drop depended on the physical blockage of the channel. Again amount of blockage depended on cell size, shape and orientation. As the cell sizes were same for both devices the peak amplitude remained identical (Figure 5-3(c)).

Nanotopographic surfaces have various influences on cell functions [175-182]. Nanotextured topography is more biomimectic and cell-stimulating cue as cells have to contact with nanotextured interfaces in vivo. Complex nanostructures are found in basement membranes of most tissue [175]. Cells can recognize and adjust with nanotextured surfaces in a selective manner. Cells adhered and probed with nanotextured surfaces and moved using nanoscale methods like filopodia and lamellipodia [176]. The membrane of cells got deformed and caused modification in cell functioning due to the topography. This had substantial impacts on mechanical properties of cells such as mechanical stretching, spreading, elasticity etc [175-179]. Nanotextured surfaces can also alter the elastic modulus of the cells by influencing the volume and shape [177-179]. Translocation time of a cell depended on cell elasticity [6] and cell-surface interactions [6, 7]. The combined effects of all these facts slower the translocation of tumor cells in nanotextured microchannels. Statistical analysis of translocation time and peak amplitude for tumor cells in plain and nanotextured microchannels were performed using one-way analysis of variance (ANOVA). The peak amplitude did not show appreciable statistical difference (*P*-value was 0.07) but translocation time was significantly different for two types of microchannels (P-value < 0.01).

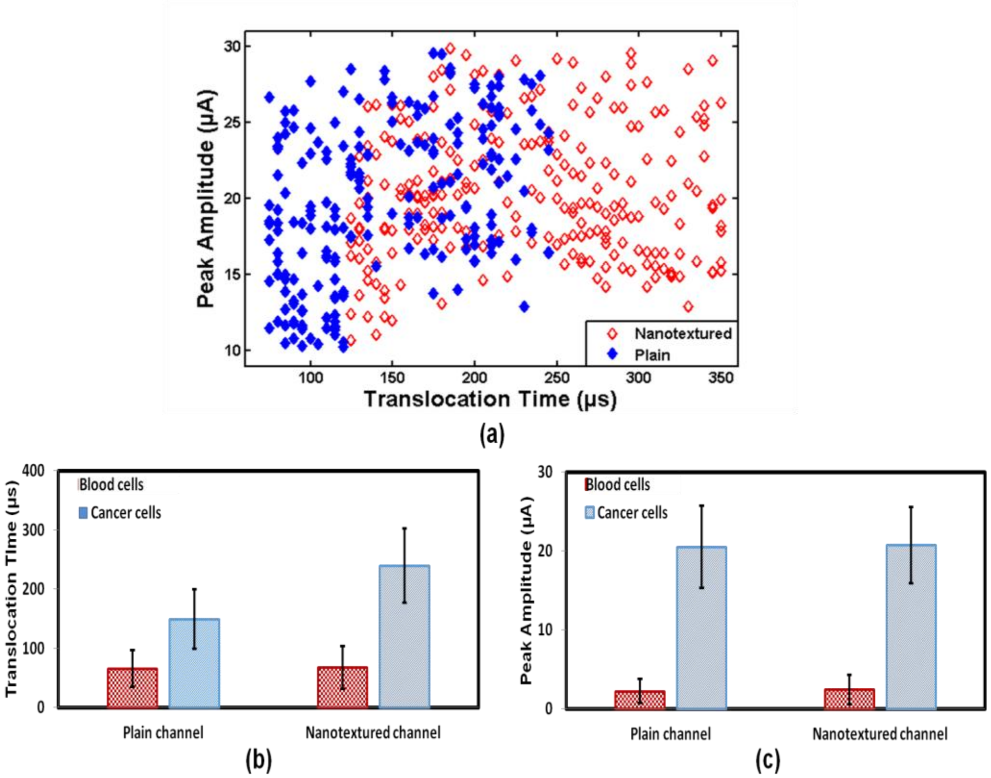

Figure 5-3: Translocation behavior of renal cancer cells through plain and nanotextured microchannels (a) characteristics plot for the cells; (b) average translocation time and (c) average peak amplitude ($n \approx 200$). Reprinted with permission [201].

Translocation Behavior of Blood Cells in Plain and Nanotextured Microchannels

Translocation profile of blood cells was determined through plain and nanotextured microchannels. Blood cells were diluted in 1X PBS at a ratio of 1:100 and processed through the microchannels for 5 minutes. The experiments were repeated at least three times and identical results were obtained. RBCs are smaller compared to WBCs and single RBC might be very small to create detectable pulse. Thus the microchannels may have missed some pulses of RBCs. In both types of microchannels, translocation behavior of blood cells was similar (Figure 5-4). The averages of translocation time and current peak was not very different as shown in Figure 5-3(b) and (c). Only 7.63% blood cells showed higher translocation time in nanotextured microchannel compared to plain channel. Blood cells are comparatively smaller in size and created less physical blockage in microchannels. Most of the cells could not come in contact with the surface or side walls of the channels. The nanotexture thus did not had higher affinity towards blood cells and translocation behavior was very similar in both microchannels for majority of the blood cells.

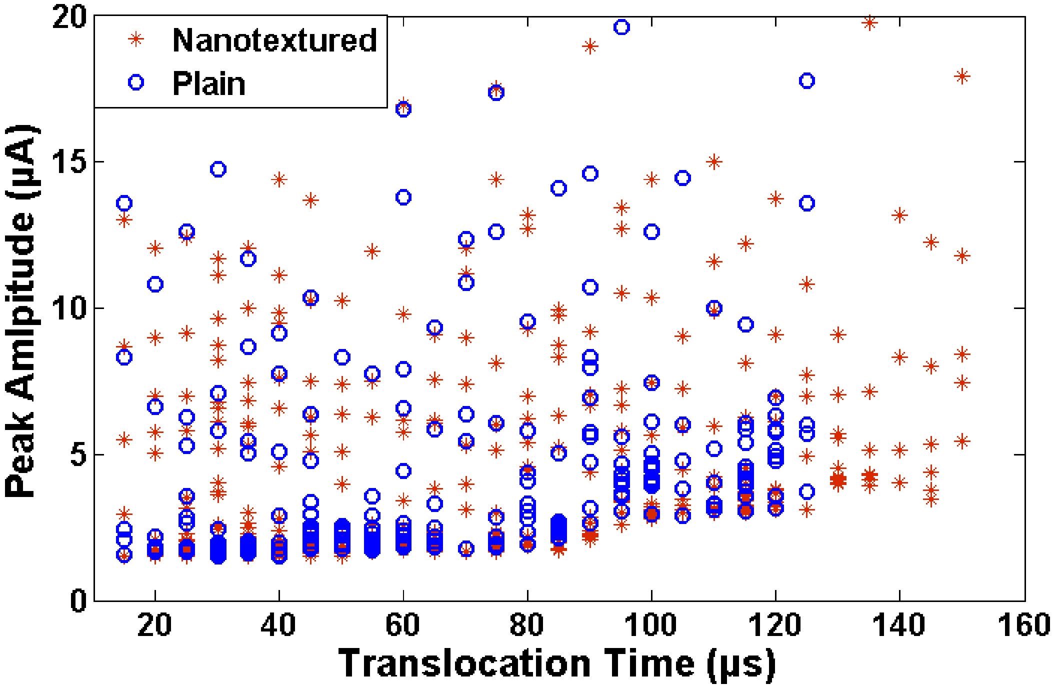

Figure 5-4: Translocation behavior of blood cells in plain and nanotextured microchannels (*n ≈ 200)*

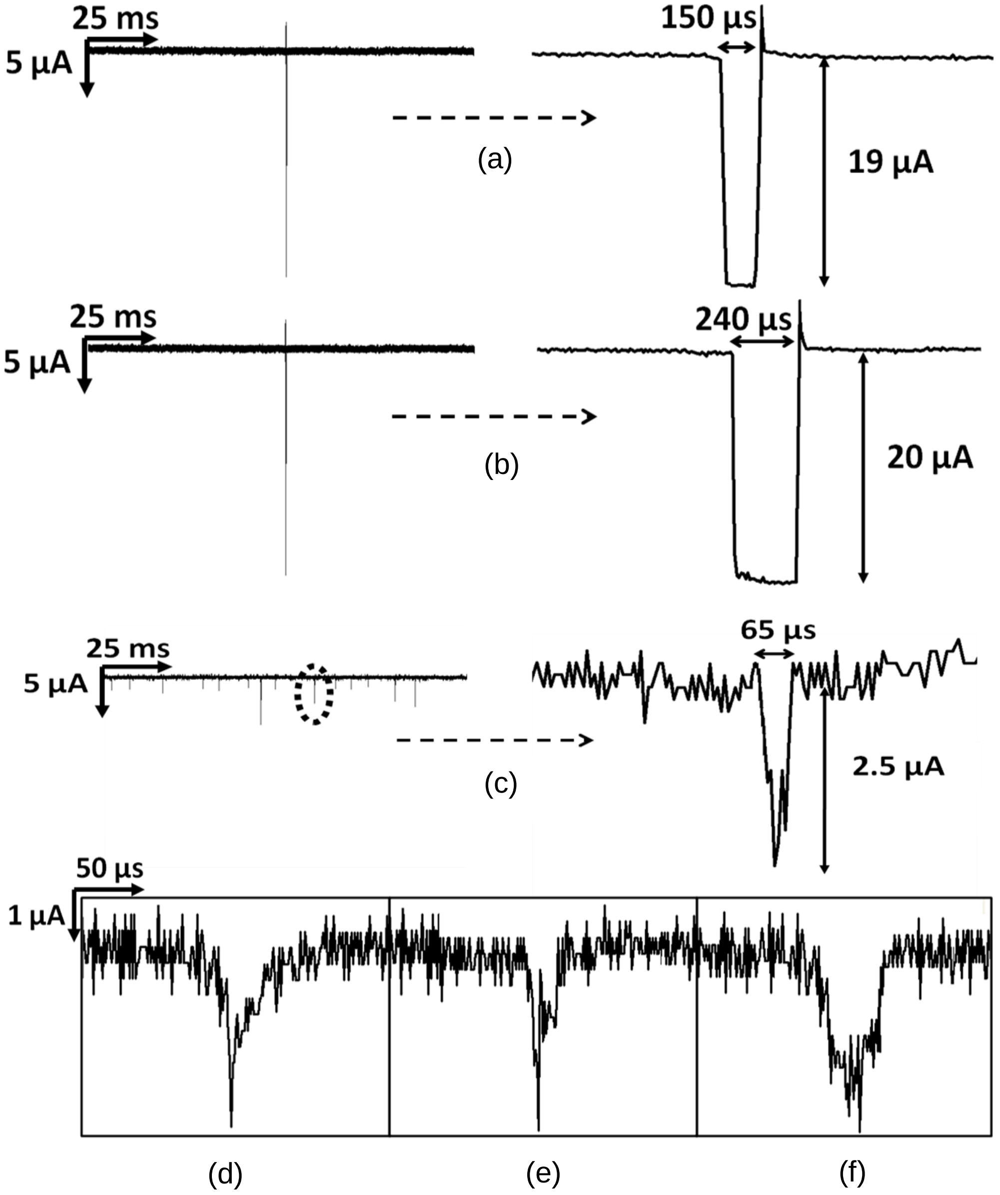

Figure 5-5: Representative electrical pulses of the translocated cells through the microchannels, (a) cancer cell through plain microchannel; (b) **c**ancer cell through nanotextured microchannel; (c) blood through nanotextured PDMS microchannel;, close-up of electrical pulses of some blood cells through (d, e) plain and (f) nanotextured PDMS microchannel. Reprinted with permission [201].

Pulse Shapes of Tumor and Blood Cells

Pulse shapes of cancer and blood cells were observed very closely. Cancer cells generated very smooth pulses (Figure 5-5(A) and (B)). Due to highly elastic nature, pseudopod formation, and interactions with the surface, tumor cells took longer time to pass the channels and ripples of very small magnitude were observed at the bottoms of inverted bell shaped pulses. By closely observing pulse shapes, cluster of cells can be differentiated from single cell.

Smooth pulse is found when only one cancer cell passed through the microchannel at a time. At a sampling rate of 5 µs, in plain and nanotextured channel a pulse consisted of approximately 30 and 48 data points of current, respectively for the tumor cell. Each current value related to a cross-sectional contour sketching the physical dimension of the entire cell [6]. Thus the translocation data can be used to precisely track the three dimensional electrical profile of the tumor cells. From Figure 5-5(a) and (b), it is visible that for cancer cells, pulse width is higher in nanotextured microchannel and also higher number of ripples is being at the bottom of the current pulse. The reason can be the formation of pseudopods in the nanotextured microchannel. Interactions of tumor cells were higher with nanotextured surfaces and cells created higher number of pseudopods [13]. The formation of pseudopod leaded change in shape of the cells and physical blockage got affected. The current rose slightly at the end of every pulse of tumor cells in both types of channels. It was transient and current stabilized in very short period of time. This transient might be due to sudden rush of ions under the applied bias to balance the potential across the channel. For blood cells, some pulses had several spikes which suggested that more than one cells, most probably RBCs, passed together. The diameters of WBCs vary within a range of 5-16 µm. The larger

WBCs showed deeper pulses but the bottom of the pulses had sharper angles (Figure 5-5(c)) as blood cells were stiffer. Figure 5-5(d-f) represents close-up electrical profile of different blood cells. These pulses had several spikes or irregular shapes, in contrast to the pulses of cancer cells. At a sampling rate of 5 µs, in both channels on an average, a pulse contained approximately 13 data points of current for a blood cell. Thus, even for blood cells pulse shape can depict the physical dimension. Statistical analysis of translocation time and peak amplitude for blood and tumor cells were performed and significant difference was found (P-value < 0.01).

Discrimination of Tumor and Blood Cells

The pulse data for blood and renal cancer cells through plain and nanotextured microchannels is plotted in Fig. 5. In plain microchannels, the peak amplitude and translocation time for blood cells were 16.81 µA and 125 µs, respectively. On the other hand, lowest peak amplitude and translocation time for renal cancer cells in the plain microchannels were 10.29 µA and 75 µs, respectively. Thus, there was an overlapping region in translocation behavior for both types of cells in plain microchannels. The calculations showed that 82% tumor cells exhibited distinctive behavior in plain microchannels and 18% of tumor cells were enveloped in the translocation region of blood cells. Similarly, in nanotextured microchannels, the peak amplitude and translocation time for blood cells were 16.95 µA and 150 µs, respectively. On the other hand, lowest peak amplitude and translocation time for renal cancer cells in nanotextured microchannels were 10.73µA and 125 µs, respectively. In nanotextured microchannels, 93% of tumor cells were discriminated from blood cells based on their translocation time and peak amplitude. Translocation time of tumor cells was higher in nanotextured microchannels as discussed above and consequently the discrimination efficiency was improved.

Detection of Tumor Cells from Blood

The aim of the microfluidic device was to detect cancer cells from blood and other bodily fluids. To achieve that target the blood was diluted ten times with 1X PBS. The dilution of blood made the process easier by reducing the density and viscosity of the blood. This diluted blood solution was passed through the microchannels at a flow rate of 16.67 µl/min. We ran experiments in each type of devices for 10 min and repeated it twice. The recorded translocation data of blood cells from both plain and nanotextured devices were used for density plot as shown in Fig. 6(A) and 6(B), respectively. The color variation represents the densities of cells. As the dilution factor decreased from 100 to 10 upper threshold for blood cells were increased slightly due to clumping effect at high concentration. There were some irregular shaped pulses which could be separated from the pulses of renal cancer cells based on their characteristics such as amplitude, width and shape. For plain and nanotextured channels the peak amplitudes were 19.2 µA and 21.04 µA, respectively and the maximum translocation times were 125 µs and 165 µs, respectively. Next, the renal cancer cells were spiked in diluted blood (dilution factor was 10) at a concentration of 100 cells/ml. Now this mixture was used to run the experiments through microchannels for 15 min and repeated twice. The flow rate was kept same as before. Thus the total volume of processed sample was 0.5 ml and the total number of cells was supposed to be passed through the microchannel was 50. Next, the recorded data was used to discriminate tumor cells from blood based on their pulse shape, translocation time and peak amplitude.

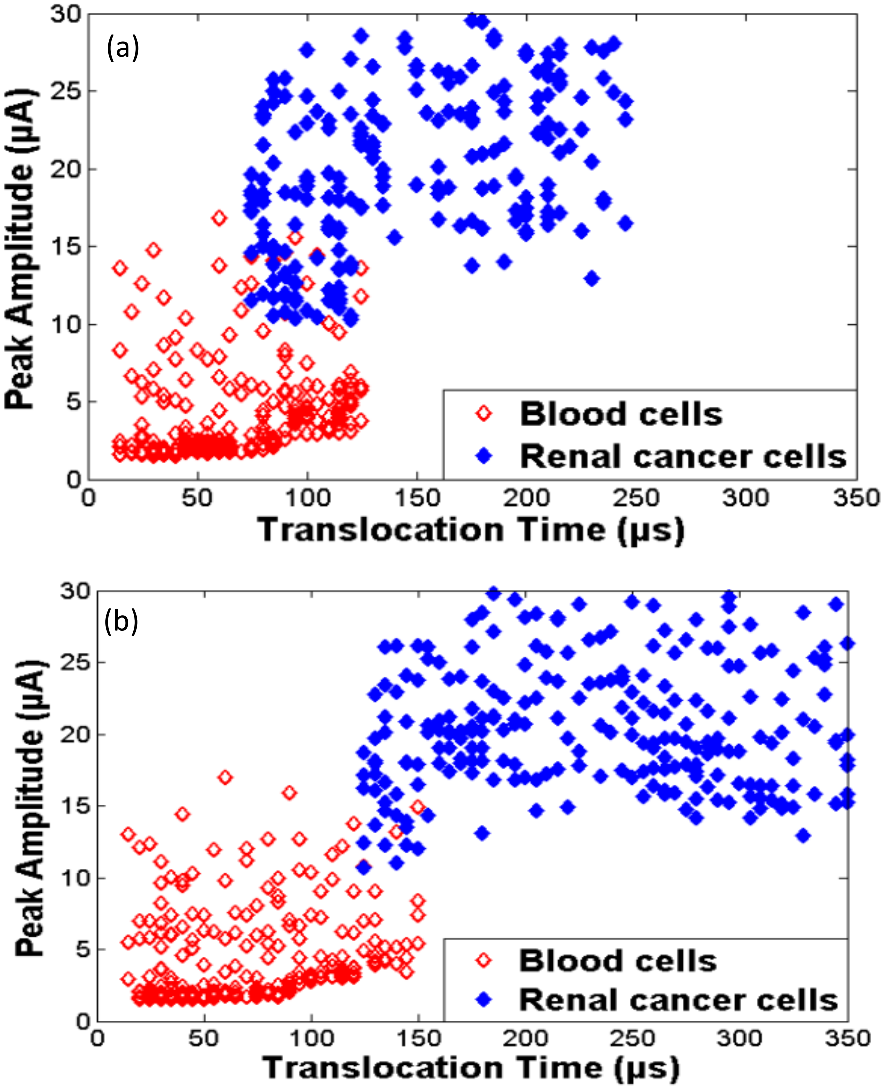

Figure 5-6: Representative translocation data of blood and renal cancer cells through (a) plain and (b) nanotextured microchannels (*n*≈ 200). Reprinted with permission [201].

The density plots of the obtained data are shown in Fig. 6(C) and 6(D) for plain and nanotextured microchannels, respectively. Tumor cells were discriminated in plain microchannels by comparing Fig. 6(A), and 6(C) and Fig. 6(B), and 6(D) were compared for nanotextured microchannels. Typical translocation regions of renal cancer cells, obtained from Fig. 5, are shown by green dotted circle in Fig 6(C) and 6(D). Most of the cells showed familiar peaks in both channels. The majority of the cancer cells exhibited higher translocation time and peak amplitude to distinguish them from blood cells. But for both devices several cells fell in a region which is very adjacent to blood cells. These small percentages (5.56% in plain microchannels and 4.65% in nanotextured microchannels) of cells were discriminated by observing pulse shape very closely. In plain microchannel, cancer cells were detected with an efficiency of 72% while in nanotextured microchannel 86% efficiency was achieved. Enhanced cell-surface interactions in nanotextured channel thus appreciably increased the detection efficiency of tumor cells.

Conclusions

Microfluidic channel was fabricated to detect tumor cells from blood from their translocation behavior. The nanotextured microchannel reduced the translocation time of 50% cancer cells due to enhanced cell-surface interactions. This interesting phenomenon increased the detection efficiency of the device by 14%. The device was very reliable, inexpensive and reusable. This approach can be implemented for quantifying circulating tumor cells. Nanotextured microchannel can also be implemented to differentiate various types and stages of cells.

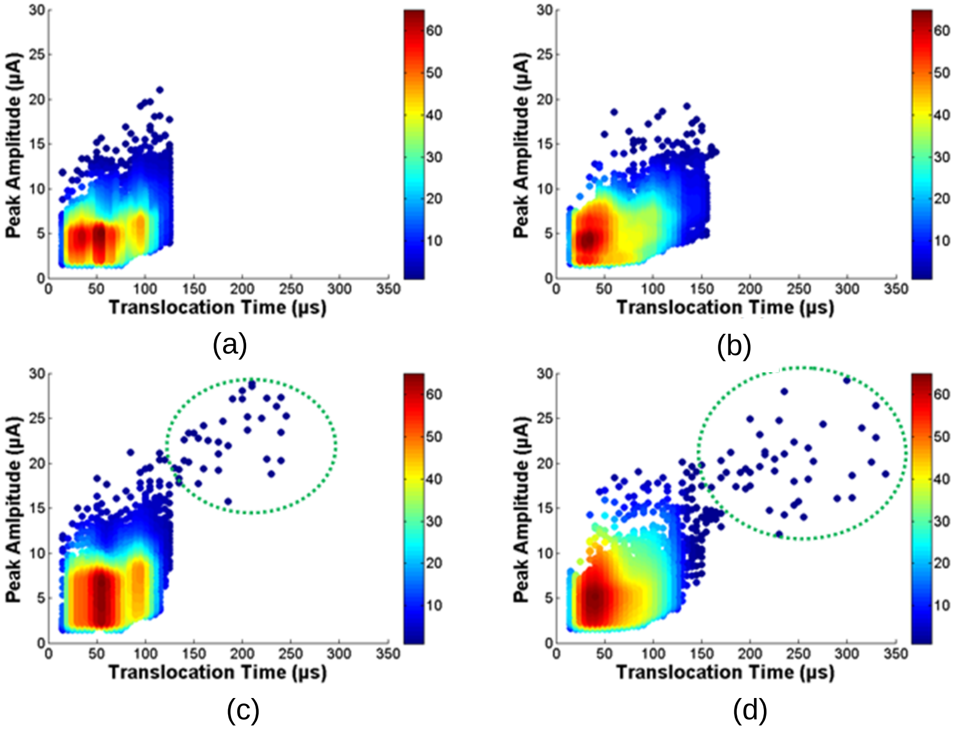

(a)
(b)
(c)
(d)

Figure 5-7: Data plots for blood cells through (a) plain and (b) nanotextured microchannels; data plots for cancer cells spiked in blood through (c) plain and (d) nanotextured microchannels. The typical region of detected cancer cells are enclosed in dotted green circle. Reprinted with permission [201].

Chapter 6

SINGLE BIOCHIP FOR THE DETECTION OF TUMOR CELLS EMPLOYING ELECTRICAL PROFILE AND SURFACE IMMOBILIZED APTAMER

Introduction

In previous two chapters the effect of nanoscale topography on tumor cells has been explained. Nanotextured substrates offer enhanced surface area which amplifies the attachment of aptamers and leaded higher cell capture for target cells. It has also been demonstrated in previous chapter that how translocation profile can discriminate cancer cells from blood. In this chapter a new microfluidic device is introduced to take leverage of both aptamer functionalized nanotextured surface and current measurement techniques for the detection of tumor cells. The device was fabricated using soft lithography and micro reactive ion etching (Micro-RIE) was performed to create nanotextured surface. The device was functionalized with anti-EGFR aptamer and flow velocity was optimized to have high capture efficiency for target cells. Higher flow velocity increased the throughput but deteriorate the cell capture capacity and viability of the cells due to large gradients in shear stress. Cell viability is essential for subsequent genotype and phenotype profiling of the isolated cells. On the other hand, lower flow rate increased the nonspecific binding of unwanted cells. Besides capturing tumor cells, this device was measuring ionic current across microchannels to detect them. The translocation mechanism of cells through the microchannels depended on the size, shape, orientation, and biomechanical properties of the cells and applied fluid pressure. It has been reported that cancer cells are larger in size than blood cells and highly viscoelastic in nature [6, 94, 95]. The transformation of cytoskeleton, while becoming malignant changes the viscoelastic property of tumor cells [183]. However, the cells were suspended in phosphate buffered saline (PBS) and translocated through the device under different fluidic pressure. While passing microchannels, every cell provided distinctive current pulse by creating physical blockage of the channel. Pulse duration and amplitude depended on the physical and mechanical properties of the cells. First of all, hGBM and white blood cells (WBCs) were suspended separately in PBS and injected in the device to observe their translocation characteristics. In this case, all the pulses from inlet and outlet microchannels suggested translocation signatures of individual type of cells. The difference in number of detected cells in two microchannels was indicating the amount of captured cells inside the device. Images of the devices were taken to enumerate the number of captured cells in the cell capture zone and compared with current measurement data. Next, the mixture of hGBM and WBCs (ratio 1:1) was passed at a flow velocity of 1 mm/s. From the current pulses of inlet microchannel 82% hGBM cells discriminated from WBCs. On the other hand, 73% hGBM cells were captured in cell capture region and 20% were detected at outlet microchannel. Thus, 93% of tumor cells were detected using both the cell capture zone and outlet microchannel which is significantly higher compared to the efficiency of only inlet microchannel or cell capture region alone. Finally, the hGBM cells were spiked in rat blood at a concentration of 100 cells/mL and more than 80% cells were detected by the microfluidic device. This microdevice has exploited the benefits of both cell-affinity micro-chromatography and mechanophysical properties based current measurement techniques. This microdevice can be an efficient point-of-care module for the detection of rare tumor cells.

Materials and Methods

Device Fabrication

The schematic diagram of the microfluidic device is shown in Figure 6-1. The inlet and outlet of the devices are connected to the cell capture zone via two microchannels. The current was measured across these microchannels while cells were passing through the device.

The dimensions of the microchannel was 20 µm x 20 µm x 5 µm (width x height x length). The device was fabricated using soft lithography. The pattern was designed in AutoCAD and produced on a glass photomask. The master was fabricated on a silicon wafer. Photoresist SU-8 2010 was spin coated at 1000 rpm for 35 seconds followed by photolithography. Next, PDMS was used to fabricate microfluidic device from the master using same procedure as mentioned in earlier chapters. PDMS was mixed with Sylgard 184 silicone elastomer curing agent (Dow Corning), degassed in a desiccator get rid of the bubbles, poured on the master and heated to cure it. PDMS mold was peeled off the master and fluidic ports were punched using biopsy punch. Next, the device was etched in reactive ion etch series 800 plasma system. The etching was performed using oxygen (O_2) and carbon tetrafluoride (CF_4) for 20 min to create nantoexture. Next, PDMS devices were functionalized with anti-EGFR aptamer as explained earlier, and covered with UV ozone plasma treated glass slides. Eventually, the devices were filled with 1X PBS with 5 mM magnesium chloride (pH 7.5). The master was characterized using Zeiss LSM 5 Pascal Confocal Microscope and KLA-Tencor Alpha-Step IQ profilometer. To evaluate surface topography quantitatively of nanotextured PDMS surfaces a Dimension 5000 AFM was used.

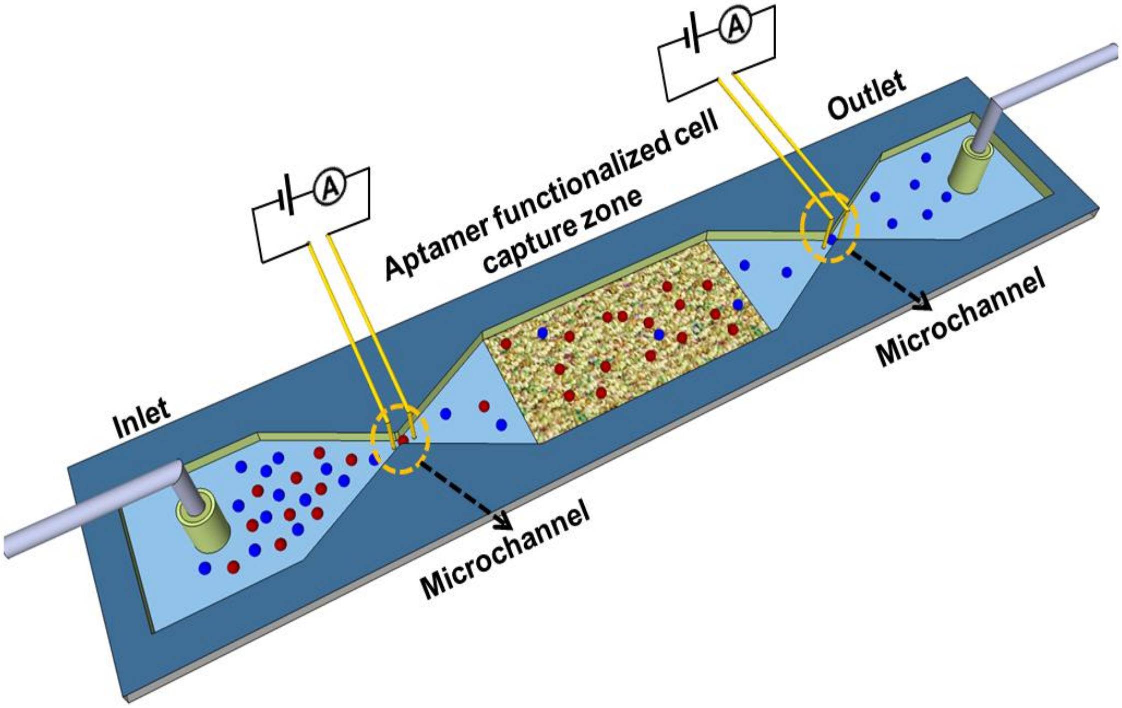

Figure 6-1: Schematic diagram of the microfluidic device consisted inlet, outlet and nanotextured cell capture zone which is functionalized with anti-EGFR aptamers. Current was measured across two microchannels using Ag/AgCl electrodes.

Measurement Setup

The measurement setup was described in previous chapter. The ionic current was measured across the microchannels using Ag/AgCl electrodes. To apply bias voltage and measure current, data acquisition card (National Instruments) was used. A syringe pump (Harvard Apparatus) was used to flow the sample fluid into the device through a tubing adapter. Physical blockage of the channel reduced the conductivity of the channels while cells were passing through microchannels,

Aptamer Preparation

Aptamer preparation was same as explained in chapter 4 [13]. Anti-EGFR RNA aptamer (K_d = 2.4 nM) was immobilized on the substrate through duplex formation using amine-modified capture probe. The sequences of the extended anti-EGFR aptamer was 5'-GGC GCU CCG ACC UUA GUC UCU GUG CCG CUA UAA UGC ACG GAU UUA AUC GCC GUA GAA AAG CAU GUC AAA GCC GGA ACC GUG UAG CAC AGC AGA GAA UUA AAU GCC CGC CAU GAC CAG-3' [13].

Attachment of Anti-EGFR Aptamer on PDMS Surfaces

The aptamer attachment protocol was same as mentioned in chapter 4 [13]. PDMS devices were treated in UV Ozone plasma for 30 min followed by piranha solution dip, rinsing in DI water and dried in nitrogen flow. Then immersed in 3% (v/v) of (3-aminopropyl)triethoxysilane (APTES) in methanol for 30 min at room temperature; cured 30 min at 120 °C. Next, devices were treated with dimethylformamide (DMF) for 5 hours at 45 °C. After every chemical treatment, devices were rinsed in DI water and dried in nitrogen. A 30 µmol/L concentration of capture DNA (which had a 5' amine group) was prepared with 1% *N,N*-Diisopropylethylamine (DIPEA) and devices were incubated in DNA solution overnight in a humid chamber at 37 °C. Then the devices were washed with methanol and diethylpyrocarbonate (DEPC) treated DI water. Next, samples were immersed in 150 mmol/L DIPEA in DMF and 50 mmol/L 6-amino-1-hexanol for 5 hours and again washed in ethanol, DMF, and DEPC-treated DI water. Then a glass chamber was properly washed with RNase free and DEPC treated DI water and PDMS samples were placed in it. Next, aptamer (1 µmol/L) dissolved in 1X annealing buffer [10 mmol/L Tris (pH 8.0), 1 mmol/L EDTA (pH 8.0), 1 mmol/L NaCl] was placed on each sample. After incubating 2 hours at 37 °C, samples were washed with 1X annealing buffer and DEPC-treated DI water for 5 minutes. Finally, devices were kept in 1X PBS (pH 7.5) with 5 mmol/L magnesium chloride solution.

Culture of Human Glioblastoma (hGBM) Cells and Collection of Rat blood

The hGBM cells were cultured using the same protocol described in chapter 4 [13]. Chemically defined, serum-free Dulbecco's Modified Eagle's Medium (DMEM)/F-12 medium supplemented with 20 ng/mL mouse EGF (from Peprotech, Rocky Hill, NJ), 1X B27 supplement (Invitrogen, Carlsbad, CA), 1 insulintransferrin-selenium (Invitrogen), and penicillin:streptomycin 100 U/mL:100 µg/mL (HyClone, Wilmington, DE) was used to culture these cells. Lentivirus expressing *mcherry* fluorescent protein was used to transducer the hGBM cells. The blood samples were collected from tail of a rat by restraining the animal [156]. The blood was collected in tubes with K2-EDTA as anticoagulant. Lysis buffer (eBioscience, CA, USA) was used to isolate white blood cells (WBCs) from red blood cells (RBCs) [7, 13]. 10 mL of 1X lysis buffer was added to 1 mL of whole blood and incubated for 10 min. Then 20-30 mL of 1X PBS was added to stop the reaction. This solution was centrifuged at 300-400g and cells were collected from the bottom of the tube as pellet. This pellet was re-suspended in the 1X PBS and washed several times to remove blood platelets. Then the cell density was calculated and again suspended in 1X PBS to have desired cell concentration.

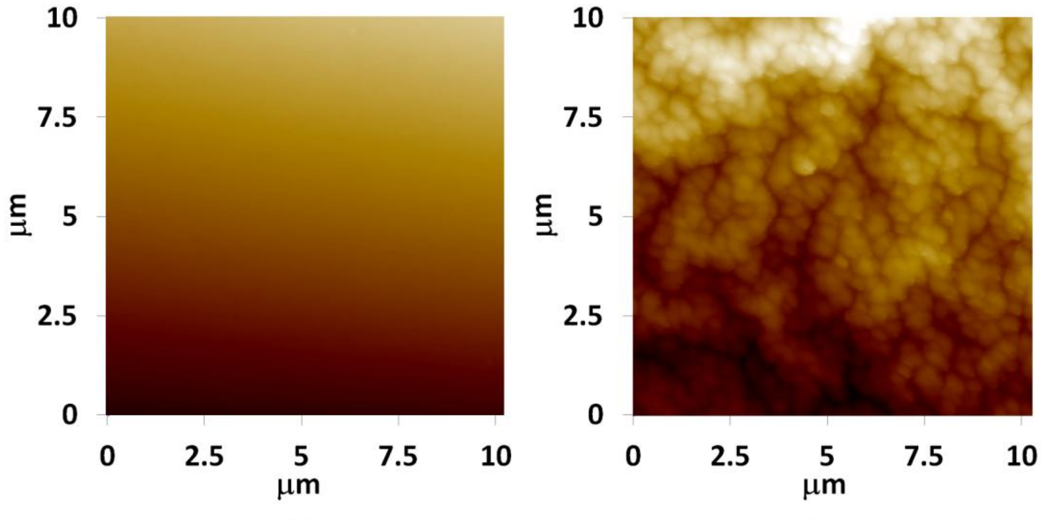

(a)

(b)

Figure 6-2: AFM micrographs of (a) plain; and (b) nanotextured PDMS surfaces.

Current Measurement and Capture of Cells in Microfluidic Device

The cell suspension was injected through the aptamer functionalized microfluidic devices at different velocities. The current was recorded across two microchannels during cells were passing through. Then 1X PBS was pushed at same flow rate to wash the device and eliminate nonspecifically bound cells. Current was recorded while washing the device to detect loosely bound cells. From the solution, cells were detected by analyzing the data recorded from ionic current measurement. Also the images of the cell capture zone were taken with microscope and analyzed by *Image J* to count the number of captured cells. First of all, hGBM and WBCs were suspended separately in 1X PBS. Next, these cells were mixed at 1:1 ratio and injected into the device. Finally, rat blood was diluted 10 times in 1X PBS to reduce the viscosity and hGBM cells were spiked at a concentration of 100 cell/mL and passed through the devices. For the cell mixture, the devices were observed in fluorescence microscope to discriminate between cancer and blood cells.

Results and Discussion

Topography of Nanotextured Surfaces

Using AFM, the measured average roughness of nanotextured surfaces was approximately 500 nm. The AFM images of plain and nanotextured surfaces are shown in Figure 6-2.

Device Assembly

The microfluidic device had two microchannels that was assembled as described in the Materials and Methods section. Dimensions of the microchannels were small enough to ensure multiple tumor cells cannot pass through simultaneously. Higher flow rates allowed high throughput. But the measurement system could not record translocation events of some cells. Again high flow rate increased the shear stress on the cells inside the channel and reduced the probability of a cell to be captured in aptamer functionalized zone. For the current measurement system frequency of the electrical sampling was optimized to reduce noise and enhance stability [6, 7]. The current sampling rate was 5 µs (0.20 MHz) and applied bias voltage was 5 volts.

Determinationo of Cell Capture Efficiency

EGFR was overexpressed on cell membrane of the hGBM cells and anti-EGFR aptamer had affinity for this type of cells [13]. Thus, anti-EGFR aptamer functionalized nanotextured surfaces was employed to capture hGBM cells. The efficiency to capture cells depended on the flow velocity. Higher flow rate increased the shear stress on cell membranes and reduced the possibility of a cell to be captured. A flow rate around 2 mm/s can be used to capture tumor cells with high selectivity [184]. Here the flow velocity was varied from 1 to 5 mm/s for determining cell capture probability of the aptamer functionalized nanotextured PDMS.

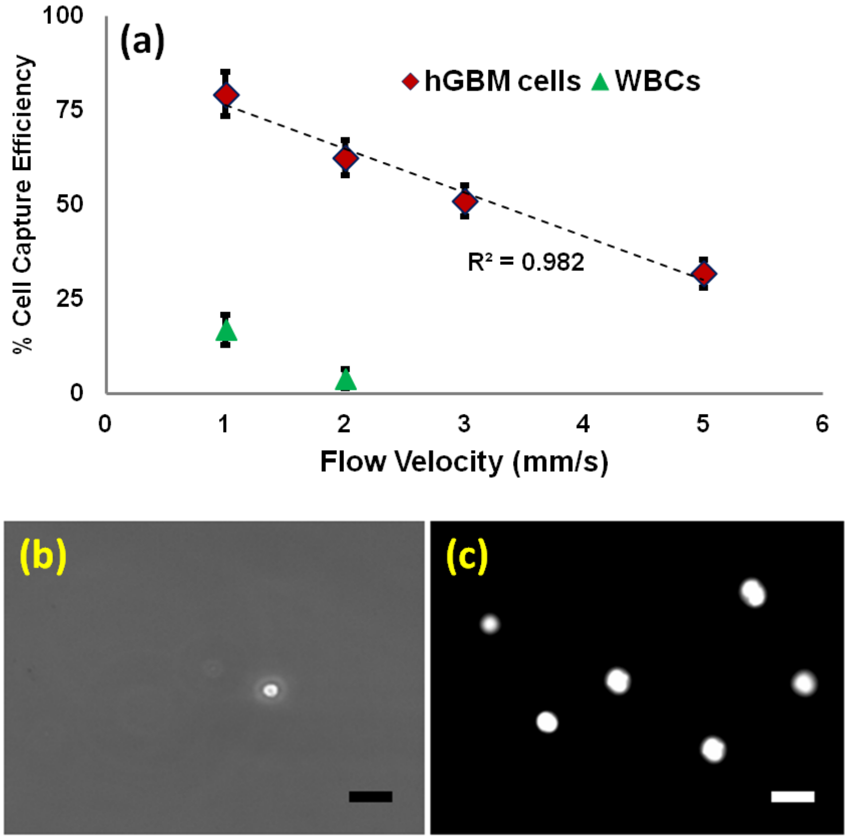

Figure 6-3: Cell capture efficiencies in anti-EGFR aptamer functionalized nanotextured PDMS channels at different flow velocities (a) cell capture efficiencies for hGBM and WBCs are shown using blue and green marker; captured cells; (b) hGBM cells and (c) WBCs; 100 µm scale bar is for both (b) and (c).

RBCs and most of the WBCS are generally smaller compared to tumor cells, some WBCs have diameter comparable to tumor cells [6, 7, 184]. Again, hGBM cells have overexpressed EGFR in their cell membrane. All these properties elevated the cell capture probability of hGBM cells over blood cells in aptamer modified nanotextured microfluidic channel. First of all, hGBM and WBCs were injected in the device separately to calculate cell capture efficiency. The capture efficiency was defined as the ratio of captured cells and the total number of cells passed through the channel. The capture efficiencies of hGBM and WBCs at different flow velocities are shown in Figure 6-3 (a). As the flow velocity increased from 1 mm/s to 5 mm/s the capture efficiency for hGBM cells was dropped from 79.37 ± 5.97% to 31.79 ± 3.75%. To examine the viability of captured hGBM cells at 1 mm/s flow velocity, trypan blue exclusion dye (0.4%) was used and more than 90% cells were viable. On the other hand, for WBCs capture efficiency was decreased from 16.89 ± 4.02% to 3.93 ± 2.59% for the flow velocity of 1 mm/s and 2 mm/s respectively. Figure 6-3(b) and (c) are showing the images of captured hGBM and WBCs, respectively at a flow velocity of 1 mm/s.

Cell capture efficiency of aptamer functionalized surfaces basically depends on the available number of anti-EGFR aptamers on the surface, the density of EGFR on cell membrane and the affinity between EGFR and its complimentary aptamer. Nanoscale topography on the surface can enhance the number of anti-EGFR aptamer molecules [13]. Higher number of aptamers increased the density of target cells and also reduced the binding of nonspecific cells. Again, nanotextured can create minor turbulence in the fluid flow which enhanced the possibility of aptamer-cell interactions. The phenomenon, mentioned above cansignificantly augmented the adherent of cells inside the channel. For the optimal condition aptamer density is usually very high on a surface, roughly be estimated 20-25 per 100 nm^2, which is almost twenty times higher than the density of EGFR on the cell membrane of hGBM cells [13]. The single aptamer-EGFR binding force can be approximated around 8 x 10^{-6} dynes [185]. Total binding force between a cell and aptamer grafted surface depends on the EGFR density on cell membrane and total contact area between cell and surface. The size and orientation of cells can be vital for cell-surface bonding. The cells with larger diameter are more likely to come in contact with the aptamer grafted surface and become flat to have rigid bonding. Conclusively higher density of EGFR in cell membrane and larger contact area can provide greater binding force (F_B). In addition the flow velocity generates shear stress (τ) as well as force (F_T) on cell membrane and tries to wash it off shown in Figure 6-4. The following equation can be used to calculate the stress [186],

$$\tau = \frac{6\sigma Q}{h^2 w} \dots\dots\dots (6-1)$$

Where, σ is the dynamic viscosity of the fluid, Q is the volumetric flow rate; h and w are height and width of the channel, respectively. Resultant of these two forces (F_R) have significant impact on cell capture probability [184].

Electrical Measurement of Cells

Translocation behavior of blood and tumor cells through nanotextured microchannel has been characterized as explained in chapter 5. It was deduced that tumor cells can be differentiated from blood cells according to their pulse characteristics such as width, amplitude and shape. In this microfluidic device the current was measured across two microchannels connected to inlet and outlet. First of all, the hGBM cells and WBCs were suspended in 1X PBS at a concentration of 1000 cells/mL separately and injected through the device at different flow velocities while current was measuring across two microchannels. The hGBM cells showed distinctively different pulse characteristics from WBCs. The amplitude and pulse width was higher for majority of the tumor cells compared to blood cells. Though some hGBM and WBCs had indistinguishable translocation profiles, more than 80% tumor cells revealed distinctive behavior at flow velocity of 1 mm/s and 2 mm/s. The average peak amplitude for hGBM and WBCs at 1 mm/s flow velocity was 19.35±3.62 and 7.96±2.83, respectively and translocation time was 235.16±53.47and 77.15±38.59, respectively. For 2 mm/s flow velocity the peak amplitude did not vary significantly but the translocation time for hGBM and WBCs were 171.75±43.44 and 64.88±29.26, respectively. The translocation profile of a cell depended on its mechanical and physical properties such as size, shape and elastic modulus, and also on the orientation. The pulse width depended on the time a cell takes to pass the microchannel and cells with higher length had greater pulse width. The peak amplitude depended on the cross sectional area of the channel which was blocked by cells [187]. Thus orientation of a cell also had impact in pulse characteristics. Based on the orientation, translocation profile of single cell can vary to some extent. Current profile also depended on elasticity of a cell [7]**.** Higher elasticity allowed a cell to pass easily and provided steady uniform pulse. Average size of a WBC is mostly smaller than a tumor cells. Again the tumor cells are highly elastic and can squeeze through small channels quiet easily [94, 95, 156]. The shapes of tumor cells are also different from WBCs. The cumulative effect of all these aforementioned factors made the translocation profiles of hGBM cells different from WBCs as shown in Figure 6-5(a).

The flow velocity also influenced the translocation behavior of cells. At higher velocity the cells moved faster and had less chance to interact with the channel surfaces. Due to high pressure, cells can be deformed and leaded modifications in the pulse characteristics.

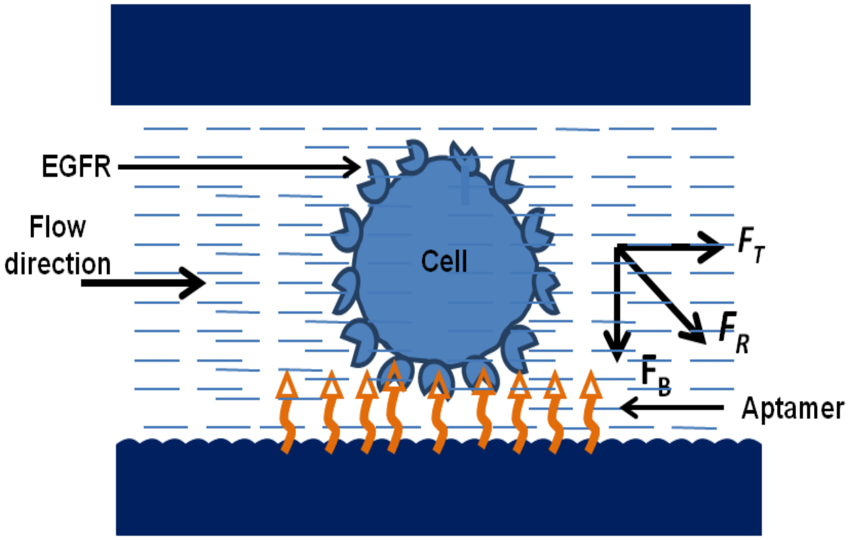

Figure 6-4: Forces working on EGFR overexpressed tumor cell in aptamer functionalized nanotextured PDMS channel.

Pulse shapes can also be observed closely to differentiate cell types. Due to deformable nature and interactions with the surface pulse shape of cancer cells were different than blood cells shown in Figure 6(b) and (c). At a sampling rate of 5 µs and flow velocity of 1 mm/s, on average, a tumor cell and WBC consisted of 47 and 15 data points, respectively. From these data physical dimension of the whole cell can be depicted. The pulse triggered by a cluster of cells can also be identified from pulse shapes. Generally a pulse from single cell is uniform in contrast to cell clusters, where pulses have several spikes and irregular shapes. Translocation time and peak amplitude for blood and tumor cells were found significantly different from statistical analysis (*P*-value < 0.01).

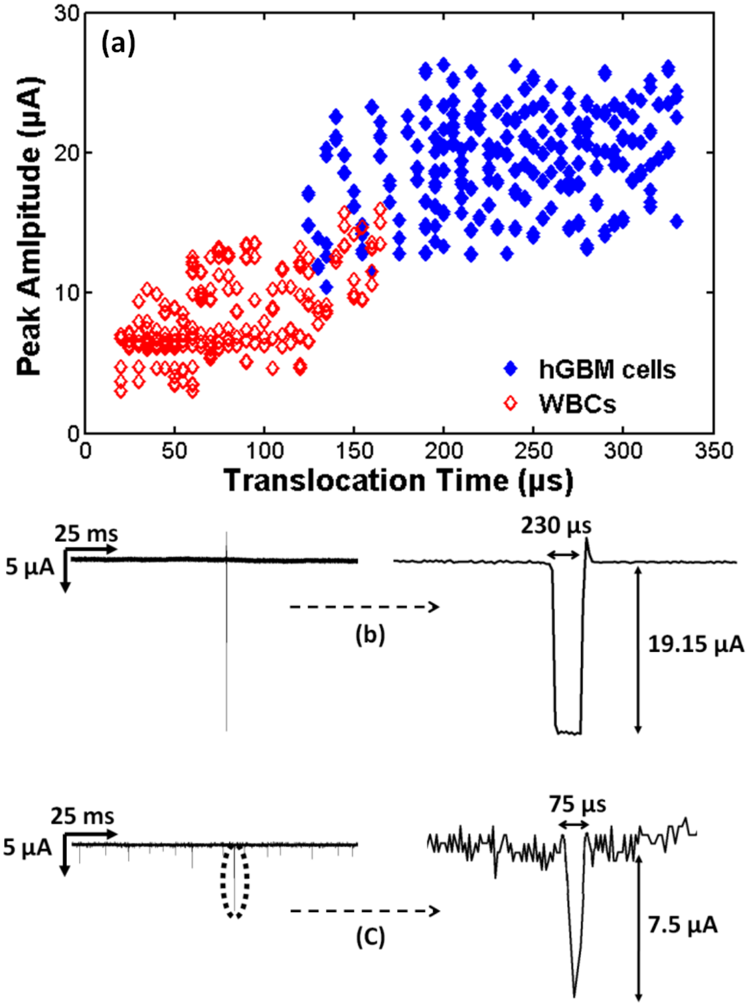

Figure 6-5: Electrical data and translocation behavior of hGBM and WBCs through microchannels, (a) distribution of the pulses for two types of cells where average translocation time and peak amplitude of current both are higher for hGBM cells; electrical profile of the translocated cells through the microchannel (b) hGBM cell ; (c) WBC.

Total Detection Efficiency

Cancer cells have different chemical, physical and biomechanical properties compared to blood cells. But properties of cells may vary within a large range depending on types and state of cancer, also from patient to patient. Thus, this device was aimed to take the advantages of all of these properties of tumor cells to detect them. At a flow velocity of 1 mm/s, due to the overexpression of EGFR this device was able to capture 79.37 ± 5.97% tumor cells. While remaining cells were passing through microchannel to the outlet, 19.16 ± 6.96% of total tumor cells were detected from current measurement data of outlet channel. The detection efficiency was defined as the ratio of detected cells at outlet microchannel and the total number of cells passed through the device. Thus, overall detection efficiency of the microfluidic device was 98.53 ± 0.99%.

Isolation of hGBM and WBCs

It has been shown that higher flow rate increased the throughput but reduced the nonspecific binding of cells. At the same time possibility to capture cancer cells was less at higher flow velocity. At early stages of cancer the number of tumor cells in blood is exceedingly low and it is desired to have highly sensitive device to detect as much cells as possible. To isolate hGBM cells from WBCs, the cell mixture was suspended in 1X PBS at a ratio of 1:1 (2000 cell/mL) and passed through the aptamer functionalized microfluidic devices at 1 mm/s flow velocity while current was measured across two microchannels. After 30 min the device was washed using 1X PBS and observed in fluorescent microscope. The experiment was repeated twice. The concentration of captured tumor cells and WBCs were calculated from images using *Image J* and enrichment of tumor cells inside the device was calculated.

Previously the hGBM and WBCs were pushed separately in the device. That's why all the pulses obtained from current measurement data were representing one specific type of cells. But current pulses needed to be evaluated precisely to discriminate tumor cells from cell mixture. Translocation data acquired from first microchannel of the device, shown in Figure 6-6(a) was analyzed and 82.08±4.91% of the tumor cells was detected. Next, the cell capture efficiency was determined from the images as shown in Figure 6-6(b) and (c) and it was 73.36±4.61%. Optical image in Figure 6-6(b) is showing all the captured cells and 6-6(c) is fluorescent image where only the hGBM cell is visible. Comparing these images single WBC was identified which is circled with blue in Figure 6-6(b).

From the data recorded for outlet microchannel, 20±0.39% of total tumor cells was differentiated successfully. Translocation data from outlet microchannel is also shown in Figure 6-6(a). The number of detected cells in outlet microchannel was lower than the inlet microchannel as some cells were captured in cell capture zone. The cell capture and current measurement techniques together offered 93.36±4.22% efficiency to discriminate tumor cells from WBCs which was remarkably higher compared to only current measurement or aptamer functionalized nanotextured method alone. The cell capture area selectively isolated the tumor cells and WBCs at a ratio of 4.5:1.

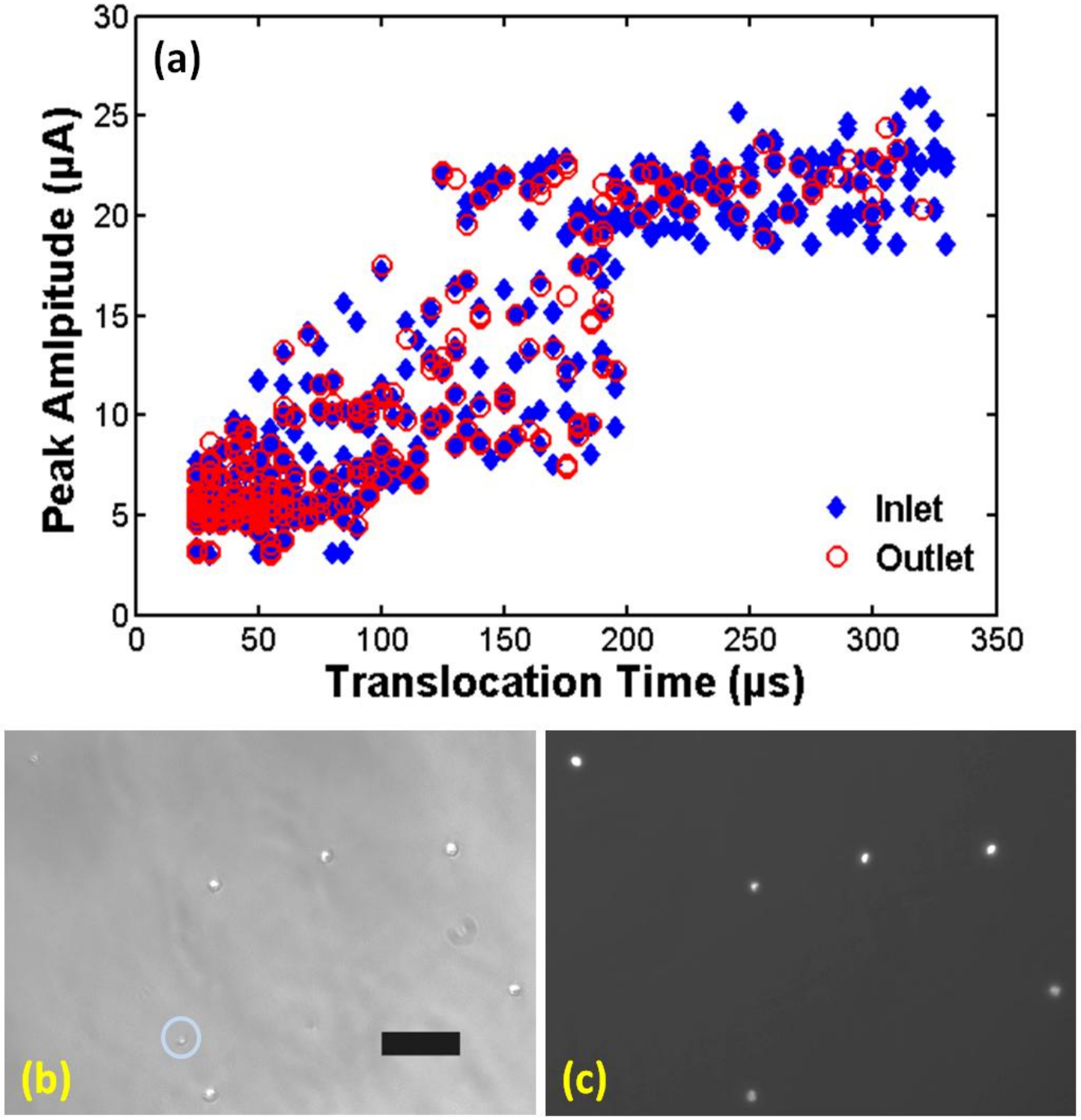

Figure 6-6: Data for the mixture of hGBM and WBCs at a ratio of 1:1 (a) Electrical data through microchannels; captured cells on aptamer functionalized microdevice (b) optical image where both types of cells are present (a WBC is marked in blue); (c) fluorescent image where only hGBM cells are visible; 100 μm scale bar is for both (b) and (c).

Detection of Tumor Cells from Blood

Eventually, tumor cells were spiked in rat blood and detected using the microfluidic device. The hGBM cells were spiked in diluted blood at a concentration of 100 cells/mL as mentioned in materials and method section. After running the experiment for half an hour, images of the device were captured and current measurement data was analyzed from both microchannels. Even at this low concentration of tumor cells the inlet microchannel was able to detect more than 70% cells from the solution shown in Figure 6-7(a). In this figure different colors are used to indicate the concentration of cells and green circle is indicating the detected tumor cells. Again, 16.67±3.93% of total tumor cells was discriminated from blood cells at the outlet microchannel using the translocation behavior shown in Figure 6-7(b). Next, from the images it was found that 67.24±8.65% tumor cells were captured in the aptamer modified nanotextured region shown in Figure 6-7(c) and (d). Optical image in Figure 6-7(c) is showing all the captured cells in the device and Figure 6-7(d) is the fluorescent image where only the hGBM cell is visible which is marked with blue in Figure 6-7(c). Overall efficiency of the device to detect tumor cells was 83.91% and substantially higher compared to the detection efficiency only from the translocation behavior of the inlet channel or aptamer functionalized nanotextured cell capture area. Thus, this microfluidic device can be implemented as an efficient point-of-care device todetect cancer at early stage.

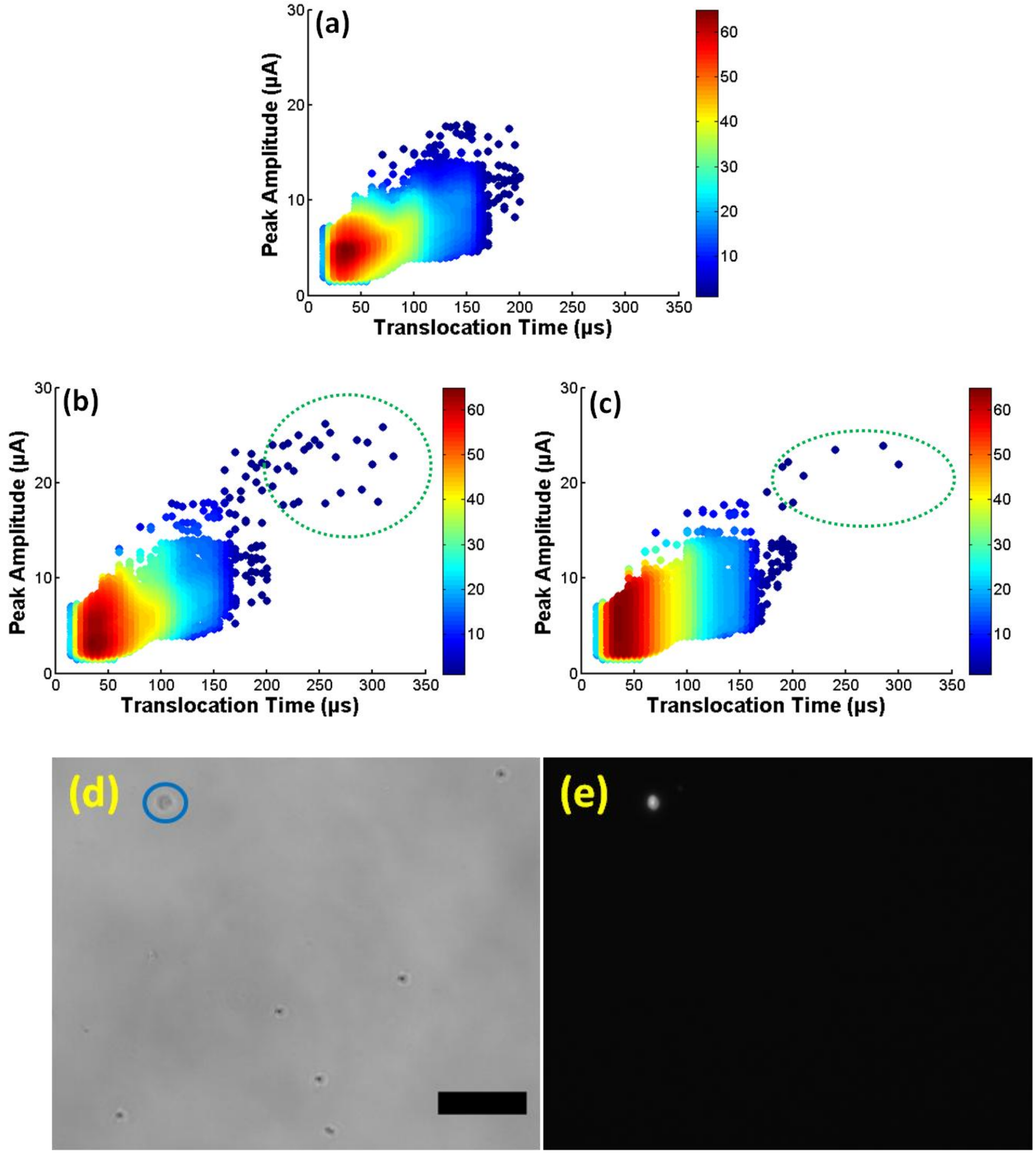

Figure 6-7: Data for the mixture of hGBM and blood, electrical data through microchannels (a) inlet and (b) outlet (detected cancer cells are enclosed in green region); captured cells on aptamer functionalized microdevice (c) optical image where both types of cells are present (a hGBM cell is marked in blue); (d) fluorescent image where only hGBM cells are visible; 100 µm scale bar is for both (b) and (c).

Conclusions

A microfluidic device is implemented to detect cancer cells from blood. Multistage detection scheme was designed by surface grafted aptamers in nanotextured PDMS and by measuring translocation behavior. The flow rate was optimized to have higher detection efficiency. This device provided significantly higher efficiency compared to only current measurement or aptamer functionalized nanotextured surface technique. More than 80% of hGBM cells were detected from blood sample. A general drawback of multistage detection method is the loss of rare cells at different stages. But this device did not have this problem as all the cells passed through the cell capture region and microchannel in series manner. The aptamer based separation depends on the overexpression of target protein on cell membrane which may vary within a large range. Again mechanophysical properties of tumor cells overlap with blood cells which limited the efficiency of size based isolation methods. Thus, association of these two approaches in a simple lab-on-chip yield high efficiency. This inexpensive device can be used in parallel to increase the throughput. The efficiency of the device can be increased further by implementing novel design for cell capture zone.

Chapter 7

NANOTEXTUERD BARE COVERSLIP GLASS TO ENHANCE THE GROWTH OF PC12 CELLS

Introduction

The number of traumatic injuries to the brain and spinal cord are over 1.5 million every year only in the United States [188]. Controlled outgrowth of neurite, guided by the chemical and physical cues is essential in regenerative medicine for the treatments of nerve injuries [189-192]. Only few effective treatments are available for CNS injuries because the CNS is refractory to axonal regeneration and relatively inaccessible to many pharmacological treatments. Thorough functional recovery from CNS injury would require improved neuronal survival, regeneration of axons, and their reconnection to appropriate targets [193]. To promote the regeneration of axons, inhibitory molecules can be destroyed to create a growth-permissive environment or the response of axons contacting these inhibitors can be decreased [194]. Contemporary treatments used for CNS injury include surgical, thermal, and pharmacological interventions largely targeted at decreasing neuronal loss and the inflammatory response initiated after acute injury. Stem cell therapies provide fascinating alternative for treating chronic CNS injuries and improving nervous system regeneration [188]. However, the particular cells used in the pre-clinical studies are oligodendrocyte precursors [195]. Pre-clinical studies using undifferentiated stem cells indicate that these cells do not form neurons in the CNS and may lead to the development of tumors [196, 197]. Considering the complexity of CNS injuries and recovery responses, the development of better treatment strategies for spinal cord injuries, a combinatorial strategy that triggers axon regeneration and appropriate connectivity should also be explored [198]. Recent progress in nanoengineering provided exciting alternatives for designing biocompatible micro- and nanovectors for controlled release of therapeutic and diagnostic agents to targeted CNS cells. Guided neurite growth is also possible by nanopattern than the neurite itself [189]. Nanopatterned substrates can minimize the complication of confinement and offer efficient model to investigate the underlying mechanisms of topological neurite guidance. A recent study has showed that nano-topological features led to aligned neurite outgrowth in PC12 cells [189]. This study suggested that the upregulation and downregualtion of specific biomolecules in nanopatterned regions induced the neurite growth.

Several studies have already reported that cell capture, growth, adhesion, translocation behavior, and orientation are influenced by nanoscale topography of the substrates [13, 119, 159, 160, 199-201]. Also in the areas of tissue engineering, some studies have shown that nanostructured scaffolds can significantly increase densities of certain cells [161, 175]. Nanotopographic surfaces have various impacts on cell functions [175, 176, 178-181, 202]. These surfaces offer biomimetic cell-stimulating cue, as cells have to contact with nanotextured interfaces in vivo. Basement membranes of most tissues are composed of complex mixtures of nanoscale structures [176]. Cells sense nanotopography and react by bridging or conforming in a selective manner. Also nanoscale patterning significantly impact on the organization and type of focal adhesions either by disrupting their formation or by inducing specific integrin recruitment [175, 176]. As integrins are directly linked to the nuclei, due to the cellular response to topography gene expression also gets affected. Upon adhesion to a substrate the cell probes its environment and moves using nanoscale processes like filopodia and lamellipodia. Filopodia probes the environment and their ends serve as anchor points for cell movement [175, 176]. Cells also interact with the topography by deforming membranes and cause modification on the functioning of cell surface. Thus, the key feature of nanotextured surface is it activates receptors on cell surface and enhances the cell-surface interactions to modulate the cell growth. In this study, the effect of nanotexture surface was investigated for the growth of PC12 cells. The cells were cultured on bare coverslip glasses. The surfaces were not coated with ECM component because it originates the argument whether the growth is induced by the topology or due to the enhanced concentration of coated materials on the nanotexture surface. Thus, the effect of nanoscale random topology as physical cue for the growth of PC12 was observed exclusively. Here micro reactive ion etching (micro-RIE) was performed to create nanotexture on glass coverslip and that elevated the cell growth substantially. Therefore, nanotexture surfaces can be implemented for faster growth of neuronal cells to have quick recovery of nerve injuries. Nanotexture surface might also be incorporated for controlled neurite outgrowth.

Materials and Methods

Preparation of Nanotextured glass Substrates

The cover glasses were cleaned in isopropyl alcohol (IPA), rinsed in deionized (DI) water and dried in nitrogen. A reactive ion etch (RIE) series 800 plasma system was used to create nanotexture on this substrates. The etching was performed using the mixture of oxygen (O_2) and carbon tetrafluoride (CF_4) for 45 min (10 sccm O_2 and

CF_4, 250 Watt, 250 mTorr). After etching, each substrate was cleaned in sonicated IPA followed by cleaning in piranha solution (H_2O_2:H_2SO_4, 1:3) and DI water.

Surface Characterization using AFM

Surface topography of the coverslip glasses was evaluated qualitatively, and quantitatively by a Dimension 5000 atomic force microscopy (AFM). The root mean square surface roughness was measured for both plain and nanotextured coverslip glasses. Micrographs of the samples were captured in the ambient air with 15% to 20% humidity at a tapping frequency of approximately 300 kHz. The field measured was 5 µm x 5 µm at a scan rate of 1 Hz with 256 scanning lines.

SEM and Elemental Composition of the Samples

An SEM/EDS Leo Supra 55 VP was used to examined surface topography. The sample surfaces were coated with 5 nm of gold to avoid surface charging before taking SEM images. The micrographs were taken at 12 kV of accelerating voltage and 30 µm aperture. Next, energy dispersive x-ray spectroscopy (EDS) was used to identify and quantify the surface elements of plain and nanotextured coverslips. An EDS detector (EDAX, Genesis) was attached to the scanning electron microscope (SEM). The SEM was focused at a 15 mm working distance with 20 kV accelerating voltage and data were recorded followed by mapping analysis.

Contact Angle Measurements

Contact angles for plain and nanotextured coverslips were measured using a contact angle goniometer (NRL-100; Rame-Hart, Washington, DC). A 10 µl water drop was placed on the samples and the contact angle of the water-substrate interface was recorded by visual observation through a microscope. On average, 5 measurements were taken for each run.

Culture and Treatment

PC12 rat pheochromocytoma cells (ATCC, Manassas, VA) were were routinely cultured at 37°C in 5% CO2 in F-12 Nutrient Mixture with Kaighn's modification (F12K) containing 2.5% fetal bovine serum and 15% horse serum (both from Invitrogen, Carlsbad, CA). For experiments, cells were plated at 5,000 cells/cm2 on culture plate membranes, normal, and nano-textured glass cover-slips in 24-well tissue culture plates and allowed to grow for 48 hours or more until 65% confluence were observed. All the experiments were performed in triplicates. For the treatment, after 48 hours of cell growth and attachment, cultures were washed twice with PBS and placed into serum-free F-12K with or without 100 ng/ml nerve growth factor β subunit (β-NGF, Sigma-Aldrich, St. Louis, MO), added daily for 96 hours. Cultures were fixed in 4.0% paraformaldehyde and 2.0% gluteraldehyde in PBS and washed twice in PBS. For cell density assessment, bright-field images (4-5 images/condition/experiment) were captured through a 10X objective on a Vee Gee Vanguard 1491 INi inverted microscope. Nuclear morphology was assessed using confocal images captured through a 64X objective from cells labeled with 4',6-diamidino-2-phenylindole (DAPI, Ex = 405 nm, Em = 450/35 nm), following treatment containing culture plate membranes, normal, and nano-textured glass cover-slips in 24-well tissue culture plates as growth surfaces.

Topography of Nanotextured Substrates

Micro-RIE provided reasonably uniform nanotextured coverslip glasses. The measured average roughness of plain and nanotextured coverslips were 11.34±2.25 nm and 105.06±17.87 nm, respectively. The AFM micrographs of plain and nanotextured surfaces are shown in Figure 7-1.

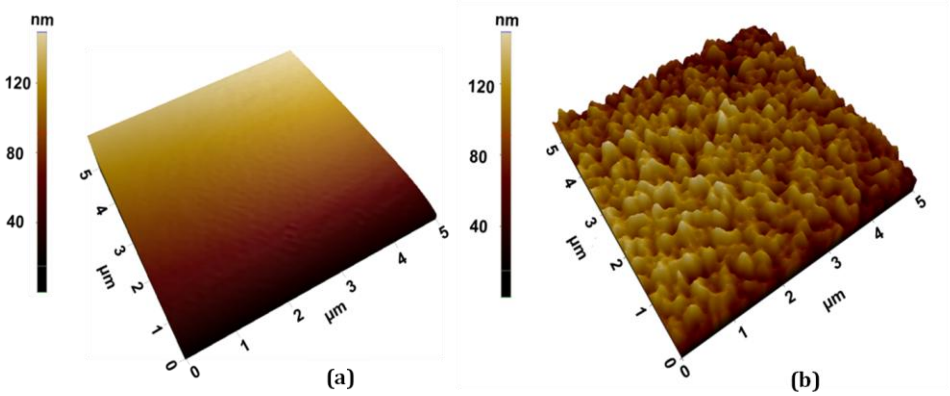

Figure 7-1: AFM micrographs of the (a) plain and (b) nanotextured PDMS surfaces.

Elemental Analysis and Compositional Mapping

The SEM micrograph of nanotextured coverslip glass is shown in Figure 2(a). Glass is basically SiO_2 which contains some other elements. EDS elemental analysis of plain coverslip showed the presence of silicon (Figure 7-2(b)) and nanotextured coverslip showed almost identical results (Figure 7-2(c)). Therefore, it can be said that the etching did not make any change in chemical nature of coverslip glasses.

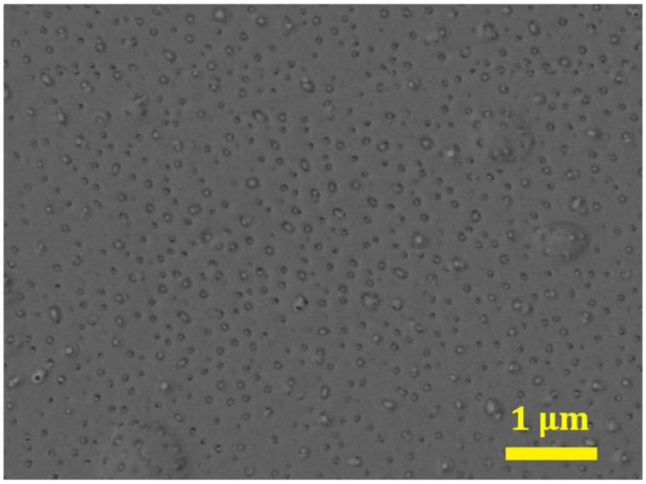

(a)

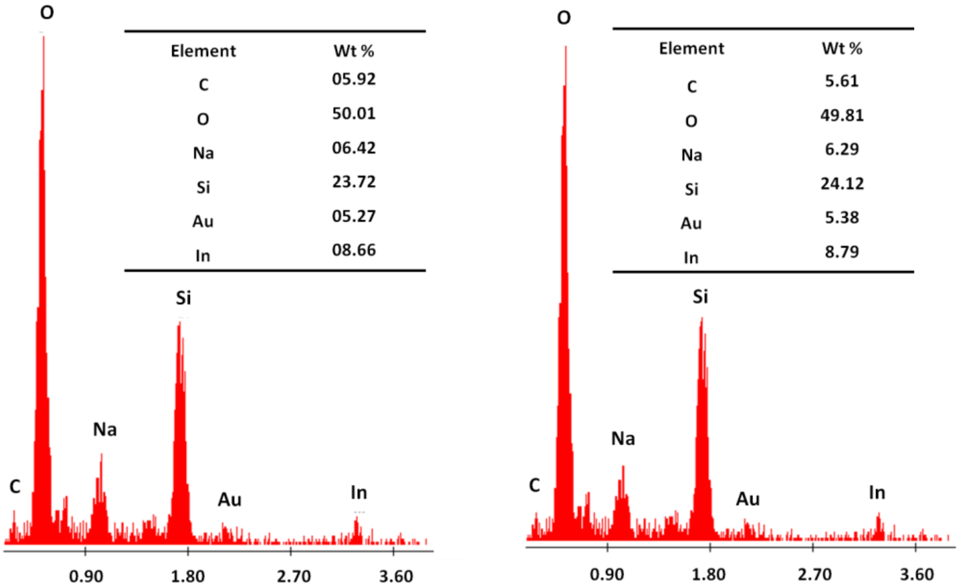

Element	Wt %
C	05.92
O	50.01
Na	06.42
Si	23.72
Au	05.27
In	08.66

Element	Wt %
C	5.61
O	49.81
Na	6.29
Si	24.12
Au	5.38
In	8.79

(a) (b)

Figure 7-2: (a) SEM micrograph of a nanotextured glass substrate; EDS elemental composition of (b) plain and (c) nanotextured coverslip glasses.

Data for Contact Angle Measurements

Contact angle from a water droplet provides the measurement of hydrophobicity or hydrophilicity of a surface. Contact angle is more than 90^o for hydrophobic surfaces and less than that for hydrophilic surfaces. Nanotexturing augments the hydrophobicity of hydrophobic surfaces and hydrophilicity of hydrophilic surfaces. The contact angles of all experimental surfaces were measured and their average values with standard deviations are recorded. For plain and nanotextured coverslips these values were 25.4 ± 1.14^o and 12.60 ± 1.52^o, respectively. Glass is hydrophilic by nature and nanotexturing enhanced its hydrophilicity in this case.

In Vitro Cell Growth on Nanotextured Surfaces

PC12 cells were seeded on TCP membranes, plain, and nanotextured coverslip glasses. The cell growth was observed on both bare substrates and nerve growth factor (NGF) treated substrates. In all cases cell densities were calculated by analyzing micrographs using *ImageJ*. On bare substrates, TCP and plain coverslips had cell densities of 475±86 and 310±76 per mm^2, respectively. For nanotextured coverslips this density was 612±95 per mm^2 which was almost twice compared to plain surfaces. Next, the substrates were treated with β subunit of NGF which is biologically active and advocates axon growth [188]. In this case, cell densities on TCP, plain, and nanotextured coverslips were 437±69, 344±89, and 649±49 per mm^2, respectively. Thus, cell growth was significantly higher in both cases on nanotextured coverslips compared to plain surfaces (Figure 7-3). One-way analysis of variance (ANOVA) analysis showed statistically significant differences (p-value < 0.01) in the cell density between plain and nanotextured coverslips for both the cases. Here, the surfaces were not coated with laminin to see the effect of nanotexture as physical cue. The implementation of laminin can undermine the effect of nanotexture as physical stimulation. As nanotexture offers larger effective surface area, it can lead higher concentration of laminin and consequently can provide faster cell growth. Again, it has been reported that laminin has profound impact on the growth, and differentiation as well as neurite outgrowth of PC12 cells [203-205]. Neuron cells generally require ECM component such as collagen, laminin, or fibronectin, etc. to attach and survive on surfaces. First of all, cells bind to the surface and subsequently dendrites begin to elongate. Proper cell attachment is imperative for the growth, differentiation, and survival. Nanotexture might enhance the level of mRNA expression of β3-tubulin in PC12 cells to facilitate better cell attachment [206]. Thus, this study aimed to understand the effect of nanotexture exclusively on cell growth without presence of laminin. Nanotexture provides a biomimetic cell-stimulating cue as cells in vivo contact nanotexture not plain interfaces [175]. Because complex nanoscale structures have been observed in basement membranes of various tissues. Nanoscale structures can regulate cell functions. Cell adaptation processes have significant impact in cell sensing and response to topography. It has been reported that nanoscale topographies of the surface influence the interfacial forces, focal adhesion, cytoskeletal, and membrane receptor organization [202]. By altering the surface topology, it is possible to modulate cell morphologies, and make substantial local biomechanical deformation to activate specific signaling cascades that eventually regulate cellular growth. Nanoscale topology regulates cell function in a noninvasive and nonbiological manner [175]. However, cell growth was regulated here by introducing isotropic nanotexture on coverslip glasses via cell adaptation mechanism independent of ECM components. The nanotexturing not only provided larger effective surface area, it offered biomimic surface and enhanced the adhesion of cells by augmenting cells-surface interactions.

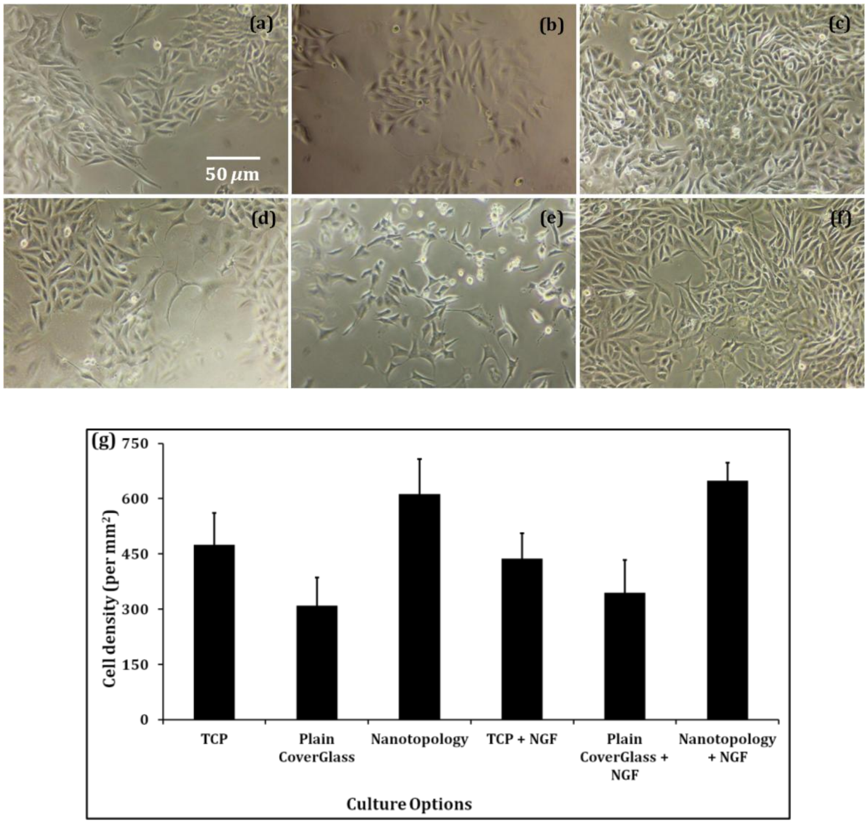

Figure 7-3: Micrographs of PC 12 cells grown on numerous substrates under following conditions: (a) TCP; (b) plain cover glass; (c) nanotopology; surfaces were coated with 100 ng/ml NGB β (d) TCP; (e) plain cover glass; (f) nanotopology; (g) density of PC 12 cells (cell number/mm^2) on all the experimental surfaces.

Nuclear Morphology of Cells

Nuclear morphology was further assessed by observing the DAPI stained cell nuclei to investigate the possibility of induction of apoptosis as a result of the presence of nanotextured coverslip substrates that were used for cell attachment and growth. We found little fragmentation and blebbing or DNA condensation in cells grown on the nanotextured surfaces compared to normal glass cover-slips or culture plate membranes, and most of the cells had round and homogeneous nuclei (Figure 7-4(a)-(c), -NGF conditions not shown). Quantification of pyknotic nuclei, which is indicative of cell death [207], is displayed in Figure 7-4(d). It was observed that between 4-8% cells did have deformed and condensed nuclei with apoptotic bodies, which is very typical for the normal handling and culture procedure.

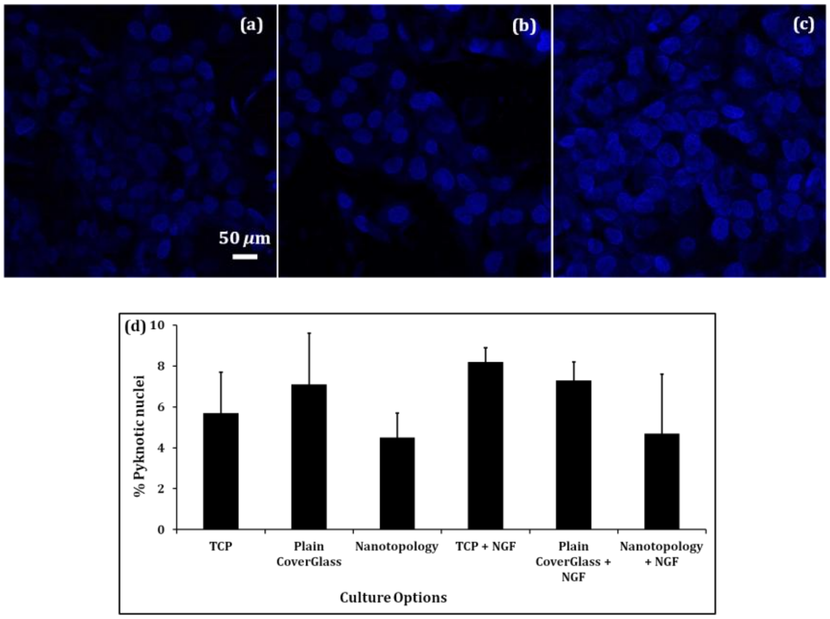

Figure 7-4: Micrographs of DAPI stained cell nuclei of PC12 cells under the treatment of NGF β on (a) TCP; (b) plain cover glass; (c) nanotopology surfaces; (d) quantification of pyknotic nuclei on various surfaces.

Conclusion

Micro-RIE provides rapid and cost-effective way of fabricating nanotextured coverslip glasses. Nanotexture stimulated the growth of PC12 cells and consequently the cell density was almost 1.9 times in nantoextured coverslips compared to plain surfaces even without presence of ECM components. This study did not use any ECM component such as collagen, laminin etc. to see the effect of only nanoscale topology as a physical cue on cell growth. The morphology study indicated that PC12 cell attachment and growth on the nanotextured substrates did not launch any apoptotic machinery of the cell. Coupled with the capability of inducing enhanced proliferation, these substrates carry excellent potential to be used for neural cell attachment, which is the precursor of enhanced differentiation that can be used to manipulate axon regeneration and guidance to facilitate neural circuit reconstruction.

Chapter 8

FUTURE RESEARCH DIRECTIONS

Introduction

This chapter focuses on the opportunity and direction of future works that would complement/supplement the current research work will be discussed. The potential use of the developed biochip for some other applications will be discussed.

Diagnosis of Different Cell Types

We have successfully implemented our microfluidic devices for the detection of renal and hGBM cancer cells based on their mechanophysical properties and overexpressed EGFR on their cell membrane. It has already shown that EGFR is a common biomarker for some other cancer such as breast cancer, lung cancer, bladder cancer and so on. The intrinsic physical and mechanical properties of these cancer cells are also different from blood cells. Thus, the developed microdevices can be implemented to detect other types of cancer cells. The procedure for the experiments will be same as mentioned earlier. First of all specific types of cancer cells will be suspended on 1X PBS and will be injected in the devices. Then using translocation behavior, filtering device or aptamer functionalized nanotextured surfaces we will try to detect them. After observing their behavior we will mix the cells in blood and try to isolate using our device. In addition to that we will closely observe the translocation behavior of different types of cancer cells and try to figure out any difference in translocation behavior for various cell types. In that case it will be possible to figure out the type of cancer for the patients. On the whole, our goal will be to collect large amount of reliable data for building a statistical backbone for our device for successful cancer detection.

Staging of Cancer

We can implement our device to determine the stages of cancer. Staging is a method of determining where a cancer is located, if or where it has spread, and whether it is affecting the functions of other organs in the body. Staging is important for the appropriate treatment and evaluating the prognosis. Our focus will be to characterize our device with sample of different stages but specific type of cancer. The overexpression of biomarker can be changed with the progression of disease. From the obtained data we will focus to determine a threshold of cell density on nanotextured aptamer functionalized surfaces for cancer cells of different stages. Also their translocation behavior will also be observed. Moreover, at different stages of cancer, physical and mechanical behavior of cells can be altered due to the transformation of cytoskeleton which will have impact on their translocation behavior.

Diagnosis of Bladder Cancer from Human Urine Samples

We have developed biosensors to detect cancer cells from blood. The developed devices can be implemented to detect bladder cancer cells from urine. It will be completely non-invasive approach to collect samples. Our device can discriminate cancer cells by their intrinsic mechanophysical properties or overexpression of biomarker. Thus, the possibility of detecting cells using this biosensor is high. The urine samples from patients with and without bladder cancer will be assessed with the device.

High Frequency Multiplexer for Microchannels to Record Translocation Profile

We have developed current measurement setup to record translocation behavior of cells through a microchannel. The physical blockage of the microchannel changes the ionic current flow and current values are read by the National Instrument's data acquisition card (NI PXI 4071) which is pretty expensive part of the electrical setup. A dedicated data acquisition card (DAC) has been employed for measuring current across only two microchannels. In order to increase the number of channels for higher throughput, adding more cards would be much costly. We plan to develop a high frequency multiplexer which can help to record data from multiple channels using a single data acquisition card. Multiplexing is a method by which multiple analog or digital signals are combined into one signal over a shared medium. This phenomenon is commonly used in telecommunications.

The multiplexers can have different number of input and output. The output from the multiplexer depends on the line that is selected. The frequency/speed at which the multiplexer can switch from one input line to the next is called the switching frequency/speed. Switching frequency, although neglected at times, plays an important role in determining the efficiency of a design. The higher the switching frequency, the faster the select line can switch from one input line to another.

The high frequency multiplexer will be added to data acquisition card to record data from multiple channels simultaneously. A high frequency multiplexer can switch the input signal among multiple channels at regular intervals. Data for all parallel channels will be recorded on computer in their respective files. Since the information is rapidly changing, the multiplexer should be able to quickly switch from one channel to the other (ideally 2.5 μsec) not to miss any significant event. This high frequency multiplexer can be implemented for other applications where simultaneous recording of data from multiple channels is required. Figure 8-1 shows design of electrical setup that utilizes 4X1 multiplexer to increase the number of microchannels quadruple.

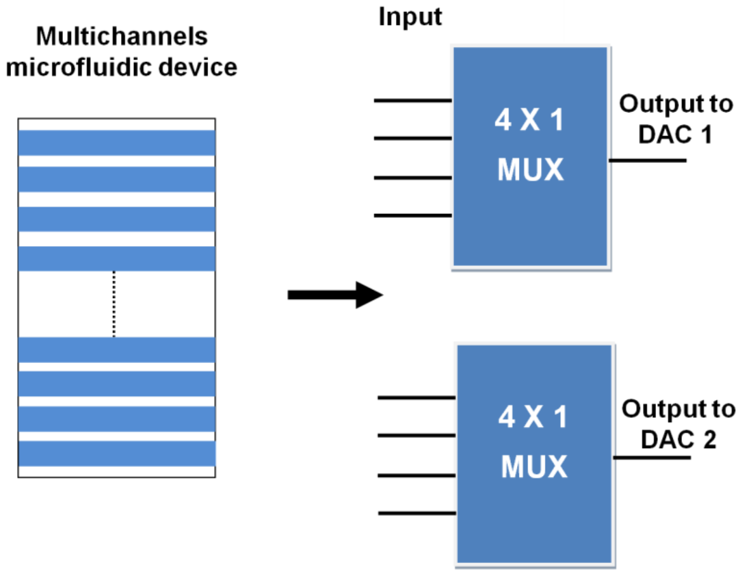

Figure 8-1: Demonstrates the use of high speed multiplexer to increase the channels four times in the microchannel array assembly.

References

[1] J. Chen, J. Li, and Y. Sun, "Microfluidic approaches for cancer cell detection, characterization, and separation," *Lab on a Chip,* vol. 12, pp. 1753-1767, 2012.

[2] D. Hanahan and R. A. Weinberg, "Hallmarks of cancer: the next generation," *Cell,* vol. 144, pp. 646-674, 2011.

[3] P. Anand, A. B. Kunnumakara, C. Sundaram, K. B. Harikumar, S. T. Tharakan, O. S. Lai, B. Sung, and B. B. Aggarwal, "Cancer is a preventable disease that requires major lifestyle changes," *Pharmaceutical Research,* vol. 25, pp. 2097-2116, 2008.

[4] E. S. Lianidou and A. Markou, "Circulating tumor cells in breast cancer: detection systems, molecular characterization, and future challenges," *Clinical Chemistry,* vol. 57, pp. 1242-1255, 2011.

[5] S. Nagrath, L. V. Sequist, S. Maheswaran, D. W. Bell, D. Irimia, L. Ulkus, M. R. Smith, E. L. Kwak, S. Digumarthy, and A. Muzikansky, "Isolation of rare circulating tumour cells in cancer patients by microchip technology," *Nature,* vol. 450, pp. 1235-1239, 2007.

[6] W. Asghar, Y. Wan, A. Ilyas, R. Bachoo, Y.-t. Kim, and S. M. Iqbal, "Electrical fingerprinting, 3D profiling and detection of tumor cells with solid-state micropores," *Lab on a Chip,* vol. 12, pp. 2345-2352, 2012.

[7] A. Ilyas, W. Asghar, Y.-t. Kim, and S. M. Iqbal, "Parallel recognition of cancer cells using addressable array of solid-state micropores," *Biosensors and Bioelectronics,* 2014.

[8] R. Siegel, J. Ma, Z. Zou, and A. Jemal, "Cancer statistics, 2014," *CA: A Cancer Journal for Clinicians,* vol. 64, pp. 9-29, 2014.

[9] M. Yu, S. Stott, M. Toner, S. Maheswaran, and D. A. Haber, "Circulating tumor cells: approaches to isolation and characterization," *The Journal of cell biology,* vol. 192, pp. 373-382, 2011.

[10] K. W. Kwon, S. S. Choi, S. H. Lee, B. Kim, S. N. Lee, M. C. Park, P. Kim, S. Y. Hwang, and K. Y. Suh, "Label-free, microfluidic separation and enrichment of human breast cancer cells by adhesion difference," *Lab on a Chip,* vol. 7, pp. 1461-1468, 2007.

[11] Y. Chen, P. Li, P.-H. Huang, Y. Xie, J. D. Mai, L. Wang, N.-T. Nguyen, and T. J. Huang, "Rare cell isolation and analysis in microfluidics," *Lab on a Chip,* vol. 14, pp. 626-645, 2014.

[12] H.-S. Moon, K. Kwon, S.-I. Kim, H. Han, J. Sohn, S. Lee, and H.-I. Jung, "Continuous separation of breast cancer cells from blood samples using multi-orifice flow fractionation (MOFF) and dielectrophoresis (DEP)," *Lab on a Chip,* vol. 11, pp. 1118-1125, 2011.

[13] Y. Wan, M. Mahmood, N. Li, P. B. Allen, Y.-t. Kim, R. Bachoo, A. D. Ellington, and S. M. Iqbal, "Nanotextured substrates with immobilized aptamers for cancer cell isolation and cytology," *Cancer,* vol. 118, pp. 1145-1154, 2012.

[14] Y. Wan, Y. Liu, P. B. Allen, W. Asghar, M. A. I. Mahmood, J. Tan, H. Duhon, Y.-t. Kim, A. D. Ellington, and S. M. Iqbal, "Capture, isolation and release of cancer cells with aptamer-functionalized glass bead array," *Lab on a Chip,* vol. 12, pp. 4693-4701, 2012.

[15] Y. Xu, J. A. Phillips, J. Yan, Q. Li, Z. H. Fan, and W. Tan, "Aptamer-based microfluidic device for enrichment, sorting, and detection of multiple cancer cells," *Analytical chemistry,* vol. 81, pp. 7436-7442, 2009.

[16] M. D. Estes, B. Ouyang, S. Ho, and C. H. Ahn, "Isolation of prostate cancer cell subpopulations of functional interest by use of an on-chip magnetic bead-based cell separator," *Journal of Micromechanics and Microengineering,* vol. 19, pp. 095015-095022, 2009.

[17] A. E. Saliba, L. Saias, E. Psychari, N. Minc, D. Simon, F. C. Bidard, C. Mathiot, J. Y. Pierga, V. Fraisier, and J. Salamero, "Microfluidic sorting and multimodal typing of cancer cells in self-assembled magnetic arrays," *Proceedings of the National Academy of Sciences,* vol. 107, pp. 14524-14529, 2010.

[18] V. Sivagnanam, B. Song, C. Vandevyver, J. C. G. BuÌˆnzli, and M. A. M. Gijs, "Selective breast cancer cell capture, culture, and immunocytochemical analysis using self-assembled magnetic bead patterns in a microfluidic chip," *Langmuir,* vol. 26, pp. 6091-6096, 2010.

[19] K. Zhang, L. B. Zhao, S. S. Guo, B. X. Shi, T. L. Lam, Y. C. Leung, Y. Chen, X. Z. Zhao, H. L. W. Chan, and Y. Wang, "A microfluidic system with surface modified piezoelectric sensor for trapping and detection of cancer cells," *Biosensors and Bioelectronics,* vol. 26, pp. 935-939, 2010.

[20] C. L. Chen, K. C. Chen, Y. C. Pan, T. P. Lee, L. C. Hsiung, C. M. Lin, C. Y. Chen, C. H. Lin, B. L. Chiang, and A. M. Wo, "Separation and detection of rare cells in a microfluidic disk via negative selection," *Lab Chip,* vol. 11, pp. 474-483, 2010.

[21] J. H. Kang, S. Krause, H. Tobin, A. Mammoto, M. Kanapathipillai, and D. E. Ingber, "A combined micromagnetic-microfluidic device for rapid capture and culture of rare circulating tumor cells," *Lab on a Chip,* vol. 12, pp. 2175-2181, 2012.

[22] J. Sun, M. Li, C. Liu, Y. Zhang, D. Liu, W. Liu, G. Hu, and X. Jiang, "Double spiral microchannel for label-free tumor cell separation and enrichment," *Lab on a Chip,* vol. 12, pp. 3952-3960, 2012.

[23] M. Hosokawa, T. Hayata, Y. Fukuda, A. Arakaki, T. Yoshino, T. Tanaka, and T. Matsunaga, "Size-selective microcavity array for rapid and efficient detection of circulating tumor cells," *Analytical Chemistry,* vol. 82, pp. 6629-6635, 2010.

[24] S. Zheng, H. K. Lin, B. Lu, A. Williams, R. Datar, R. J. Cote, and Y. C. Tai, "3D microfilter device for viable circulating tumor cell (CTC) enrichment from blood," *Biomedical Microdevices,* vol. 13, pp. 203-213, 2011.

[25] H. K. Lin, S. Zheng, A. J. Williams, M. Balic, S. Groshen, H. I. Scher, M. Fleisher, W. Stadler, R. H. Datar, and Y. C. Tai, "Portable filter-based microdevice for detection and characterization of circulating tumor cells," *Clinical Cancer Research,* vol. 16, pp. 5011-5018, 2010.

[26] S. L. Stott, C. H. Hsu, D. I. Tsukrov, M. Yu, D. T. Miyamoto, B. A. Waltman, S. M. Rothenberg, A. M. Shah, M. E. Smas, and G. K. Korir, "Isolation of circulating tumor cells using a microvortex-generating herringbone-chip," *Proceedings of the National Academy of Sciences,* vol. 107, pp. 18392-18397, 2010.

[27] S. L. Murphy, J. Q. Xu, and K. D. Kochanek, "Deaths: final data for 2010," *National Vital Statistics Reports,* vol. 61, pp. 1-118, 2013.

[28] C. L. Chaffer and R. A. Weinberg, "A perspective on cancer cell metastasis," *Science,* vol. 331, pp. 1559-1564, 2011.

[29] A. G. Knudson, "Two genetic hits (more or less) to cancer," *Nature Reviews Cancer,* vol. 1, pp. 157-162, 2001.

[30] L. A. Liotta, M. L. Stracke, E. Kohn, S. Aznavoorian, and U. M. Wewer, "Tumor invasion and metastases: biochemical mechanisms," in *New Directions in Cancer Treatment*: Springer, 1989, pp. 381-398.

[31] L. A. Liotta, "Tumor invasion and metastases--role of the extracellular matrix: Rhoads Memorial Award lecture," *Cancer Research,* vol. 46, pp. 1-7, 1986.

[32] J. J. Christiansen and A. K. Rajasekaran, "Reassessing epithelial to mesenchymal transition as a prerequisite for carcinoma invasion and metastasis," *Cancer research,* vol. 66, pp. 8319-8326, 2006.

[33] J. Yang, S. A. Mani, and R. A. Weinberg, "Exploring a new twist on tumor metastasis," *Cancer research,* vol. 66, pp. 4549-4552, 2006.

[34] D. S. Goodsell, "The molecular perspective: epidermal growth factor," *The Oncologist,* vol. 8, pp. 496-497, 2003.

[35] E. Rozengurt, K. D. Brown, and P. Pettican, "Vasopressin inhibition of epidermal growth factor binding to cultured mouse cells," *Journal of Biological Chemistry,* vol. 256, pp. 716-722, 1981.

[36] R. Pérez, M. Pascual, A. Macías, and A. Lage, "Epidermal growth factor receptors in human breast cancer," *Breast Cancer Research and Treatment,* vol. 4, pp. 189-193, 1984.

[37] R. S. Herbst, "Review of epidermal growth factor receptor biology," *International Journal of Radiation Oncology* Biology* Physics,* vol. 59, pp. S21-S26, 2004.

[38] P. Paterlini-Brechot and N. L. Benali, "Circulating tumor cells (CTC) detection: clinical impact and future directions," *Cancer letters,* vol. 253, pp. 180-204, 2007.

[39] J. Boonstra, P. Rijken, B. Humbel, F. Cremers, and A. Verkleij, "The epidermal growth factor," *Cell biology international,* vol. 19, pp. 413-430, 1995.

[40] R. Nishikawa, X.-D. Ji, R. C. Harmon, C. S. Lazar, G. N. Gill, W. K. Cavenee, and H. J. Huang, "A mutant epidermal growth factor receptor common in human glioma confers enhanced tumorigenicity," *Proceedings of the National Academy of Sciences,* vol. 91, pp. 7727-7731, 1994.

[41] A. J. Ekstrand, N. Longo, M. L. Hamid, J. J. Olson, L. Liu, V. P. Collins, and C. D. James, "Functional characterization of an EGF receptor with a truncated extracellular domain expressed in glioblastomas with EGFR gene amplification," *Oncogene,* vol. 9, pp. 2313-2320, 1994.

[42] N. E. Hynes and G. MacDonald, "ErbB receptors and signaling pathways in cancer," *Current opinion in cell biology,* vol. 21, pp. 177-184, 2009.

[43] J. Mendelsohn, "The epidermal growth factor receptor as a target for cancer therapy," *Endocrine-Related Cancer,* vol. 8, p. 3, 2001.

[44] G. Carpenter and S. Cohen, "Epidermal growth factor," *Annual review of biochemistry,* vol. 48, pp. 193-216, 1979.

[45] T. R. Ashworth, "A case of cancer in which cells similar to those in the tumours were seen in the blood after death," *Aust Med J,* vol. 14, pp. 146-149, 1869.

[46] R. W. Carey, P. D. Taft, J. M. Bennett, and S. Kaufman, "Carcinocythemia (carcinoma cell leukemia): An acute leukemia-like picture due to metastatic carcinoma cells," *The American journal of medicine,* vol. 60, pp. 273-278, 1976.

[47] M. Toner and D. Irimia, "Blood-on-a-chip," *Annu. Rev. Biomed. Eng.,* vol. 7, pp. 77-103, 2005.

[48] S. R. Shi, R. J. Cote, and C. R. Taylor, "Antigen retrieval immunohistochemistry: past, present, and future," *Journal of Histochemistry & Cytochemistry,* vol. 45, p. 327, 1997.

[49] S. D. Jayasena, "Aptamers: an emerging class of molecules that rival antibodies in diagnostics," *Clinical Chemistry,* vol. 45, p. 1628, 1999.

[50] N. Hamaguchi, A. Ellington, and M. Stanton, "Aptamer beacons for the direct detection of proteins," *Analytical Biochemistry,* vol. 294, pp. 126-131, 2001.

[51] D. Proske, M. Blank, R. Buhmann, and A. Resch, "Aptamers-basic research, drug development, and clinical applications," *Applied microbiology and biotechnology,* vol. 69, pp. 367-374, 2005.

[52] O. C. Farokhzad, S. Jon, A. Khademhosseini, T. N. T. Tran, D. A. LaVan, and R. Langer, "Nanoparticle-Aptamer Bioconjugates," *Cancer research,* vol. 64, p. 7668, 2004.

[53] J. A. Phillips, Y. Xu, Z. Xia, Z. H. Fan, and W. Tan, "Enrichment of cancer cells using aptamers immobilized on a microfluidic channel," *Analytical Chemistry,* vol. 81, pp. 1033-1039, 2008.

[54] D. H. J. Bunka and P. G. Stockley, "Aptamers come of ageâ€“at last," *Nature Reviews Microbiology,* vol. 4, pp. 588-596, 2006.

[55] C. Tuerk and L. Gold, "Systematic evolution of ligands by exponential enrichment: RNA ligands to bacteriophage T4 DNA polymerase," *Science,* vol. 249, p. 505, 1990.

[56] A. D. Ellington and J. W. Szostak, "In vitro selection of RNA molecules that bind specific ligands," *Nature,* vol. 346, pp. 818-822, 1990.

[57] J. E. Weigand and B. Suess, "Aptamers and riboswitches: perspectives in biotechnology," *Applied microbiology and biotechnology,* vol. 85, pp. 229-236, 2009.

[58] F. Jarosch, K. Buchner, and S. Klussmann, "In vitro selection using a dual RNA library that allows primerless selection," *Nucleic acids research,* vol. 34, p. e86, 2006.

[59] L. Cerchia, F. Ducong, C. Pestourie, J. Boulay, Y. Aissouni, K. Gombert, B. Tavitian, V. De Franciscis, and D. Libri, "Neutralizing aptamers from whole-cell SELEX inhibit the RET receptor tyrosine kinase," *PLoS biology,* vol. 3, p. e123, 2005.

[60] J. K. Joung, E. I. Ramm, and C. O. Pabo, "A bacterial two-hybrid selection system for studying protein肦NA and protein杙rotein interactions," *Proceedings of the National Academy of Sciences,* vol. 97, p. 7382, 2000.

[61] T. Sun, L. Feng, X. Gao, and L. Jiang, "Bioinspired surfaces with special wettability," *Accounts of Chemical Research,* vol. 38, pp. 644-652, 2005.

[62] Z. Guo and W. Liu, "Biomimic from the superhydrophobic plant leaves in nature: Binary structure and unitary structure," *Plant Science,* vol. 172, pp. 1103-1112, 2007.

[63] L. Feng, Y. Zhang, J. Xi, Y. Zhu, N. Wang, F. Xia, and L. Jiang, "Petal effect: a superhydrophobic state with high adhesive force," *Langmuir,* vol. 24, pp. 4114-4119, 2008.

[64] A. R. Parker and C. R. Lawrence, "Water capture by a desert beetle," *Nature,* vol. 414, pp. 33-34, 2001.

[65] R. P. Evershed, R. Berstan, F. Grew, M. S. Copley, A. J. H. Charmant, E. Barham, H. R. Mottram, and G. Brown, "Water-repellent legs of water striders," *Carbohyd. Res,* vol. 113, pp. 291-299, 1983.

[66] R. N. Wenzel, "Resistance of solid surfaces to wetting by water," *Industrial & Engineering Chemistry,* vol. 28, pp. 988-994, 1936.

[67] A. B. D. Cassie and S. Baxter, "Wettability of porous surfaces," *Transactions of the Faraday Society,* vol. 40, pp. 546-551, 1944.

[68] N. A. Patankar, "Transition between superhydrophobic states on rough surfaces," *Langmuir,* vol. 20, pp. 7097-7102, 2004.

[69] D. Byun, J. Hong, J. H. Ko, Y. J. Lee, H. C. Park, B.-K. Byun, and J. R. Lukes, "Wetting characteristics of insect wing surfaces," *Journal of Bionic Engineering,* vol. 6, pp. 63-70, 2009.

[70] A. Balmert, H. F. Bohn, P. Ditsche-Kuru, and W. Barthlott, "Dry under water: Comparative morphology and functional aspects of air-retaining insect surfaces," *Journal of Morphology,* vol. 272, pp. 442-451, 2011.

[71] S. J. Liliensiek, P. Nealey, and C. J. Murphy, "Characterization of endothelial basement membrane nanotopography in rhesus macaque as a guide for vessel tissue engineering," *Tissue Engineering Part A,* vol. 15, pp. 2643-2651, 2009.

[72] G. A. Abrams, S. L. Goodman, P. F. Nealey, M. Franco, and C. J. Murphy, "Nanoscale topography of the basement membrane underlying the corneal epithelium of the rhesus macaque," *Cell and tissue research,* vol. 299, pp. 39-46, 2000.

[73] S. Brody, T. Anilkumar, S. Liliensiek, J. A. Last, C. J. Murphy, and A. Pandit, "Characterizing nanoscale topography of the aortic heart valve basement membrane for tissue engineering heart valve scaffold design," *Tissue engineering,* vol. 12, pp. 413-421, 2006.

[74] E. Eybl, A. Griesmacher, M. Grimm, and E. Wolner, "Toxic effects of aldehydes released from fixed pericardium on bovine aortic endothelial cells," *Journal of Biomedical Materials Research,* vol. 23, pp. 1355-1365, 1989.

[75] K. Jansson, L. Bengtsson, J. Swedenborg, and A. Haegerstrand, "In vitro endothelialization of bioprosthetic heart valves provides a cell monolayer with proliferative capacities and resistance to pulsatile flow," *The Journal of Thoracic and Cardiovascular Surgery,* vol. 121, pp. 108-115, 2001.

[76] G. A. Abrams, S. S. Schaus, S. L. Goodman, P. F. Nealey, and C. J. Murphy, "Nanoscale topography of the corneal epithelial basement membrane and Descemet's membrane of the human," *Cornea,* vol. 19, pp. 57-64, 2000.

[77] F.-Z. Cui and J. Ge, "New observations of the hierarchical structure of human enamel, from nanoscale to microscale," *Journal of tissue engineering and regenerative medicine,* vol. 1, pp. 185-191, 2007.

[78] C. M. Earhart, C. E. Hughes, R. S. Gaster, C. C. Ooi, R. J. Wilson, L. Y. Zhou, E. W. Humke, L. Xu, D. J. Wong, and S. B. Willingham, "Isolation and mutational analysis of circulating tumor cells from lung cancer patients with magnetic sifters and biochips," *Lab on a Chip,* vol. 14, pp. 78-88, 2014.

[79] K. Hoshino, Y. Y. Huang, N. Lane, M. Huebschman, J. W. Uhr, E. P. Frenkel, and X. Zhang, "Microchip-based immunomagnetic detection of circulating tumor cells," *Lab on a Chip,* vol. 11, pp. 3449-3457, 2011.

[80] K. Hoshino, P. Chen, Y.-Y. Huang, and X. Zhang, "Computational analysis of microfluidic immunomagnetic rare cell separation from a particulate blood flow," *Analytical Chemistry,* vol. 84, pp. 4292-4299, 2012.

[81] S. Kim, S.-I. Han, M.-J. Park, C.-W. Jeon, Y.-D. Joo, I.-H. Choi, and K.-H. Han, "Circulating tumor cell microseparator based on lateral magnetophoresis and immunomagnetic nanobeads," *Analytical Chemistry,* vol. 85, pp. 2779-2786, 2013.

[82] K. Hoshino, Y.-Y. Huang, N. Lane, M. Huebschman, J. W. Uhr, E. P. Frenkel, and X. Zhang, "Microchip-based immunomagnetic detection of circulating tumor cells," *Lab on a Chip,* vol. 11, pp. 3449-3457, 2011.

[83] F. F. Becker, X. B. Wang, Y. Huang, R. Pethig, J. Vykoukal, and P. R. Gascoyne, "Separation of human breast cancer cells from blood by differential dielectric affinity," *Proceedings of the National Academy of Sciences,* vol. 92, pp. 860-864, 1995.

[84] P. R. C. Gascoyne, X. B. Wang, Y. Huang, and F. F. Becker, "Dielectrophoretic separation of cancer cells from blood," *Industry Applications, IEEE Transactions on,* vol. 33, pp. 670-678, 1997.

[85] J. Cheng, E. L. Sheldon, L. Wu, M. J. Heller, and J. P. O'Connell, "Isolation of cultured cervical carcinoma cells mixed with peripheral blood cells on a bioelectronic chip," *Analytical chemistry,* vol. 70, pp. 2321-2326, 1998.

[86] Y. Huang, J. Yang, X. B. Wang, F. F. Becker, and P. R. C. Gascoyne, "The removal of human breast cancer cells from hematopoietic CD34+ stem cells by dielectrophoretic field-flow-fractionation," *Journal of hematotherapy & stem cell research,* vol. 8, pp. 481-490, 1999.

[87] J. Yang, Y. Huang, X. B. Wang, F. F. Becker, and P. R. C. Gascoyne, "Cell separation on microfabricated electrodes using dielectrophoretic/gravitational field-flow fractionation," *Analytical Chemistry,* vol. 71, pp. 911-918, 1999.

[88] H. S. Moon, K. Kwon, S. I. Kim, H. Han, J. Sohn, S. Lee, and H. I. Jung, "Continuous separation of breast cancer cells from blood samples using multi-orifice flow fractionation (MOFF) and dielectrophoresis (DEP)," *Lab on a Chip,* vol. 11, pp. 1118-1125, 2008.

[89] P. R. C. Gascoyne, J. Noshari, T. J. Anderson, and F. F. Becker, "Isolation of rare cells from cell mixtures by dielectrophoresis," *Electrophoresis,* vol. 30, pp. 1388-1398, 2009.

[90] A. Gencoglu and A. Minerick, "Chemical and morphological changes on platinum microelectrode surfaces in AC and DC fields with biological buffer solutions," *Lab Chip,* vol. 9, pp. 1866-1873, 2009.

[91] A. Salmanzadeh, L. Romero, H. Shafiee, R. C. Gallo-Villanueva, M. A. Stremler, S. D. Cramer, and R. V. Davalos, "Isolation of prostate tumor initiating cells (TICs) through their dielectrophoretic signature," *Lab Chip,* vol. 12, pp. 182-189, 2012.

[92] D. R. Gossett, W. M. Weaver, A. J. Mach, S. C. Hur, H. T. K. Tse, W. Lee, H. Amini, and D. Di Carlo, "Label-free cell separation and sorting in microfluidic systems," *Analytical and bioanalytical chemistry,* vol. 397, pp. 3249-3267, 2010.

[93] A. A. Adams, P. I. Okagbare, J. Feng, M. L. Hupert, D. Patterson, J. GoÌˆttert, R. L. McCarley, D. Nikitopoulos, M. C. Murphy, and S. A. Soper, "Highly efficient circulating tumor cell isolation from whole blood and label-free enumeration using polymer-based microfluidics with an integrated conductivity

sensor," *Journal of the American Chemical Society,* vol. 130, pp. 8633-8641, 2008.

[94] U. Dharmasiri, S. Balamurugan, A. A. Adams, P. I. Okagbare, A. Obubuafo, and S. A. Soper, "Highly efficient capture and enumeration of low abundance prostate cancer cells using prostateâ€•specific membrane antigen aptamers immobilized to a polymeric microfluidic device," *Electrophoresis,* vol. 30, pp. 3289-3300, 2009.

[95] M. Lekka, P. Laidler, D. Gil, J. Lekki, Z. Stachura, and A. Z. Hrynkiewicz, "Elasticity of normal and cancerous human bladder cells studied by scanning force microscopy," *European Biophysics Journal,* vol. 28, pp. 312-316, 1999.

[96] S. E. Cross, Y. S. Jin, J. Rao, and J. K. Gimzewski, "Nanomechanical analysis of cells from cancer patients," *Nature Nanotechnology,* vol. 2, pp. 780-783, 2007.

[97] S. J. Tan, L. Yobas, G. Y. H. Lee, C. N. Ong, and C. T. Lim, "Microdevice for the isolation and enumeration of cancer cells from blood," *Biomedical Microdevices,* vol. 11, pp. 883-892, 2009.

[98] S. J. Tan, R. L. Lakshmi, P. Chen, W. T. Lim, L. Yobas, and C. T. Lim, "Versatile label free biochip for the detection of circulating tumor cells from peripheral blood in cancer patients," *Biosensors and Bioelectronics,* vol. 26, pp. 1701-1705, 2010.

[99] Z. Chen, S. Zhang, Z. Tang, P. Xiao, X. Guo, and Z. Lu, "Pool-dam structure based microfluidic devices for filtering tumor cells from blood mixtures," *Surface and interface analysis,* vol. 38, pp. 996-1003, 2006.

[100] K. W. Kwon, S. S. Choi, S. H. Lee, B. Kim, S. N. Lee, M. C. Park, P. Kim, S. Y. Hwang, and K. Y. Suh, "Label-free, microfluidic separation and enrichment of human breast cancer cells by adhesion difference," *Lab Chip,* vol. 7, pp. 1461-1468, 2007.

[101] H. Mohamed, L. D. McCurdy, D. H. Szarowski, S. Duva, J. N. Turner, and M. Caggana, "Development of a rare cell fractionation device: application for cancer detection," *NanoBioscience, IEEE Transactions on,* vol. 3, pp. 251-256, 2004.

[102] T. Xu, B. Lu, Y. C. Tai, and A. Goldkorn, "A cancer detection platform which measures telomerase activity from live circulating tumor cells captured on a microfilter," *Cancer Research,* vol. 70, pp. 6420-6426, 2010.

[103] J. Chen, Y. Zheng, Q. Tan, E. Shojaei-Baghini, Y. L. Zhang, J. Li, P. Prasad, L. You, X. Y. Wu, and Y. Sun, "Classification of cell types using a microfluidic device for mechanical and electrical measurement on single cells," *Lab on a Chip,* vol. 11, pp. 3174-3181, 2011.

[104] A. Salmanzadeh, L. Romero, H. Shafiee, R. C. Gallo-Villanueva, M. A. Stremler, S. D. Cramer, and R. V. Davalos, "Isolation of prostate tumor initiating cells (TICs) through their dielectrophoretic signature," *Lab on a Chip,* vol. 12, pp. 182-189, 2012.

[105] S. Shim, K. Stemke-Hale, A. M. Tsimberidou, J. Noshari, T. E. Anderson, and P. R. C. Gascoyne, "Antibody-independent isolation of circulating tumor cells by continuous-flow dielectrophoresis," *Biomicrofluidics,* vol. 7, p. 011807, 2013.

[106] S.-B. Huang, M.-H. Wu, Y.-H. Lin, C.-H. Hsieh, C.-L. Yang, H.-C. Lin, C.-P. Tseng, and G.-B. Lee, "High-purity and label-free isolation of circulating tumor

cells (CTCs) in a microfluidic platform by using optically-induced-dielectrophoretic (ODEP) force," *Lab on a Chip,* vol. 13, pp. 1371-1383, 2013.

[107] Z. Du, N. Colls, K. H. Cheng, M. W. Vaughn, and L. Gollahon, "Microfluidic-based diagnostics for cervical cancer cells," *Biosensors and Bioelectronics,* vol. 21, pp. 1991-1995, 2006.

[108] S. Wang, H. Wang, J. Jiao, K. J. Chen, G. E. Owens, K. i. Kamei, J. Sun, D. J. Sherman, C. P. Behrenbruch, and H. Wu, "Three-dimensional nanostructured substrates toward efficient capture of circulating tumor cells," *Angewandte Chemie,* vol. 121, pp. 9132-9135, 2009.

[109] S. Wang, K. Liu, J. Liu, Z. F. Yu, X. Xu, L. Zhao, T. Lee, E. K. Lee, J. Reiss, and K. Lee, "Highly efficient capture of circulating tumor cells by using nanostructured silicon substrates with integrated chaotic micromixers," *Angewandte Chemie International Edition,* vol. 50, pp. 3084-3088, 2011.

[110] H. J. Yoon, T. H. Kim, Z. Zhang, E. Azizi, T. M. Pham, C. Paoletti, J. Lin, N. Ramnath, M. S. Wicha, and D. F. Hayes, "Sensitive capture of circulating tumour cells by functionalized graphene oxide nanosheets," *Nature Nanotechnology,* vol. 8, pp. 735-741, 2013.

[111] W. Zhao, C. H. Cui, S. Bose, D. Guo, C. Shen, W. P. Wong, K. Halvorsen, O. C. Farokhzad, G. S. L. Teo, and J. A. Phillips, "Bioinspired multivalent DNA network for capture and release of cells," *Proceedings of the National Academy of Sciences,* vol. 109, pp. 19626-19631, 2012.

[112] J. Liu, S. Guo, L. Zhang, H. Huang, D. Baigl, M. Xie, Y. Chen, and W. Pang, "A micropillar-integrated smart microfluidic device for specific capture and sorting of cells," *Electrophoresis,* vol. 28, pp. 4713-4722, 2007.

[113] S. Zheng, H. Lin, J.-Q. Liu, M. Balic, R. Datar, R. J. Cote, and Y.-C. Tai, "Membrane microfilter device for selective capture, electrolysis and genomic analysis of human circulating tumor cells," *Journal of Chromatography A,* vol. 1162, pp. 154-161, 2007.

[114] G. Vona, A. Sabile, M. Louha, V. Sitruk, S. Romana, K. Schutze, F. Capron, D. Franco, M. Pazzagli, and M. Vekemans, "Isolation by size of epithelial tumor cells: a new method for the immunomorphological and molecular characterization of circulating tumor cells," *The American Journal of Pathology,* vol. 156, pp. 57-63, 2000.

[115] S. M. McFaul, B. K. Lin, and H. Ma, "Cell separation based on size and deformability using microfluidic funnel ratchets," *Lab on a Chip,* vol. 12, pp. 2369-2376, 2012.

[116] K. Loutherback, J. D'Silva, L. Liu, A. Wu, R. H. Austin, and J. C. Sturm, "Deterministic separation of cancer cells from blood at 10 mL/min," *AIP Advances,* vol. 2, p. 042107, 2012.

[117] H. W. Hou, M. E. Warkiani, B. L. Khoo, Z. R. Li, R. A. Soo, D. S.-W. Tan, W.-T. Lim, J. Han, A. A. S. Bhagat, and C. T. Lim, "Isolation and retrieval of circulating tumor cells using centrifugal forces," *Scientific Reports,* vol. 3, p. 1259, 2013.

[118] M. E. Warkiani, G. Guan, K. B. Luan, W. C. Lee, A. A. S. Bhagat, P. K. Chaudhuri, D. S.-W. Tan, W. T. Lim, S. C. Lee, and P. C. Y. Chen, "Slanted spiral microfluidics for the ultra-fast, label-free isolation of circulating tumor cells," *Lab on a Chip,* vol. 14, pp. 128-137, 2014.

[119] G.-S. Park, H. Kwon, D. W. Kwak, S. Y. Park, M. Kim, J.-H. Lee, H. Han, S. Heo, X. S. Li, and J. H. Lee, "Full surface embedding of gold clusters on silicon

nanowires for efficient capture and photothermal therapy of circulating tumor cells," *Nano Letters,* vol. 12, pp. 1638-1642, 2012.

[120] W. Asghar, Y.-T. Kim, A. Ilyas, J. Sankaran, Y. Wan, and S. M. Iqbal, "Synthesis of nano-textured biocompatible scaffolds from chicken eggshells," *Nanotechnology,* vol. 23, p. 475601, 2012.

[121] L. Wang, W. Asghar, U. Demirci, and Y. Wan, "Nanostructured substrates for isolation of circulating tumor cells," *Nano Today,* vol. 8, pp. 374-387, 2013.

[122] H. Baac, J.-H. Lee, J.-M. Seo, T. H. Park, H. Chung, S.-D. Lee, and S. J. Kim, "Submicron-scale topographical control of cell growth using holographic surface relief grating," *Materials Science and Engineering: C,* vol. 24, pp. 209-212, 2004.

[123] B. Zhu, Q. Lu, J. Yin, J. Hu, and Z. Wang, "Alignment of osteoblast-like cells and cell-produced collagen matrix induced by nanogrooves," *Tissue engineering,* vol. 11, pp. 825-834, 2005.

[124] D. S. Kim, H. S. Lee, J. Lee, S. Kim, K.-H. Lee, W. Moon, and T. H. Kwon, "Replication of high-aspect-ratio nanopillar array for biomimetic gecko foot-hair prototype by UV nano embossing with anodic aluminum oxide mold," *Microsystem Technologies,* vol. 13, pp. 601-606, 2007.

[125] B. Das and S. P. McGinnis, "Novel template-based semiconductor nanostructures and their applications," *Applied Physics A,* vol. 71, pp. 681-688, 2000.

[126] P. D. Dalton, N. T. Joergensen, J. Groll, and M. Moeller, "Patterned melt electrospun substrates for tissue engineering," *Biomedical Materials,* vol. 3, p. 034109, 2008.

[127] U. A. Gurkan, S. Tasoglu, D. Kavaz, M. C. Demirel, and U. Demirci, "Emerging technologies for assembly of microscale hydrogels," *Advanced healthcare materials,* vol. 1, pp. 149-158, 2012.

[128] S. Tasoglu, D. Kavaz, U. A. Gurkan, S. Guven, P. Chen, R. Zheng, and U. Demirci, "Paramagnetic levitational assembly of hydrogels," *Advanced Materials,* vol. 25, pp. 1137–1143, 2013.

[129] F. Xu, F. Inci, O. Mullick, U. A. Gurkan, Y. Sung, D. Kavaz, B. Li, E. B. Denkbas, and U. Demirci, "Release of magnetic nanoparticles from cell-encapsulating biodegradable nanobiomaterials," *ACS nano,* vol. 6, pp. 6640-6649, 2012.

[130] N. G. Durmus, S. Tasoglu, and U. Demirci, "Bioprinting: Functional droplet networks," *Nature materials,* vol. 12, pp. 478-479, 2013.

[131] J. Doshi and D. H. Reneker, "Electrospinning process and applications of electrospun fibers," *Journal of electrostatics,* vol. 35, pp. 151-160, 1995.

[132] R. L. Price, K. Ellison, K. M. Haberstroh, and T. J. Webster, "Nanometer surface roughness increases select osteoblast adhesion on carbon nanofiber compacts," *Journal of biomedical materials research Part A,* vol. 70, pp. 129-138, 2004.

[133] L. P. Zanello, B. Zhao, H. Hu, and R. C. Haddon, "Bone cell proliferation on carbon nanotubes," *Nano Letters,* vol. 6, pp. 562-567, 2006.

[134] S. D. Vidyala, W. Asghar, and S. M. Iqbal, "Porous Organic Nanolayers for Coating of Solid-state Devices," *Journal of nanobiotechnology,* vol. 9, p. 18, 2011.

[135] L. J. Lee, C. Zeng, X. Cao, X. Han, J. Shen, and G. Xu, "Polymer nanocomposite foams," *Composites science and technology,* vol. 65, pp. 2344-2363, 2005.

[136] Y. S. Nam and T. G. Park, "Porous biodegradable polymeric scaffolds prepared by thermally induced phase separation," *Journal of biomedical materials research,* vol. 47, pp. 8-17, 1999.

[137] Y. S. Song, R. L. Lin, G. Montesano, N. G. Durmus, G. Lee, S.-S. Yoo, E. Kayaalp, E. Hæggström, A. Khademhosseini, and U. Demirci, "Engineered 3D tissue models for cell-laden microfluidic channels," *Analytical and Bioanalytical Chemistry,* vol. 395, pp. 185-193, 2009.

[138] S. D. Puckett, P. P. Lee, D. M. Ciombor, R. K. Aaron, and T. J. Webster, "Nanotextured titanium surfaces for enhancing skin growth on transcutaneous osseointegrated devices," *Acta Biomaterialia,* vol. 6, pp. 2352-2362.

[139] W. G. Lee, U. Demirci, and A. Khademhosseini, "Microscale electroporation: challenges and perspectives for clinical applications," *Integrative Biology,* vol. 1, pp. 242-251, 2009.

[140] K. E. Fischer, B. J. AlemÃ¡n, S. L. Tao, R. H. Daniels, E. M. Li, M. D. BuÌˆnger, G. Nagaraj, P. Singh, A. Zettl, and T. A. Desai, "Biomimetic nanowire coatings for next generation adhesive drug delivery systems," *Nano letters,* vol. 9, pp. 716-720, 2009.

[141] M. Sitti and R. S. Fearing, "Synthetic gecko foot-hair micro/nano-structures as dry adhesives," *Journal of Adhesion Science and Technology,* vol. 17, pp. 1055-1073, 2003.

[142] K. Autumn, M. Sitti, Y. A. Liang, A. M. Peattie, W. R. Hansen, S. Sponberg, T. W. Kenny, R. Fearing, J. N. Israelachvili, and R. J. Full, "Evidence for van der Waals adhesion in gecko setae," *Proceedings of the National Academy of Sciences,* vol. 99, pp. 12252-12256, 2002.

[143] L. Chen, X. Liu, B. Su, J. Li, L. Jiang, D. Han, and S. Wang, "Aptamerâ€•Mediated Efficient Capture and Release of T Lymphocytes on Nanostructured Surfaces," *Advanced Materials,* vol. 23, pp. 4376-4380, 2011.

[144] S. Wang, H. Wang, J. Jiao, K. J. Chen, G. E. Owens, K. i. Kamei, J. Sun, D. J. Sherman, C. P. Behrenbruch, and H. Wu, "Threeâ€•Dimensional Nanostructured Substrates toward Efficient Capture of Circulating Tumor Cells," *Angewandte Chemie,* vol. 121, pp. 9132-9135, 2009.

[145] S. Wang, K. Liu, J. Liu, Z. T. F. Yu, X. Xu, L. Zhao, T. Lee, E. K. Lee, J. Reiss, and Y. K. Lee, "Highly efficient capture of circulating tumor cells by using nanostructured silicon substrates with integrated chaotic micromixers," *Angewandte Chemie International Edition,* vol. 50, pp. 3084-3088, 2011.

[146] S. T. Kim, D.-J. Kim, T.-J. Kim, D.-W. Seo, T.-H. Kim, S.-Y. Lee, K. Kim, K.-M. Lee, and S.-K. Lee, "Novel Streptavidin-Functionalized Silicon Nanowire Arrays for CD4+ T Lymphocyte Separation," *Nano letters,* vol. 10, pp. 2877-2883, 2010.

[147] S.-K. Lee, G.-S. Kim, Y. Wu, D.-J. Kim, Y. Lu, M. Kwak, L. Han, J.-H. Hyung, J.-K. Seol, and C. Sander, "Nanowire substrate-based laser scanning cytometry for quantitation of circulating tumor cells," *Nano letters,* vol. 12, pp. 2697-2704, 2012.

[148] W. Chen, S. Weng, F. Zhang, S. Allen, X. Li, L. Bao, R. H. W. Lam, J. A. Macoska, S. D. Merajver, and J. Fu, "Nanoroughened Surfaces for Efficient Capture of Circulating Tumor Cells without Using Capture Antibodies," *ACS nano,* vol. 7, pp. 566-575, 2012.

[149] L. A. Liotta, K. Tryggvason, S. Garbisa, I. Hart, C. M. Foltz, and S. Shafie, "Metastatic potential correlates with enzymatic degradation of basement membrane collagen," *Nature,* vol. 284, pp. 67-68, 1980.

[150] A. D. Hughes and M. R. King, "Use of naturally occurring halloysite nanotubes for enhanced capture of flowing cells," *Langmuir,* vol. 26, pp. 12155-12164, 2010.

[151] W. Han, B. A. Allio, D. G. Foster, and M. R. King, "Nanoparticle coatings for enhanced capture of flowing cells in microtubes," *ACS nano,* vol. 4, pp. 174-180, 2009.

[152] J. Sekine, S. C. Luo, S. Wang, B. Zhu, H. R. Tseng, and H. h. Yu, "Functionalized Conducting Polymer Nanodots for Enhanced Cell Capturing: The Synergistic Effect of Capture Agents and Nanostructures," *Advanced Materials,* vol. 23, pp. 4788-4792, 2011.

[153] B. Wang, A. L. Weldon, P. Kumnorkaew, B. Xu, J. F. Gilchrist, and X. Cheng, "Effect of surface nanotopography on immunoaffinity cell capture in microfluidic devices," *Langmuir,* vol. 27, pp. 11229-11237, 2011.

[154] N. Zhang, Y. Deng, Q. Tai, B. Cheng, L. Zhao, Q. Shen, R. He, L. Hong, W. Liu, and S. Guo, "Electrospun TiO2 Nanofiber-Based Cell Capture Assay for Detecting Circulating Tumor Cells from Colorectal and Gastric Cancer Patients," *Advanced Materials,* vol. 24, pp. 2756-2760, 2012.

[155] L. Chen, X. Liu, B. Su, J. Li, L. Jiang, D. Han, and S. Wang, "Aptamer-mediated efficient capture and release of T lymphocytes on nanostructured surfaces," *Advanced Materials,* vol. 23, pp. 4376-4380, 2011.

[156] A. Hatch, D. M. Pesko, and S. K. Murthy, "Tag-free microfluidic separation of cells against multiple markers," *Analytical Chemistry,* vol. 84, pp. 4618-4621, 2012.

[157] M. Islam, W. Asghar, Y.-t. Kim, and S. M. Iqbal, "Cell elasticity-based microfluidic label-free isolation of metastatic tumor cells," *British Journal of Medicine and Medical Research,* vol. 4, pp. 2119-2128, 2013.

[158] Y. Wan, Y.-t. Kim, L. Na, A. D. Ellington, and S. M. Iqbal, "Aptamer-Based Lab-on-Chip for Cancer Cell Isolation and Detection," in *ASME 2010 First Global Congress on NanoEngineering for Medicine and Biology*, pp. 35-36.

[159] L. Bacakova, E. Filova, M. Parizek, T. Ruml, and V. Svorcik, "Modulation of cell adhesion, proliferation and differentiation on materials designed for body implants," *Biotechnology Advances,* vol. 29, pp. 739-767, 2011.

[160] S. A. Biela, Y. Su, J. P. Spatz, and R. Kemkemer, "Different sensitivity of human endothelial cells, smooth muscle cells and fibroblasts to topography in the nano-micro range," *Acta Biomaterialia,* vol. 5, pp. 2460-2466, 2009.

[161] A. Thapa, D. C. Miller, T. J. Webster, and K. M. Haberstroh, "Nano-structured polymers enhance bladder smooth muscle cell function," *Biomaterials,* vol. 24, pp. 2915-2926, 2003.

[162] D. C. Miller, A. Thapa, K. M. Haberstroh, and T. J. Webster, "Endothelial and vascular smooth muscle cell function on poly (lactic-co-glycolic acid) with nano-structured surface features," *Biomaterials,* vol. 25, pp. 53-61, 2004.

[163] K. Tsougeni, A. Tserepi, G. Boulousis, V. Constantoudis, and E. Gogolides, "Control of Nanotexture and Wetting Properties of Polydimethylsiloxane from Very Hydrophobic to Super-Hydrophobic by Plasma Processing," *Plasma Processes and Polymers,* vol. 4, pp. 398-405, 2007.

[164] M. E. Vlachopoulou, P. S. Petrou, S. E. Kakabakos, A. Tserepi, and E. Gogolides, "High-aspect-ratio plasma-induced nanotextured poly (dimethylsiloxane) surfaces with enhanced protein adsorption capacity," *Journal of Vacuum Science & Technology B: Microelectronics and Nanometer Structures,* vol. 26, pp. 2543-2548, 2008.

[165] T. H. Park and M. L. Shuler, "Integration of cell culture and microfabrication technology," *Biotechnology Progress,* vol. 19, pp. 243-253, 2003.

[166] M.-E. Vlachopoulou, A. Tserepi, P. S. Petrou, E. Gogolides, and S. E. Kakabakos, "Protein arrays on high-surface-area plasma-nanotextured poly (dimethylsiloxane)-coated glass slides," *Colloids and Surfaces B: Biointerfaces,* vol. 83, pp. 270-276, 2011.

[167] H. Hufnagel, A. Huebner, C. Gulch, K. Guse, C. Abell, and F. Hollfelder, "An integrated cell culture lab on a chip: modular microdevices for cultivation of mammalian cells and delivery into microfluidic microdroplets," *Lab on a Chip,* vol. 9, pp. 1576-1582, 2009.

[168] P. Kohli, C. C. Harrell, Z. Cao, R. Gasparac, W. Tan, and C. R. Martin, "DNA-functionalized nanotube membranes with single-base mismatch selectivity," *Science,* vol. 305, pp. 984-986, 2004.

[169] J. S. Sankaran, S. Goyal, W. T. Kahsai, U. H. T. Pham, and S. M. Iqbal, "Hydrophilic interfacing for thermal micro assembly of polymers (HITMAP)," *Advanced Science Letters,* vol. 4, pp. 3464-3469

2011.

[170] L. Zabaglo, M. G. Ormerod, M. Parton, A. Ring, I. E. Smith, and M. Dowsett, "Cell filtration-laser scanning cytometry for the characterisation of circulating breast cancer cells," *Cytometry Part A,* vol. 55, pp. 102-108, 2003.

[171] G. Vona, A. Sabile, M. Louha, V. Sitruk, S. Romana, K. Schtze, F. Capron, D. Franco, M. Pazzagli, and M. Vekemans, "Isolation by size of epithelial tumor cells: a new method for the immunomorphological and molecular characterization of circulating tumor cells," *The American Journal of Pathology,* vol. 156, pp. 57-63, 2000.

[172] M. M.-C. Cheng, G. Cuda, Y. L. Bunimovich, M. Gaspari, J. R. Heath, H. D. Hill, C. A. Mirkin, A. J. Nijdam, R. Terracciano, and T. Thundat, "Nanotechnologies for biomolecular detection and medical diagnostics," *Current Opinion in Chemical Biology,* vol. 10, pp. 11-19, 2006.

[173] L. Soleymani, Z. Fang, E. H. Sargent, and S. O. Kelley, "Programming the detection limits of biosensors through controlled nanostructuring," *Nature Nanotechnology,* vol. 4, pp. 844-848, 2009.

[174] S. Devabhaktuni and S. Prasad, "Nanotextured organic light emitting diode based chemical sensor," *Journal of Nanoscience and Nanotechnology,* vol. 9, pp. 6299-6306, 2009.

[175] R. Dylewicz, A. Z. Khokhar, R. Wasielewski, P. Mazur, and F. Rahman, "Nanotexturing of GaN light-emitting diode material through mask-less dry etching," *Nanotechnology,* vol. 22, p. 055301, 2011.

[176] J. Y. Lim and H. J. Donahue, "Cell sensing and response to micro-and nanostructured surfaces produced by chemical and topographic patterning," *Tissue Engineering,* vol. 13, pp. 1879-1891, 2007.

[177] K. Anselme, P. Davidson, A. M. Popa, M. Giazzon, M. Liley, and L. Ploux, "The interaction of cells and bacteria with surfaces structured at the nanometre scale," *Acta Biomaterialia,* vol. 6, pp. 3824-3846, 2010.

[178] C. T. McKee, V. K. Raghunathan, P. F. Nealey, P. Russell, and C. J. Murphy, "Topographic modulation of the orientation and shape of cell nuclei and their influence on the measured elastic modulus of epithelial cells," *Biophysical Journal,* vol. 101, pp. 2139-2146, 2011.

[179] J. C. Hansen, J. Yul Lim, L.-C. Xu, C. A. Siedlecki, D. T. Mauger, and H. J. Donahue, "Effect of surface nanoscale topography on elastic modulus of individual osteoblastic cells as determined by atomic force microscopy," *Journal of Biomechanics,* vol. 40, pp. 2865-2871, 2007.

[180] E. K. F. Yim, E. M. Darling, K. Kulangara, F. Guilak, and K. W. Leong, "Nanotopography-induced changes in focal adhesions, cytoskeletal organization, and mechanical properties of human mesenchymal stem cells," *Biomaterials,* vol. 31, pp. 1299-1306, 2010.

[181] L. Prodanov, J. te Riet, E. Lamers, M. Domanski, R. Luttge, J. J. W. A. van Loon, J. A. Jansen, and X. F. Walboomers, "The interaction between nanoscale

surface features and mechanical loading and its effect on osteoblast-like cells behavior," *Biomaterials,* vol. 31, pp. 7758-7765, 2010.

[182] I. Keun Kwon, S. Kidoaki, and T. Matsuda, "Electrospun nano-to microfiber fabrics made of biodegradable copolyesters: structural characteristics, mechanical properties and cell adhesion potential," *Biomaterials,* vol. 26, pp. 3929-3939, 2005.

[183] L. Richert, F. Vetrone, J. H. Yi, S. F. Zalzal, J. D. Wuest, F. Rosei, and A. Nanci, "Surface nanopatterning to control cell growth," *Advanced Materials,* vol. 20, pp. 1488-1492, 2008.

[184] J. Guck, S. Schinkinger, B. Lincoln, F. Wottawah, S. Ebert, M. Romeyke, D. Lenz, H. M. Erickson, R. Ananthakrishnan, and D. Mitchell, "Optical deformability as an inherent cell marker for testing malignant transformation and metastatic competence," *Biophysical Journal,* vol. 88, pp. 3689-3698, 2005.

[185] Y. Wan, J. Tan, W. Asghar, Y.-t. Kim, Y. Liu, and S. M. Iqbal, "Velocity effect on aptamer-based circulating tumor cell isolation in microfluidic devices," *The Journal of Physical Chemistry B,* vol. 115, pp. 13891-13896, 2011.

[186] N. N. Watkins, S. Sridhar, X. Cheng, G. D. Chen, M. Toner, W. Rodriguez, and R. Bashir, "A microfabricated electrical differential counter for the selective enumeration of CD4+ T lymphocytes," *Lab on a Chip,* vol. 11, pp. 1437-1447, 2011.

[187] M. M. Bellah, S. M. Iqbal, and Y.-T. Kim, "Differential behavior of EGFR-overexpressing cancer cells through aptamer-functionalized micropores," *Microfluidics and Nanofluidics,* pp. 1-10, 2014.

[188] S. Ghosh Mitra, D. R. Diercks, N. C. Mills, D. L. Hynds, and S. Ghosh, "Role of engineered nanocarriers for axon regeneration and guidance: current status and future trends," *Advanced Drug Delivery Reviews,* vol. 64, pp. 110-125, 2012.

[189] H. Cheng, L. Zhou, B. Li, M. Zhu, H.-P. Too, and W. K. Choi, "Nano-topology guided neurite outgrowth in PC12 cells is mediated by miRNAs," *Nanomedicine: Nanotechnology, Biology and Medicine,* vol. 10, pp. 1871-1875, 2014.

[190] J. Díaz-Alonso, M. Guzmán, and I. Galve-Roperh, "Endocannabinoids via CB1 receptors act as neurogenic niche cues during cortical development," *Philosophical Transactions of the Royal Society B: Biological Sciences,* vol. 367, pp. 3229-3241, 2012.

[191] P. H. Frederikse, C. Kasinathan, and N. J. Kleiman, "Parallels between neuron and lens fiber cell structure and molecular regulatory networks," *Developmental Biology,* vol. 368, pp. 255-260, 2012.

[192] S. Park, R. A. Koppes, U. P. Froriep, X. Jia, A. K. H. Achyuta, B. L. McLaughlin, and P. Anikeeva, "Optogenetic control of nerve growth," *Scientific Reports,* vol. 5, 2015.

[193] R. Ellis-Behnke, "Nano neurology and the four P's of central nervous system regeneration: preserve, permit, promote, plasticity," *Medical Clinics of North America,* vol. 91, pp. 937-962, 2007.

[194] K. Fouad, A. Krajacic, and W. Tetzlaff, "Spinal cord injury and plasticity: opportunities and challenges," *Brain Research Bulletin,* vol. 84, pp. 337-342, 2011.

[195] S. Koshizuka, S. Okada, A. Okawa, M. Koda, M. Murasawa, M. Hashimoto, T. Kamada, K. Yoshinaga, M. Murakami, and H. Moriya, "Transplanted hematopoietic stem cells from bone marrow differentiate into neural lineage cells and promote functional recovery after spinal cord injury in mice," *Journal of Neuropathology & Experimental Neurology,* vol. 63, pp. 64-72, 2004.

[196] J. Sharp and H. S. Keirstead, "Therapeutic applications of oligodendrocyte precursors derived from human embryonic stem cells," *Current Opinion in Biotechnology,* vol. 18, pp. 434-440, 2007.

[197] B. E. Reubinoff, P. Itsykson, T. Turetsky, M. F. Pera, E. Reinhartz, A. Itzik, and T. Ben-Hur, "Neural progenitors from human embryonic stem cells," *Nature Biotechnology,* vol. 19, pp. 1134-1140, 2001.

[198] F. L. Vale, J. Burns, A. B. Jackson, and M. N. Hadley, "Combined medical and surgical treatment after acute spinal cord injury: results of a prospective pilot study to assess the merits of aggressive medical resuscitation and blood pressure management," *Journal of Neurosurgery,* vol. 87, pp. 239-246, 1997.

[199] M. A. I. Mahmood, Y. Wan, M. Islam, W. Ali, M. Hanif, Y.-t. Kim, and S. M. Iqbal, "Micro+ nanotexturing of substrates to enhance ligand-assisted cancer cell isolation," *Nanotechnology,* vol. 25, p. 475102, 2014.

[200] M. Islam, A. Sajid, M. A. I. Mahmood, M. M. Bellah, P. B. Allen, Y.-T. Kim, and S. M. Iqbal, "Nanotextured polymer substrates show enhanced cancer cell isolation and cell culture," *Nanotechnology,* vol. 26, p. 225101, 2015.

[201] M. Islam, M. M. Bellah, A. Sajid, M. R. Hasan, Y.-t. Kim, and S. M. Iqbal, "Effects of Nanotexture on Electrical Profiling of Single Tumor Cell and

Detection of Cancer from Blood in Microfluidic Channels," *Scientific Reports,* vol. 5, p. 13031, 2015.

[202] L. Richert, F. Vetrone, J.-H. Yi, S. F. Zalzal, J. D. Wuest, F. Rosei, and A. Nanci, "Surface nanopatterning to control cell growth," *Advanced Materials,* vol. 20, pp. 1488-1492, 2008.

[203] S. Rogelj, M. Klagsbrun, R. Atzmon, M. Kurokawa, A. Haimovitz, Z. Fuks, and I. Vlodavsky, "Basic fibroblast growth factor is an extracellular matrix component required for supporting the proliferation of vascular endothelial cells and the differentiation of PC12 cells," *The Journal of Cell Biology,* vol. 109, pp. 823-831, 1989.

[204] P. Rossino, I. Gavazzi, R. Timpl, M. Aumailley, M. Abbadini, F. Giancotti, L. Silengo, P. C. Marchisio, and G. Tarone, "Nerve growth factor induces increased expression of a laminin-binding integrin in rat pheochromocytoma PC12 cells," *Experimental Cell Research,* vol. 189, pp. 100-108, 1990.

[205] A. D. Lander, D. K. Fujii, and L. F. Reichardt, "Purification of a factor that promotes neurite outgrowth: isolation of laminin and associated molecules," *The Journal of Cell Biology,* vol. 101, pp. 898-913, 1985.

[206] J. A. Kim, N. Lee, B. H. Kim, W. J. Rhee, S. Yoon, T. Hyeon, and T. H. Park, "Enhancement of neurite outgrowth in PC12 cells by iron oxide nanoparticles," *Biomaterials,* vol. 32, pp. 2871-2877, 2011.

[207] C. F. Adams, A. Rai, G. Sneddon, H. H. P. Yiu, B. Polyak, and D. M. Chari, "Increasing magnetite contents of polymeric magnetic particles dramatically improves labeling of neural stem cell transplant populations," *Nanomedicine: Nanotechnology, Biology and Medicine,* vol. 11, pp. 19-29, 2015.

Biographical Information

Muhymin Islam received BSc in Electrical and Electronics Engineering in 2005 from Bangladesh University of Engineering and Technology (BUET), Dhaka, Bangladesh. His undergraduate research focus was to develop improved I-V characteristics model for nanoscale MESFETs. He started his PhD in the Electrical Engineering Department at the University of Texas at Arlington, Arlington, Texas in 2010. Here he worked in Nano Bio Lab and his research focus was to develop surface engineered biosensors for the early detection of cancer. He earned his PhD in 2015.